Alma Mater Studiorum · Università di Bologna

Scuola di Scienze
Dipartimento di Fisica e Astronomia
Corso di Laurea Magistrale in Astrofisica e Cosmologia

Detection of short Gamma-Ray Bursts with CTA through real-time analysis

Tesi di Laurea

Presentata da:
Ambra Di Piano

Relatore:
Chiar.mo Prof. Cristian Vignali

Co-relatori:
Dott. Andrea Bulgarelli
Dott.ssa Valentina Fioretti

Sessione IV
Anno Accademico 2018-2019

This thesis project was carried out in association with INAF/OAS institute, Bologna.

Abstract

Context. CTA will be the next generation of ground-based observatories for high and very-high energy science, enhancing gamma-ray astronomy with the deployment of more than a hundred highly sensitive and fast-reacting Cherenkov telescopes. With respect to the current Imaging Atmospheric Cherenkov Telescopes (IACTs), CTA will cover a larger energy range (from 20 GeV up to 300 TeV) with one order of magnitude better sensitivity. The facility will be provided with a real-time analysis (RTA) software that will automatically generate science alerts and analyse data from on-going observations in real-time. One of the many scientific drives in which the RTA will play a key role is the search and follow-up of transients from external alerts (i.e. from on-space gamma-ray missions, observatories operating at other wavelengths or targets of opportunity provided by neutrinos and gravitational waves detectors). The last two years (2018-2019) have been especially fruitful and fortuitous for gamma-ray bursts (GRBs) science in the VHE domain, which is also the science case for this work.
Aims. The scope of my thesis project is to investigate one of the already existing scientific tools software packages (`ctools` in particular) for gamma-ray analysis and determine its feasibility for the RTA. The technique of full-field of view maximum likelihood analysis (adapted from on-space gamma-ray science) was chosen.
Results. A prototype pipeline for the RTA has been developed, with natively implemented utilities when required. The performance of the pipeline was extensively tested for very-short exposure times (far below the lower limit of current Cherenkov science) accounting for sensitivity degradation due to the non-optimal working condition expected of the RTA. The latest CTA Instrument Response Functions (IRFs), as provided by CTA Performance to the public, have been degraded via effective area reduction for this purpose. The reliability of the analysis methods were tested by means of the verification of Wilks' theorem for false positive detections. Through statistical studies on the pipeline parameter space (i.e. minimum required exposure time), the performance of the pipeline was evaluated in terms of localisation precision, detection significance and detection rates at short timescales. The latest available templates were used for the source simulation of a short GRB afterglow.
Conclusions. Future improvements involve further tests (i.e. with an updated population synthesis) as well as post-trials correction of the detection significance. Moreover, specific implementations allowing the pipeline to dynamically adapt to a range of science cases (i.e. other transient classes) and scenarios are required for completeness. Prospects of forthcoming collaborations may involve the integration of this pipeline within the on-going work of the gamma-ray bursts experts from the CTA Consortium.

Sommario

Contesto. Con oltre cento telescopi, CTA farà parte della prossima generazione di osservatori terrestri per l'astrofisica delle alte energie. Rispetto agli Imaging Atmospheric Cherenkov Telescopes (IACTs) attualmente operativi, CTA sarà in grado di coprire un range energetico molto superiore (da 30 GeV a 300 TeV) con sensibilità fino ad un ordine di grandezza migliore. L'osservatorio sarà provvisto di un software per l'analisi in tempo reale (RTA), incaricato di generare automaticamente allerte scientifiche ed analizzare i dati simultaneamente alle osservazioni. Uno dei casi scientifici che prevedono un ruolo protagonista da parte della RTA è la ricerca ed il follow-up di fenomeni transienti a seguito di allerte generate da altri strumenti. La ricezione di allerte scientifiche è prevista sia da parte di altre missioni in banda gamma (es. satelliti), sia da parte di strumenti che operano in altre bande energetiche (MWL) oppure "target of opportunity" generati dall'osservazione di neutrini e/o onde gravitazionali (MM). Negli ultimi due anni (2018-2019) la scienza dei gamma-ray bursts (GRBs) è stata arricchita da nuove osservazioni alle alte energie, ed è in questo contesto che è stato scelto il caso scientifico in uso per questo progetto di tesi.
Scopo. Lo scopo di questo lavoro è indagare se gli attuali strumenti di analisi scientifica per i dati gamma (`ctools` in particolare) possano essere implementati nella RTA. La tecnica di analisi considerata è quella della maximum likelihood a pieno campo di vista, ereditata dalla scienza gamma sviluppata nell'ambito di missioni spaziali.
Risultati. E' stato dunque sviluppato un prototipo per la RTA, con funzionalità implementate in modo originale laddove necessario. Le prestazioni del prototipo sono state estensivamente testate per tempi d'esposizione estremamente brevi, esplorando limiti mai raggiunti prima. A causa delle condizioni non ottimali con cui si prevede che la RTA debba operare, è stato tenuto conto della degradazione in sensibilità delle osservazioni. In particolare, i requisiti per la RTA prevedono di osservare al peggio con metà della sensibilità nominale. A questo proposito le più recenti versioni di Instrument Response Functions (IRFs) sono state degradate tramite riduzione dell'area efficacie. In primo luogo è stata testata l'affidabilità del metodo di analisi tramite la verifica del teorema di Wilks, ed in seguito si è svolto lo studio statistico dello spazio dei parametri (es. tempo minimo d'esposizione). Le prestazioni della pipeline sono state valutate in termini di precisione di localizzazione, efficienza e significatività di rivelazione. Per la simulazione della sorgente (l'afterglow di un GRB breve) sono stati utilizzati i modelli più recenti a disposizione.
Conclusioni. Miglioramenti futuri includono ulteriori test del prototipo (es. con modelli di popolazione aggiornati) e correzione post-trials della significativitá di rivelazione. Specifiche implementazioni sono inoltre necessarie per la completezza dello studio. In particolare sono richiesti degli aggiornamenti affinché la pipeline possa adattarsi dinamicamente ad un variegato campione di casi scientifici (es. altri classi di sorgenti) e scenari di osservazione (es. scoperte "serendipite"). Prossime prospettive di collaborazione coinvolgono l'integrazione di questo prototipo nel lavoro che esperti di GRB stanno svolgendo per il CTA Consorzio.

Contents

Chapter 1

Introduction

This chapter will present the context, aim and methods of my thesis research. In Section 1.1 the Cherenkov light will be briefly introduced, while the current Imaging Atmospheric Cherenkov Telescopes will be summarised in Section 1.2. Section 1.3 will present the outline of the dissertation.

The last half century has seen the development of ground-based gamma-ray astronomy (i.e. with the Cherenkov technique, Section 1.1) which allows astronomers to study the very-high energy gamma-rays indirectly, through the electromagnetic cascade they produce when interacting with the Earth's atmosphere. Nowadays there are a number of operating Imaging Atmospheric Cherenkov Telescopes (IACTs), facilities capable of capturing these brief flashes and reconstructing the signal to its astrophysical origin. The third (current) generation of IACTs is comprises of MAGIC, H.E.S.S. and VERITAS (Section 1.2). The Cherenkov Telescope Array (CTA) will be the next generation of IACTs, breaching the limits of the current facilities thanks to: *i)* a full-sky coverage allowed by two sites, one in each hemisphere; *ii)* a larger field of view by about a factor of 2 in diameter more than the largest currently available; *iii)* an unprecedented sensitivity of about one order of magnitude better than current IACTs; *iv)* higher angular and energy resolutions with respect to its predecessors, up to a factor of 1.5 and 2, respectively (Table 1.1 and Table 2.1). To achieve such high performances, CTA will deploy over a hundred fast-reacting Cherenkov telescopes (full array maximum repositioning time in less than 90 s to any point in the sky). Moreover, the facility will be provided with a real-time analysis (RTA) system which will automatically generate science alerts and perform data analysis in real-time (Chapter 3). This study was carried within the context of the role played by the RTA in science alert generation and high level data analysis in real-time. The aim is to investigate the feasibility of the currently available gamma-ray data analysis science tools for the RTA, in particular the `ctools` software package. The `ctools` adapt a technique used in space gamma-ray astronomy to ground-based Cherenkov data: the full field of view maximum likelihood. Can this technique be efficiently implemented in the RTA pipeline? Can it perform efficiently at very-short exposure times (below 100 s)? Are these algorithms computationally fast enough? These are some of the questions that will be answered.

In order to develop an RTA prototype (Chapter 5), a science case was chosen. Given the growing interest in multi-wavelengths (MWL) and multi-messenger (MM) astronomy (Chapter 2), the chosen scenario was a blind-search and follow-up analysis (in real-time) of an externally alerted short

gamma-ray burst afterglow (Chapter 4). To avoid overlapping with the ongoing work of the GW-GRB experts of the CTA Consortium, no tiling strategies were accounted for. The afterglow template was selected among those with localisation uncertainty approximately equal to the CTA field of view (about 10° in diameter). Moreover, the requirements on the sensitivity degradation were also accounted for while considering the non-optimal working condition of the RTA. The source position was assumed unknown, as the pipeline is required to automatically localise the source with a significance of at least 5σ, and tests were carried out with exposure times down to extremely short timescales (t_{exp} =1 s). A full-array (South) configuration of CTA was assumed, and the latest version of CTA Instrument Response Functions (IRFs) were utilised. The energy range coverage was from 30 GeV up to 150 TeV. An unbinned analysis method was chosen to speed up the computation time of the algorithms, a key requirement for the RTA. This research is the first attempt in trying to answer still open questions. Can the `ctools` full field of view maximum likelihood analysis be implemented in the RTA for the blind search of transients, and GRBs in particular? What is the localisation precision that the RTA can reach in locating an externally alerted (MWL or MM) source? Can the prototype pipeline follow up a short GRB afterglow when the RTA degradation in sensitivity (within CTA performance requirements) is considered? What is the minimum exposure time required for a significant detection ($\sigma > 5$) with the RTA? For how long can the RTA detect an afterglow at very-short timescales (below 100 s)?

Firstly, the pipeline false alarm rate was studied, allowing to constrain the probability of acquiring a false positive detection with a significance above 5σ. The relation between the maximum likelihood Test Statistic value (TS) and the Gaussian sigma (TS$\sim \sigma^2$) documented in the `ctools` software package manual[1] was confirmed for exposure times down to 1 s for 1 (intensity) degree of freedom (dof) analysis. For a dof=3 analysis (intensity, right ascension and declination) tests showed an overall non convergence of the algorithm, which requires further investigation and may be resolved by imposing stricter boundaries on the spatial parameters during the maximum likelihood procedure. Once investigated the false alarm rate, the study progressed in constraining the statistical uncertainty of the pipeline (Chapter 6). Simulations of the afterglow were analysed at very-sort exposure times (from 1 s up to 100 s). A mocked RTA follow-up was also performed, assuming the reception of an external alert (i.e. from satellites or GW interferometers) and the proposed strategy for the CTA transient program of observing the GRB for as long as detectable, plus two additional hours of observation from the last acquired positive detection. Confidence regions (or intervals) were derived for the source localisation, the estimation of the integral photon flux and the detection significance. In this work we derived that a minimum of $t_{exp} \geq 5$ s is required for detecting the afterglow at early times at $\sigma > 5$ and that a conservative $t_{exp} \geq 10$ s may be the safest lower boundary whenever sensitivity degradation and Extra-galactic Background Light absorption may play a major role in the observation (i.e. energies above 100 GeV with RTA). Further tests allowed us to constrain the performance of the pipeline for late time detection and for a number of source intensity values. The results look promising when confronted with the newest observations [40] [42] [41].

Future improvements (Chapter 7) involve the testing of the pipeline on a population of GRBs, both long and short, accounting for the prompt emission as well as the afterglow, and the post-trial correction of the detection significance. The foreseen RTA time integration strategy, which was not accounted for in this work, should also be implemented and the parameter space should be further investigated. A forthcoming prospective of this work may involve the integration of this pipeline within the on-going work of GRB experts for the CTA Consortium.

1.1 Cherenkov Light

The Cherenkov radiation is named after Russian physicist Pavel Cherenkov[2]. When gamma-rays interact with the Earth's atmosphere, they produce an electromagnetic air shower of photons and electron-positron pairs (e^+/e^-). Ultra-high energy particles in the shower travel faster than the the speed of light in the atmospheric medium (0.03% slower than vacuum) radiating a flash of blue, visible

[1] `http://cta.irap.omp.eu/ctools/users/user_manual/index.html`

[2] Pavel Cherenkov was the winner of the 1958 Nobel Prize for detecting Cherenkov light for the first time in the history of gamma-rays astronomy, in 1934, alongside Il'Ja Frank and Igor Tamm. This pale blue light was first observed by Marie Curie in 1910, in a highly concentrated radium solution. [139]

light similarly to how a sonic boom is created by an aircraft exceeding Mach 1. Cherenkov radiation lasts a few nanoseconds, spreading its light over a large conic area (about 250 m in diameter at approximately 2000 m of altitude) that propagates outward from the direction of motion of the primary gamma-ray. The half angle of the cone is given by

$$\theta = \tan^{-1}\left[\left(\mu_\nu^2 \frac{v^2}{c^2} - 1\right)^{1/2}\right] \tag{1.1}$$

where μ_ν is the refractive index at frequency ν and v is the velocity of the particle ($v > c/\mu_\nu$). Cherenkov light may be detected by a photoelectric device or collected by Cherenkov telescopes, such as CTA and its predecessors. The energy of any incident gamma-ray can be determined from the intensity of the Cherenkov image and its direction of arrival from the image shape and orientation (Figure 1.1). The image shape of each even is also an indicator for background rejection of Extensive Air Showers (EASs) produced by cosmic-rays, which also have an electromagnetic component. Similarly to any optical telescope, Cherenkov detector systems cannot be used during daylight or when weather conditions are unsuitable.

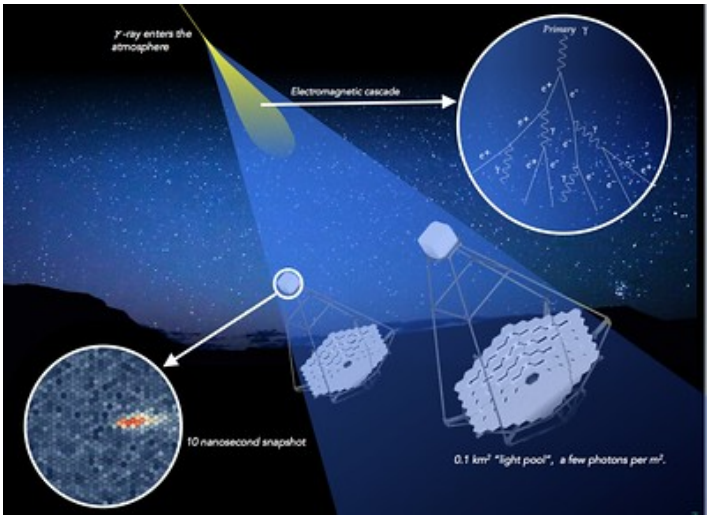

Figure 1.1: Cherenkov Effect: how CTA will detect gamma-rays. Pictured above, is the interaction between a gamma-ray and the Earth's atmosphere. The cascade produced upon impact is the source of Cherenkov light (blue, visible light) flashes, which CTA telescopes must be able to capture. **Credit:** R. White (MPIK) / K. Bernlohr (MPIK) / DESY

1.2 Imaging Atmospheric Cherenkov Telescopes

The first Cherenkov telescope to be developed was the 10 m multi-faceted telescope built for the Whipple Observatory in 1966, pioneered by T.C. Weeks, G.G. Fazio and H.F. Helmken. The Whipple telescope, which predates the stereoscopic technique, started operation in 1968 [140]. Any point sources were completely overwhelmed by the flashes of Cherenkov light due to air showers produced by charged cosmic rays, evenly spread over the sky. In order to become efficient in cosmic ray background rejection, a stereoscopic view of the Cherenkov flashes was required: two (or more) Cherenkov images of the shower should have axes pointing toward the arrival direction, the superimposition of which allows the identification of the source [141]. A third generation of detectors started with the High Energy Stereoscopic System (H.E.S.S.), the Major Atmospheric Gamma Imaging Cherenkov Telescopes (MAGIC) and the Very Energetic Radiation Imaging Telescope Array System (VERITAS) collaborations. Nowadays, these facilities are still thriving with scientific discoveries [40] [42] [41] [108].

MAGIC. MAGIC[3] is a system of two Cherenkov telescopes of 17 m in diameter, dedicated to the observation of the gamma-ray sky in the very-high energy domain from about 30 GeV up to tens of TeV. The telescopes are located at a height of 2200 m above the sea level, on the Roque de los Muchachos

[3] `https://magic.mpp.mpg.de/`

European Northern Observatory on the Canary Island of La Palma where CTA North will be located. The first of MAGIC telescopes (MAGIC-I) has been operating since 2004 and MAGIC-II followed five years after, in 2009. The baseline is of 85 m and the telescopes usually observe in stereoscopic mode. Only events triggering both telescopes in a 180 ns time window are recorded and analysed, with angular resolution of 0.11° at 30 GeV and 0.08° at 1 TeV (at 68% containment radius). MAGIC integral flux sensitivity has been calculated from MC simulation and results in about 5% of the Crab flux at E>100 GeV and 2% at E>1 TeV [142]. The technical details of the telescopes are summarised in Table 1.1. In the context of GRB science, a low-energy threshold and fast repositioning are the top two requirements, met by the MAGIC system. The former is needed to observe radiation unabsorbed by the Extragalactic Background Light (EBL) while the latter relates to the transient and brief nature (from fraction of a second to some hundreds) of these sources. One of the most recent and outstanding results from the MAGIC collaboration was the first TeV detection of a GRB (GRB190114C) afterglow component [40] [42].

H.E.S.S. The first array of Cherenkov telescope operating in stereoscopic mode was H.E.S.S.[4], located in the Khomas Highland of Namibia at about 1800 m of altitude. Operations started in 2003 with a four telescopes (12 m in diameter) system arranged in square-like geometry with 120 m of baseline. A fifth, larger telescope (27 m in diameter) was added to the system in 2012 at the centre of the configuration, improving angular resolution, sensitivity and energy coverage. It has a significantly larger field of view (of about 5° in diameter) compared to other third generation IACTs. The peak energy resolution is of about $\Delta E/E \sim$ 15-20% and its angular resolution is of about $\theta_{68} \sim 0.07$ ° at 1 TeV (at 68% containment radius). The system sensitivity is 1% of the Crab flux for 25 h of observations near zenith, for point sources [143]. H.E.S.S. has been a very competitive system for GRB science, due to the large field of view that can more easily cover the coarse localisation accuracy of satellite-born science alerts. Worthy of mention are the recent detections of GRB180720B [41] and GRB190829A [108].

VERITAS. Located at the Fred Lawrence Whipple Observatory in southern Arizona, VERITAS[5] is an array of four Cherenkov telescopes with dishes of 12 m in diameter. First light dates back to 2006. The system field of view is of about 3.5° in diameter and the energy coverage is between 85 GeV and 30 TeV. At 1 TeV VERITAS has $\Delta E/E \sim$17% energy resolution and $\theta_{68} \sim 0.08°$ angular resolution (at 68% containment radius). The system sensitivity for a point source is of about 1% of the Crab flux in less than 25 h and 10% in 25 min. The observing strategy of this facility is to assign the highest priority to GRB observations. The telescope slewing rate of $\sim 1°$/s both in azimuth and elevation has been key for the follow-up of these transients. Data taking of the majority of those could be started after about 180 s from the burst trigger.

1.3 Outline of the thesis content

The Cherenkov Telescope Array will be introduced in Chapter 2. The concept behind the proposal-driven Observatory will be briefly presented in Section 2.1, alongside the description of the Consortium. In Section 2.2 the focus will be moved onto the telescopes description and performances, which can be compared to Section 1.2 for comparison with the currently available technology. Section 2.3, 2.4 and 2.5 will be dedicated to CTA science drives, the possibilities for science beyond gamma-rays and the foreseeable synergies for MWL and MM astronomy, respectively.

The context for Real-Time Analysis will be introduced in Chapter 3 with some details on the architecture and a description of the tasks the RTA will be charged with. The key role played by the RTA in the follow-up of GW transients (GRB in particular) will be touched in Section 3.1. Short-timescale sensitivity, which is extremely important to constrain when data analysis must be as fast and as accurate as it can be, will be addressed in Section 3.2. As this work implements a full-FoV maximum likelihood analysis, rather than the most commonly use aperture photometry, the method will be summarised in Section 3.4. Section 3.5 is dedicated to the enunciate of Wilks' theorem which, for reliable science, an analysis method must abide to in order to claim awareness and control

[4] `https://www.mpi-hd.mpg.de/hfm/HESS/`
[5] `https://veritas.sao.arizona.edu/`

	MAGIC	H.E.S.S.	VERITAS
Site	La Palma (N)	Namibia (S)	Arizona (N)
Telescopes	2	4 + 1	4
Energy range	50 Gev - 10 TeV	30 GeV - 100 TeV	85 GeV - 30 TeV
θ_{68} at 1 TeV	0.08	0.07	0.08
$\Delta E/E$ at 1 TeV	20%	15-20%	17%
Mirror size (m)	17	12, 28	12
FoV diameter (deg)	3.5	3.2, 5	3.5
Photodetector	PMT	PMT, PMT	PMT
Camera pixels	1039	960, 2048	499
Pixel size (deg)	0.1	0.16, 0.067	0.15
Maximum t_{slew} (s)	$> 7°/s$	$> 1.6°/s$, $> 3.3°/min$	$1°/s$

Table 1.1: Indicative performance values of currently operating IACTs. The (N) and (S) specifics indicate the location in the northern or southern hemisphere, respectively. The angular resolution (θ_{68}) and energy resolution ($\Delta E/E$) at 1 TeV are given for 60% containment radius.

over the false alarm rate. Lastly, Section 3.6 will address the issue of sensitivity degradation after an introduction of the IRFs in Section 3.3.

The science case being gamma-ray bursts, Chapter 4 will be entirely dedicated to this class of transients after an introduction of the transient program proposed for CTA (Section 4.1). GRB will presented in Section 4.2. Section 4.2.1 will introduce the fireball model, which is currently used to described the physical nature of the phenomena, and Section 4.2.2 will be dedicated to the main mechanisms believed responsible for the prompt and afterglow radiation. A short paragraph on the progenitors of short and long GRBs can be found in Section 4.2.3. The proposed observing strategy of GRBs for CTA is reported in Section 4.2, along with the expected science return (Section 4.4). Section 4.6.1 is dedicated to the GW COSMoS catalogue and the POSyTIVE project. In Section 4.5 the current state of the art for GRB science will be briefly summarised. Being GRBs extra-galactic sources of very-high energy, an introduction to the EBL is due, alongside a description of the model that has been used in this work. This can be found in Section 4.6.2. The Section concludes with the science case introduction and a detailed description of the source template (Section 4.6 and 4.6.3 respectively).

In Chapter 5 the prototype pipeline developed for the RTA will be described. Firstly, the used science tools will be presented in Section 5.1 and the the outline of the code will be described in Section 5.2, with focus on the inputs, outputs and the source simulations (Section 5.2.1 and 5.2.2 respectively). The natively implemented utilities are summarised in Section 5.3 with functionalities dedicated to the analysis (Section 5.3.1) and the models handling (Section 5.3.2). Some miscellaneous and side scripts can be found in Section 5.3.3 and 5.3.4, respectively. Section 5.4 concludes with a summary on the post-processing procedures.

The results of this research are presented in Chapter 6. Firstly, the assessment of the false alarm rate is addressed in Section 6.1. The performance of the peak-search algorithm is reported in Section 6.2 with lower boundaries on the minimum exposure time required for efficient blind-search of a GRB afterglow in the RTA context. Section 6.3 furthers the statistical study on the constraints of the source localisation accuracy, the detection rates and the integral photon flux estimation alongside the detection significance[6]. In Section 6.4 the results from the mocked blind-search and follow up (abiding to CTA proposed strategy and RTA requirements) will be presented. Finally, in Section 6.5 a preliminary investigation on a sample of differently scaled source intensities will be presented.

The dissertation concludes with Chapter 7 where the main results of this research will be summarised. Foreseeable improvements, tests and implementations will also be mentioned, alongside future prospects. At the end (Appendix 7) a selection of additional information on the pipeline and further plots will be offered for completeness.

[6]The significance presented in this work has yet to be post-trial corrected.

Chapter 2

The Cherenkov Telescope Array

In this chapter CTA will be described in detail, as well as introducing how the Observatory will operate. A generic introduction will be offered before presenting the facility and the Consortium of the CTA project (Section 2.1). Telescopes technical properties, site description and array configurations will be outlined in Section 2.2. The main science topics will be briefly presented in Section 2.3. In Section 2.4 the focus is moved onto non gamma-ray science possibility offered by a facility such as CTA. The chapter ends with a summary of MM/MWL synergies (Section 2.5) for which CTA may play a key role in the future.

The Cherenkov Telescope Array (CTA) will be the largest ground-based gamma-ray detection observatory of the next decade (∼2025-2030), with more than 100 telescopes in the northern and southern hemispheres. It will look at the very high energy gamma-ray sky with the highest energy resolution ($\Delta E/E < 0.1$ in 1-10 TeV range, for 68% of containment radius as shown in Figure 2.2(b)) ever obtained, with unprecedented sensitivity (over 10 times better than what is currently achieved by other IACTs and three orders of magnitude higher than Fermi-LAT at 30 GeV on hour timescale as shown in Figure 2.1) paired with a broad energy coverage (from 20 GeV up to 300 TeV) and a large field of view (up to $\sim 10^\circ$ in diameter) which will allow for exceptional survey capabilities as well. Predictions are of three orders of magnitude higher sensitivity on hour timescale than Fermi-LAT at 30 GeV. Its improved angular resolution ($\lesssim 0.05^\circ$ at $E \geq 1$ TeV as shown in Figure 2.2(a)) will best that of any existing instrument operating, at the time of writing, above the X-ray band. This comes with the benefit of detailed imaging and thus more precise morphology of many gamma-ray sources.

The current Cherenkov telescope arrays consist of 2 to 5 telescopes only (i.e. H.E.S.S., MAGIC, VERITAS); they can reach sensitivities of about 1% of the Crab flux at energies between 0.1-10 TeV[1]. This value degrades further towards lower energies due to the low accuracy of event rejection (background-limited range), whilst deteriorates towards higher energies because of the limited number of gamma-rays. The goal with CTA is to improve sensitivity by a factor of 10 within the currently accessible energy domain, and to extend the energy range with respect to existing IACTs. A combination of differently sized telescopes is required to optimise the array sensitivity over its broad energy range: *i)* large telescopes, of 23 m in diameter, cover the lowest energies from 20 to 3 TeV; *ii)* medium ones, of 12 m in diameter, cover the core energy range between 80 GeV and 50 TeV; *iii)* a number of small telescopes (7 m in diameter) are designed to cover energies from 1 TeV up to 300 TeV. Also, in order to

[1] $1 mCrab = 5.07 \times 10^{-13} ph/cm^2/s$ for a minimum energy threshold of 125 GeV, as defined in [62]

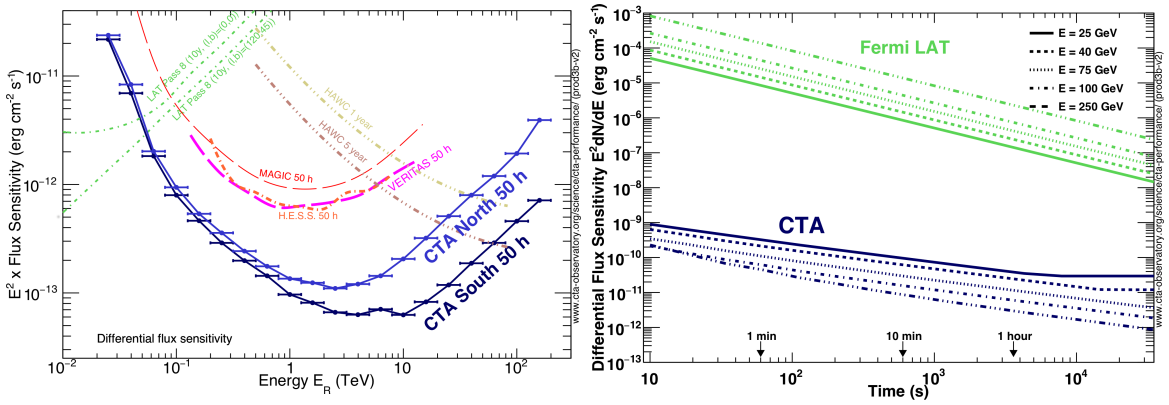

(a) (b)

Figure 2.1: **Left** The differential sensitivity shown below is defined as the minimum flux needed by CTA to obtain a 5σ detection of a point-like source, calculated in non-overlapping logarithmic energy bins (five per decade). Besides the significant detection, at least ten detected gamma-rays per energy bin and a signal/background ratio of at least 1/20 was required. Instrument response functions are provided for 0.5, 5 and 50 hours. The curves shown allow only a rough comparison of the sensitivity of the different instruments, as the method of calculation and the criteria applied are not identical. **Right** Differential flux sensitivity of CTA at selected energies as function of observing time in comparison with the Fermi LAT instrument (Pass 8 analysis, extragalactic background, standard survey observing mode). Note that especially for exposures longer than several hours, the restrictions on observability of a transient object are much stricter for CTA than for the Fermi LAT. CTA will be able to observe objects above 20 degrees elevation during dark sky conditions. The differential flux sensitivity shown above are for observations near 70-degree elevation angles. **Credits:** CTA Collaboration (left), CTAO (right).

achieve a substantially improved sensitivity at the highest energies, CTA requires a collection area up to some km^2 at higher energies (Figure 2.2(c)). This means spreading numerous telescopes over a large area. With one-to-two order of magnitude larger collecting area, CTA will dominate the time-domain astrophysical scene in gamma-rays.

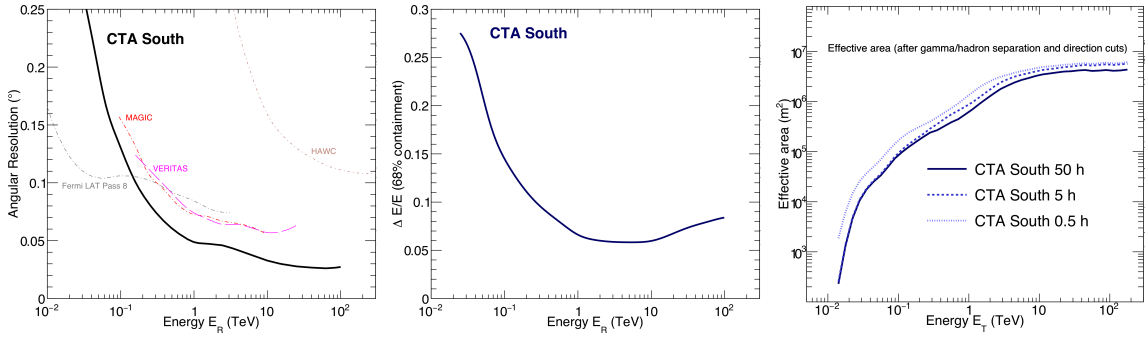

Figure 2.2: **Left:** The angular resolution vs. reconstructed energy curve shows the angle within which 68% of reconstructed gamma-rays are contained, relative to their true direction. Note that this analysis is not optimised to provide the best possible angular resolution, but rather the best point-source sensitivity (compatible with the minimum required angular resolution). Here CTA South performance is compared with other instruments, both IACTs and space-born. **Centre:** The energy resolution $\Delta E/E$ is obtained from the distribution of $(E_R - E_T)/E_T$, where R and T refer to the reconstructed and true energies of gamma-ray events recorded by CTA. $\Delta E/E$ is the half-width of the interval around 0 which contains 68% of the distribution. The plot shows the energy resolution as a function of reconstructed energy for CTA South. **Right:** The effective collection area for gamma-rays from a point-like source is shown below vs. E_T for CTA South. **Credit:** CTAO.

The two sites are located one in each hemisphere, giving CTA access to full sky coverage and thus maximising the chances of observing rarest phenomena such as nearby supernovae (SN), gamma-ray burst (GRB) and gravitational-waves (GW) counterparts. The full-array design is of 99 telescopes placed in the southern hemisphere and 19 on the northern site. This ambitious project and its science goals were conceived by the CTA Consortium[2] (CTAC), an international collaboration including more than 1,500 members from over 200 institutes in 31 countries. Moreover, for the first time in the

[2]https://www.cta-observatory.org/about/cta-consortium/

Very-High Energy astronomy, the CTA observatory will be an open, proposal-driven observatory. Data will be publicly available on a public archive after a predefined proprietary period (typically one year). The Core Program proposal prepared by the CTA Consortium, with community inputs, consists in highly motivated observations. It encompasses approximately 40% of the available observing time over the first ten years of CTA operation and it is built on individual Key Science Projects (KSPs) [1], developed and detailed by CTA Consortium.

2.1 CTA Consortium, Observatory and user access

The northern and southern CTA arrays will constitute the CTA Observatory (CTAO), which will be the first ground-based gamma-ray observatory open to the world-wide astronomical and particle physics communities as a resource for data from unique high-energy astronomical observations. As mentioned, CTA will be operated as a proposal-driven open observatory unlike existing ground-based VHE instruments. This is expected to significantly boost the scientific output of CTA by engaging a much wider research community. Observations will be carried out by observatory operators and data will be calibrated, reduced and made available to the principle investigator in standard astronomical data format. After a proprietary period, data will be made openly available through the CTA data archive. During the first phase of operation, observation time will be split between guest observer time and KSPs, such as large-scale surveys aimed at providing legacy data sets. Operations are planned to start during the construction phase, as soon as the first telescopes are ready to conduct competitive science observations. These cover day-to-day use of the arrays and sub-arrays, continuous hardware and software maintenance, proposal handling and evaluation, automated analysis and user support as well as long-term programme for upgrades and improvements. Frequent modifications to the scheduled observing programme can be expected for several reasons, first of all the transient follow-up program on top of changing atmospheric conditions.

Figure 2.3: October 21-25, 2019. The Consortium meets at the CTAO Head-Quarters in Bologna. **Credit:** Tiziana Abegg, CTAO

2.2 Telescopes

Scientists have run numerous simulations in order to define which arrays configurations would best maximise the performances, not only for the full array but accounting for sub-array configurations as well [31]. Configurations of clusters of telescopes could work on parallel and independent observations, allowing for observation time optimisation and for a more targeted science (i.e. sensitivity-wise and energy-wise). Since construction is expected to span over the next few years, planning ahead which telescopes to prioritise will allow for an early-phase commissioning of CTA with a smaller but optimised set of the arrays.

The **northern hemisphere array**[3] will be located on the existing site of the Instituto de Astrofisica de Canarias' (IAC's) Observatorio del Roque de los Muchachos in Villa de Garafia on the island of La Palma, in the Canary Islands. At 2,200 metres of altitude and nestled on a plateau below the rim of an extinct volcanic crater, the site already hosts an operating gamma-ray observatory, the Major Atmospheric Gamma Ray Imaging Cherenkov (MAGIC) telescopes, as well as a wide variety of optical telescopes of various sizes. More limited in size, the northern hemisphere array will focus on the low and core energy ranges, from 20 GeV up to about 50 TeV. Out of the three types of telescopes designed for CTA, only two will be hosted in the configuration: 4 Large-Sized Telescopes (LSTs) and 15 Medium-Sized Telescopes (MSTs), as in Figure 2.4.

[3]Array Coordinates: longitude: 17° 53' 31.218" West, latitude: 28° 45' 43.7904" North.

The **southern hemisphere array**[4] planned site is less than 10 km southeast of the European Southern Observatory's (ESO's) existing Paranal Observatory in the Atacama Desert in Chile, one of the driest and most isolated regions on Earth. This array will span the entire energy range of CTA, covering gamma-ray energies from 20 GeV to 300 TeV. The plan is for the site to host a much larger array of all three classes of CTA telescopes, spread over 4 km^2: 4 LSTs to capture the low-energy sensitivity of CTA, 25 MSTs to cover CTA's core energy range and 70 SSTs to cover CTA's highest energy gamma-rays (Figure 2.4).

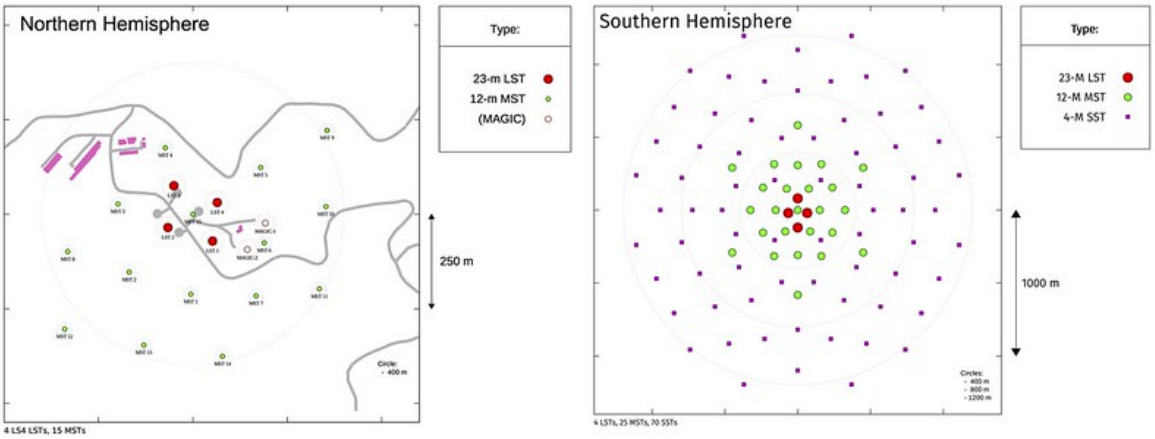

Figure 2.4: Array layout. On the left is the northern hemisphere array configuration, with its planned 4 LSTs and 15 MSTs plus the two MAGIC telescopes already on site. On the right is the southern hemisphere array configuration featuring 4 LSTs, 25 MSTs and 70 SSTs. **Credit:** CTA Collaboration.

To achieve high quality performance, the optical system should be designed as to achieve a point spread function matching the pixel size of the camera. The electronics for signal capture and triggering should similarly provide a bandwidth matched to the length of Cherenkov pulses of a few nanoseconds. Triggering strategies are also influential to the final performance of an array. The Cherenkov light produced by an air shower has to be separated in real-time from the night's high flux sky background photons and the Cherenkov signal due to hadron-induced air showers. This distinction is based on individual images and the stereoscopic combination of images from several telescopes. From a single Cherenkov telescope the raw data streams is far too high to be fully recorded, it will be necessary to reduce a volume of typically 10 terabytes (TB) of raw data per night to a few tens of megabytes (MB) of high-level data. Another important parameter is, of course, the field of view (FoV) of each telescope. It determines the ability for efficient study of extended sources and diffuse emission regions, as well as for large-scale surveys and clustered sources. On top of, of course, allowing for a more uniform response from the camera and reducing the background systematics. In Table 2.1, the technical specification of CTA are summarised for each telescope design. Values can be compared with technical specifications of existing IACTs, summarised in Table 1.1 of Chapter 1.

Large-Sized Telescopes (LST) The LST project team consists of more than 100 scientists from ten countries: Brazil, Croatia, France, Germany, India, Italy, Japan, Poland, Spain and Sweden. Large mirrors are required to detect signal of lower energies since a small amount of Cherenkov light is produced. The centres of both arrays will thus be covered by four LSTs in order to provide the full-system sensitivity between 20 and 150 GeV. These gigantic telescopes of 23 meters in diameter have a parabolic reflective surface, supported by a tubular structure made of reinforced carbon fibre and steel tubes. These alt-azimuth telescopes stand 45 meters tall and weigh around 100 tonnes, yet their are challenged to have a re-position time within 20-30 seconds at pointing precision better than 14 arc-seconds. The diameter of the field of view (FoV) is of about 4.3°. Both the re-positioning speed and the low energy threshold provided by the LSTs are critical for CTA studies high redshift

[4]Array Coordinates: longitude: 70° 18' 58.84" West, latitude: 24° 41' 0.34" South.

(a) (b) (c)

Figure 2.5: **Left** On Wednesday 10 October 2018 on the northern array site of the Cherenkov Telescope Array (CTA) took place the inauguration of the first prototype Large-Sized Telescope (LST). **Centre** On 17 January 2019, a prototype telescope proposed for the Cherenkov Telescope Array (CTA), the prototype Schwarzschild-Couder Telescope (pSCT) was unveiled in a special inauguration event. **Right** SST-2M ASTRI Prototype, Serra La Nave, Italy, was inaugurated in 2014. In December 2018 it observed gamma-ray emission from the Crab Nebulae, becoming the first world-wide double-mirrors Cherenkov telescope producing an astronomical observation. **Credit:** Akira Okumura (left); Amy Oliver, Fred Lawrence Whipple Observatory, Center for Astrophysics | Harvard & Smithsonian (centre); CTA Collaboration (right).

AGNs and gamma-raybursts. The LSTs will expand the science reach to cosmological distances and fainter sources with soft energy spectra. With a focal length of 28 meters and a reflective surface of 370 m^2, they collect and focus the Cherenkov light into the LST Camera. The camera weights less than 2 tonnes and has a total number of channels equal to 1,855 divided into 265 photo-multiplier tube (PMT) modules. PMTs with a peak quantum efficiency of 42% are used as photo-sensors to convert the light into electrical signals. The camera has been designed for maximum compactness and low weight, cost and power consumption while providing optimal performance at low energies. Each pixel incorporates a photo-sensor and the corresponding readout electronics. These electronics are based on technology developed at the Paul Scherrer Institute in Switzerland and currently used by several experiments, among which the MAGIC Cherenkov telescopes. The camera trigger strategy is based on the shower topology and the temporal evolution of the Cherenkov signal produced in the camera. The analogue signals from the photo-sensors are conditioned and processed by dedicated algorithms that look for extremely short but compact light flashes. Furthermore, the LST cameras are interconnected in order to form an on-line coincidence trigger among the telescopes, which helps suppress accidental triggers by up to a factor of 100. On Friday, 9 October 2015, the first stone-laying ceremony for LST-1 prototype took place and on Wednesday, 10 October 2018, more than 200 guests from around the world gathered on the northern array site to celebrate its inauguration. On the night of 14-15 December 2018 the first Cherenkov light was recorded.

Medium-Sized Telescope (MST) The MST design is still undergoing harmonisation. The telescopes will be built by an international collaboration of institutes and universities from Austria, Germany, France, Brazil, Poland, Spain, Switzerland and the Italy. MSTs will provide full-system sensitivity within 150 GeV and 5 TeV. The planned baseline for CTA includes 40 MSTs in total, of which 25 in the southern hemisphere and 15 in the northern hemisphere. The MST is a modified Davies-Cotton telescope with a reflector diameter of 11.5 m on a polar mount, and a focal length of 16 m. The effective mirror area is of about 88 m^2 for a weight of 82 tonnes. The positioning time to any point of the sky must fall within the requirement of 90 seconds as worst case scenario, with precision better than 7 arc-seconds. An MST prototype was deployed in Berlin in 2012 and is currently undergoing performance testing. The main purpose of the prototype is to validate the design of the individual components, test the interfaces between the mating assemblies and to define the assembly process of the product. The prototype has a fully functional drive system, cameras for pointing and tracking, sensors designed to record the behaviour response of the structure and drive system and a weather station. At present there are two different camera designs, both using photo-multiplier tubes (PMTs) with a large field of view of about 8°, enabling the MSTs to take rapid surveys of the gamma-ray sky. A first camera design (FlashCAM) would grant MSTs a 7.5° FoV dived into 1764 pixels of size of 0.17° each. The telescope readout event rates would thus be higher than 6 kHz. A

second option (NectarCAM, similar to the LST camera) would translate in a 7.7° FoV with 1855 pixels each of 0.17° in size. In this case, the telescope readout event rate is expected higher than 7 kHz.

The alternative design is the **Schwarzschild-Couder Telescope (SCT)** prototype: a dual-mirrored version of the MST. Its optical system is designed to better focus the light for greater imaging detail and improved detection of faint sources. In collaboration with the SST-2M and MST groups and institutes in Germany, Italy, Japan and Mexico, institutes in the United States have been the pioneers of the SCT design since 2006. The primary reflector mirror has a diameter of 9.7 meters whilst the secondary is 5.4 m, both segmented and designed built with active alignment, for a total effective mirror area of 41 m^2. The focal length is of about 5.6 m and its field of view covers 7.6° with a SiPM camera of 11328 pixels, each of 0.067° in size. The SCT camera is composed of the mechanical enclosure, SiPMs mounted in focal plane modules, front-end electronics with pre-amps and first level trigger, and back-plane electronics that provide the pattern trigger and data acquisition hardware. Data from nine sub-field back-planes will be merged and delivered to the SCT Camera Server using standard high-speed communication protocols. Trigger and time synchronisation signals from the back-planes will be relayed by the distributed array trigger electronics. It grants improved angular resolution as a result of a smaller point spread function (PSF) and the very large number of camera pixels.

Small-Sized Telescope (SST) These telescopes will outnumber all the others with 70 planned to be spread out over several squared kilo-meters. This is because very high-energy gamma-ray showers produce a large amount of Cherenkov light over a large area, and the SST's smaller mirror is sensitive to the highest energy gamma-rays. They will provide full system sensitivity in the energy range between 5 TeV and 300 TeV. Their positioning time must be lower than 60 seconds, with pointing precision better than 7 arc-seconds. Three prototyped were proposed for the final design: a single-mirror (SST-1M) and two dual-mirror designs (SST-2M ASTRI and SST-2M GCT). These prototypes were built by international collaborations with contributions from institutes and universities in Czech Republic, Ireland, Poland, Switzerland and Ukraine (SST-1M); in Brazil, Italy and South Africa (ASTRI); and in Australia, France, Germany, Japan, the Netherlands and the United Kingdom (GCT). A harmonization process started in 2018 and brought to the conclusion (Jun 2019) that the *"CTA-SST design should be based on the ASTRI/CHEC design (Figure 2.5c), taking into account the experience gained from all designs"*[5]. ASTRI is a dual-mirror Schwarzschild-Couder configuration paired with a compact camera based on SiPM sensors. The primary mirror has a diameter of 4.3 m and is segmented into hexagonal facets. The secondary mirror is monolithic instead, with a 1.8 m diameter. This design allows to maintain the same angular resolution and collecting area across a wide field of view with a short focal length. The camera consists of 2048 silicon photo-multiplier pixels forming approximately a 10° field of view.

2.3 Scientific drive and KSPs

As described in Section 2.1, most of the available observation time of CTA sites will be dived into open time and a Core Programme. The **Core Programme** entails a number of KSPs, multi-purpose observations designed to efficiently address the raising science questions yet to be answered. The selection of the KSPs followed a number of criteria, such as: *i)* excellent scientific case and clear advance beyond the state of the art; *ii)* production of legacy data-sets of high value to the wider community; *iii)* clear added value of the project as a KSP rather than as part of the Guest Observer Programme. This last one includes criteria like the scale of the project in terms of observing hours, the need of a coherent approach across multiple targets or pointings and the technical difficulty of performing the required analysis and hence reliance on Consortium expertise. The Core Programme was largely finalised in 2016 and can be extensively read in [1], hereafter is a brief summary.

Dark Matter (DM) Programme. In the form of Weakly Interactive Particles (WIMPs), dark matter particles can self-annihilate, converting their large rest masses into Standard Model particles, including gamma-rays. Other than that, super-symmetric models (SUSY) and other peculiar ones (along with theories with extra dimensions) yield predictions on the gamma-ray energy spectra to be

[5] `https://www.cta-observatory.org/small-sized-telescope-harmonization-process-and-status/`

	LST	MST			SST
		FlashCam	NectarCam	SCT	
Required E range	20 GeV - 3 TeV	80 GeV - 50 TeV			1 TeV - 300 TeV
Core E range	20 GeV - 150 GeV	150 GeV - 5 TeV			5 TeV - 300 TeV
Number of telescopes	4 (South) - 4 (North)	25 (South) - 15 (North)			70 (South) - 0 (North)
Primary mirror diameter	23 m	11.5		9.7	4.3
Secondary mirror diameter	-	-		5.4	1.8
Effective mirror area	370 m^2	88 m^2		41 m^2	8 m^2
Focal length	28 m	16 m		5.6 m	2.15
Total weight	103 t	82 t		80 t	19 t
FoV (diameter)	4.3°	7.5°	7.7°	7.6°	10.5
Camera pixels	1855	1764	1855	11328	2368
Pixel size	0.1°	0.17°	0.17°	0.067°	0.19°
Photodetector	PMT	PMT	PMT	SiPM	SiPM
Data rate	24 Gb/s	12 Gb/s			2 Gb/s
Maximum t_{slew}	30 s	90 s			60 s
Pointing precision	<14 arcsec	<7 arcsec		<10 arcsec	<7 arcsec
Observable sky	Any astrophysical object with elevation > 24°				
θ_{68} at 1 TeV	$\lesssim 0.05°$				
$\Delta E/E$ at 1 TeV	$\lesssim 10\%$				

Table 2.1: Summary of CTA telescopes technical details.

expected from annihilations, essential ingredients towards the prediction of the sensitivity of indirect searches. Of particular importance for CTA [54] [55] is the effort for the discovery of the nature of dark matter through a positive detection. The Core Programme primarily targets the Galactic halo which, with its dark matter profile thought as cusp-like, has substantial chances of being an optimal detection site for most popular WIMPs models. Alternative targets are: ultra-faint dwarf galaxies, the Large Magellanic Cloud as well as the Galactic plane and Extragalactic surveys.

Galactic Centre (GC). This KSP comprises a deep exposure of the inner few degrees of the Milky Way, complemented by an extended survey which is going to explore regions not yet covered by existing VHE instruments. Within a few degrees from the Galactic centre are contained a wide variety of possible targets, including the nearest super-massive black hole, dense molecular clouds, star forming regions (SFR), supernova remnants and pulsar wind nebulae alongside arc-like radio structures as well as the base of what might be large-scale Galactic outflows. This region has already yielded massive results [56] and CTA's high-precision measurements are expected to allow the scientific community to study this complex region with unprecedented spatial and spectral detail. The CTA Consortium will organise coordinated observations in collaboration of other wavebands instruments to gain detailed variability studies and produce an invaluable legacy.

Galactic Plane Survey (GPS). At the very foundation of Galactic science at all photon energies, the Galactic Plane Survey will fulfil a number of important goals. It aims at: *i)* providing a census of Galactic VHE gamma-ray sources such as supernova remnants (SNRs), pulsar wind nebulae (PWNe) and binary systems on top of new sources and substantially increasing the source count within the pre-defined region; *ii)* identifying a list of promising targets for follow-up observations, such as new gamma-ray binaries and PeVatrons[6] candidates; *iii)* determining the properties of the diffuse emission from the Galactic plane; *iv)* producing a multi-purpose, legacy data-set which encompasses the complete Galactic plane at VHE and which will have long-lasting value to the entire scientific community; *v)* discovering new and unexpected phenomena in the Milky Way, i.e. new source classes, new types of transients and variable behaviour.

Large Magellanic Cloud (LMC) Survey. The Large Magellanic Cloud hosts a number of objects susceptible of extraordinary science due to its proximity and satellite nature. The current Fermi-LAT [58] [60] and H.E.S.S. [61] [59] instruments have opened a path for CTA in observing the LMC. Unique opportunities arise to further and deeper explore the Galaxy thanks to the unprecedented sensitivity and angular resolution of CTA.

[6]Sources capable of accelerating particles up to energies of 10^{15} eV and higher.

Extragalactic Survey. The extragalactic blind survey of 25% of the total sky is expected to become one of the main legacies of CTA [63]. It is aimed at constructing an unbiased extragalactic catalogue of VHE sources, with integral sensitivity limit of approximately 6 mCrab above 125 GeV. Predictions derived from extensive simulation studies seem to point out more efficient achievements for the KSP objectives (especially detection of serendipitous flaring sources) if the survey was to be carried out with divergent pointing mode [28] (Figure 2.6). The list of potential discoveries is wide and varied, including: *i)* unbiased determination of yet unknown AGN (BL lac and possibly FSRQs); *ii)* extreme blazars peaking in the 100 GeV - 10 TeV energy range; *iii)* serendipitous detection of fast flaring sources which would not be detectable in short observation time by lower sensitivity observatories; *iv)* gamma-ray emission from yet undetected source classes *v)* discovery of dark sources with no astrophysical counterpart which could point toward a possible signal from DM annihilation; *vi)* possible detection of GRBs in the prompt phase (this topic would particularly benefit from the performance of CTA in divergent mode); *vii)* the study of large scale anisotropies in the electron spectrum at energies between 100 GeV and a few TeV.

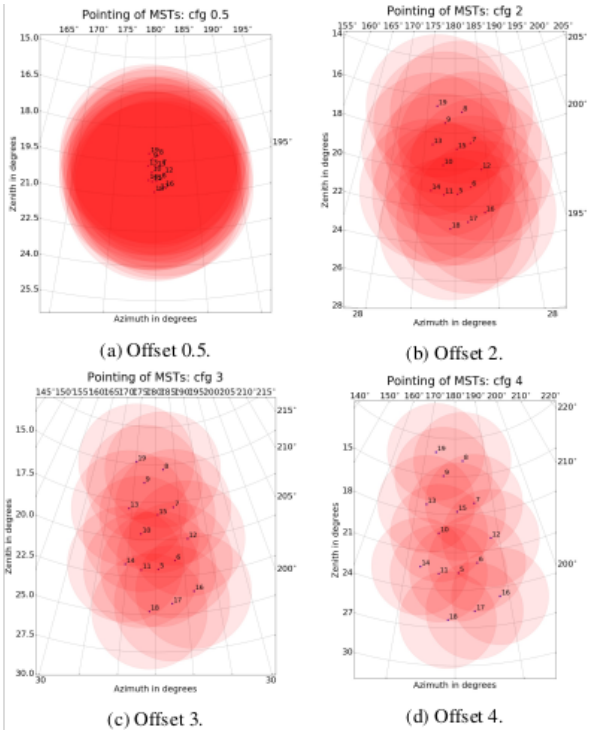

Figure 2.6: Fields of view in polar coordinates for different "on-axis" configurations with possible divergent pointings (offsets are in arbitrary units [28]). The MST cameras herein used is the NectarCam (Section 2.2) with a field of view of 7.7° in diameter. **Credit:** figure taken from Donini et al. 2019.

> **Divergent pointing mode.** In the divergent pointing mode, CTA telescopes would point to a location slightly off-set from their neighbours, in order to cover a larger portion of the area. Preliminary simulations [28] have been run based on CTA configuration without LSTs, yielding promising results. A field of view of 14° in diameter can be achieved while still containing sensitivity fluctuation below a factor of 2 across the entire FoV. Albeit the angular and energy resolution will suffer a degradation up to a factor of two worst with respect to the parallel pointing mode, the sensitivity would in increase up to a factor of 1.5, making the strategy highly desirable for the search of transients and GRBs in particular.

Transients. The word "transient" denotes a wide range of astrophysical phenomena. Emitters of very-high energy gamma-rays, transients are objects which explode or flare up in unpredictable fashion. Their timescales spans from milliseconds to years, hardly facilitating their detailed observation. One of the key strength of CTA will be its performances for transients' observation and discovery [64], both from follow-up of external alerts and from internal ones. The proposal of follow-up observations for a targets either triggered from CTA itself or other monitoring instruments, alongside an unbiased survey with divergent pointing mode. The transient classes targeted in this KSP are the following: *i)* gamma-ray bursts [47] [66]; *ii)* Galactic transients [65] [67] [68]; *iii)* X-ray, optical and radio transients [69] [70], including AGN; *iv)* high-energy neutrino transients [71] [72] (also including AGN) and GW transients [73] [74] [75]; *v)* serendipitous VHE transients [33] [35].

Cosmic Ray PeVatrons. The spectrum of cosmic rays is largely dominated by protons up to the so called *knee* of the spectrum (energies of a few PeV and above). This feature signs the steepening of

the spectrum from $\sim E^{-2.7}$ to $\sim E^{-3.0}$, where E is the particle energy. The chemical composition also changes and becomes heavier [76]. PeVatrons accelerators candidates are widely suspected to be SNRs [77]. These sources are, in fact, able to satisfy the cosmic-ray energy requirement if they can somehow convert $\sim 10\%$ of the supernova energy into accelerated particles. The acceleration channel is thought to be via diffuse shock acceleration, accompanied by the amplification of the magnetic field which can boost the acceleration of protons up to energy of the *knee*, and beyond. It is also suggested to search for diffuse gamma-ray emission [78] [79] from the vicinity of prominent gamma-ray bright SNRs, motivated by the belief that PeV particles are expected to quickly escape the SNR shock and then propagate diffusely in the ambient medium surrounding the remnant.

Star-forming systems. Connected to the cosmic rays studies included in other KSP, the star-forming systems programme is designed to better understand cosmic rays properties in star-forming environments [80]. Since cosmic rays are believed to be important regulators of the star-forming process itself, it is essential to investigate their origin, their propagation and their interaction with the inter-stellar medium (ISM). CTA will observe over six orders of magnitude in the star-forming rate (SFR) and thus help to unveil the relationship between high-energy particles and the star-forming process.

Active Galactic Nuclei. AGN are known emitters of broad wavelength radiation, covering the entirety of the electromagnetic spectrum up to multi-TeV. Fluctuations can be of timescales ranging from several years to a few minutes. At present, they account for roughly 40% of the VHE sources observable via ground-based telescope science. Being AGN active galaxies hosting supermassive black holes (SMBHs) that eject relativistic outflows, they represent a unique tool to probe the physics of extreme environments. Topics of interest for this KSP include: accretion physics, jet formation, interaction of the black hole magnetosphere with the accretion disk corona, relativistic interaction processes and general relativity. Exploration of averaged spectra from the high energy gamma-ray band covered by Fermi-LAT has shown that more than 200 blazars of different classes and several radio galaxies should be detectable with acceptable exposure times, up to redshift of $z \sim 2$ [81].

Clusters of galaxies. Clusters of galaxies represent the larger stage of structure formation, with them being the most massive gravitationally bound system in the universe. Their radii are of the order of few Mpc and their masses range from $10^{14}\,M_{\odot}$ to $10^{15}\,M_{\odot}$, which comprise of Dark Matter for the 80% of the total. Roughly 5% and 15% of their masses is related to their galaxies and gas contributions [83], respectively.

2.4 Beyond gamma-rays

Albeit CTA is designed as a gamma-ray observatory, as part of its normal operation it will collect an enormous quantity of valuable information on charged cosmic rays. The highest energy cosmic-ray electrons and heavy nuclei are of particular interest, especially in the search for their associated particle accelerators. Through the separation of their direct Cherenkov light emissions CTA will be able to provide insights on related production and acceleration channels. Among other uses of the very large optical-photon collection area, it is possible to include the use of interferometry during longer integration time observations of optical targets. This would provide outstanding angular resolution at blue wavelengths for bright sources. Most of these topics can be run in parallel with the gamma-ray data taking, while those which would interfere with the major science operations could likely make use of the bright moonlight time. This of course works towards enhancing the science return from CTA without negative impacts on the KSP goals.

Cosmic ray nuclei. One of the still open question of modern astrophysics concerns the origin and acceleration of cosmic rays. Over the past few decades a general consensus has been reached for SNRs to likely be the main sources up to energies of the spectrum's knee ($\sim 3PeV$). Confirmation and direct proof is among CTA major science goals, while gamma-ray observations provide a view of the accelerators themselves, the observatory will also address the topic via direct detection. As already mentioned, the composition around the knee feature is of particular interest. The reasons behind the

steepening of the spectrum around this energy threshold whilst suspected to be related to the maximum energy galactic accelerators can speed the particles up to, is yet not fully understood. This maximum energy should increase with the rigidity (rigidity = momentum/charge) of the particle and therefore lead to an enrichment of heavier nuclei with increasing energy at the knee. KASCADE collaboration has reported experimental evidence, although the analysis is challenged by the dependence upon the hadronic interaction models [38]. To answer some of the open questions it is necessary to perform composition measurements above 100 TeV, whereas there lays the limits of balloon and space born science. At energies of a few PeV it becomes doable to detect secondary shower particles from the ground [96] [97] albeit systematic uncertainties related to the simulation of hadronic showers are going to affect the performances.

Cosmic ray electrons. The multi-TeV energy regime is of particular interest for the cosmic ray electrons searches, because it has the unique feature of reflecting the situation of our local neighbourhood. On top of, naturally, the potential signatures of dark matter annihilation in the electron spectrum [98]. Regardless of the small fraction of the cosmic rays represented by electrons (about 1% at GeV energies) studying this component still offers a wide range of scientific opportunities. In the VHE domain, the lifetime of cosmic ray electrons is severely limited by radiative losses, due to synchrotron emission in interstellar magnetic fields and inverse-Compton scattering on starlight, IR-light and cosmic microwave background light (CMB), hence restricting the distances at which they can propagate. In other words, it implies that cosmic ray electrons of TeV energies must originate within the local universe [100] [99]. Within a kpc distance there only a handful of sources able to contribute and their contribution can have great impact on imprinting their presence in the power-law form of the spectrum seen at lower energies. It means that VHE electrons might be a very unique tool for studying the local universe in terms of single accelerators.

Optical measurements. Diffraction-limited optical aperture synthesis over kilometre baselines, not dissimilar from how radio interferometers are operated, has somewhat been an astronomical utopia. It would allow for stellar surface imaging, time evolution and observation of interaction of stellar winds and gas flows in binary systems. The current best resolution in optical astronomy comes from amplitude (phase) interferometry which combines the light from nearby telescopes (i.e. VLT interferometer and CHARA array). Expanding the baseline to kilometre's order is everything but practical, either on ground or in space. The optical and atmospheric stability required for such a project goes down to a small fraction of optical wavelength. Also, optical light, contrary to radio-waves, cannot be copied with retained phase but needs to be split up by beam-splitters to achieve interference among multiple telescope pairs. These limits, though, do not come into play if *intensity interferometry* is the sought observational technique. It was once developed in order to measure stellar sizes by an Australia-based instrument, at Narrabri [39]. Advantages from this method arise from its insensitivity to either atmospheric turbulence or telescope optical imperfections, enabling very long baselines as well as observation at very short optical wavelengths. The drawbacks are of course that of required precision related to the electronic components down to the nanosecond timescale, high photon statistics hence large and widely distributed flux collectors, fast detectors and a large funding budget.

Figure 2.7: The Narrabri Stellar Intensity Interferometer. **Credit:** figure taken from Peter G. Tuthill, 2014.

2.5 Synergies

Nowadays, having access to complementary observations at other wavelengths (MWL astronomy), or via other messengers (MM astronomy), of the same science target or sky region is an extremely valuable feature. Far from claiming completeness, here are a handful of conveniently grouped foresighted synergies.

Radio to millimetre. Combining the results of VHE observations with radio measurements can provide limits on the electron density without any need for assumptions on magnetic field strengths, it also allows to find the most dominant process among several on-going others. Through Faraday rotation, radio measurements can also provide ephemeridies of known pulsars which can guide CTA's search for gamma-ray pulsations. Fast Radio Bursts (FRBs) have also been an interesting topic for the most recent radio science and with CTA it might be possible to find gamma-rays counterparts of these still mysterious objects. Sub-millimetre wavelengths complement CTA science with detailed understanding of the environment into which shock waves propagate and, thus, through which accelerated particles are transported and interact. It has also become clear that the sub-millimetre range has peculiar impact on studying the particle-acceleration processed in micro-quasars' jets, which adds to the already wide pool of benefits. The major collaborations are pictured to be with facilities that work at degree-scale in survey mode and whose beam sizes would match to CTA's arc-minute resolution.

Infra-red (IR), visible (V) and ultra-violet (UV). Many compact high energy sources emit detectable levels of synchrotron emission. Moreover, it can display very fast variability. Examples are blazars, micro-quasars and pulsar wind-nebulae. This scenario makes OIR a new frontier for MWL exploration, especially in transient alerts generation. Additionally it should also be considered the technique of optical polarimetry even though, contrary to i.e. radio astronomy, it has not been of much interest for MWL studies of VHE sources thus far. It is becoming apparent that polarisation offers an ideal method for isolating the non-thermal component in cases of mixed emission. Polarimetry can be also be used to provide new insights in broad-band spectral energy distribution (SED) correlations, on top of deriving magnetic field parameters in jets' studies, also useful to improve the modelling of SEDs and emission-region localisation. The technical requirements for basic yet valuable optical studies can be met at modest cost, hence the addition of a dedicated optical telescope to the CTA baseline is under discussion at the time of writing. It would guarantee simultaneous, high cadence monitoring of flaring sources as well as following-up transient or triggering CTA own programmes. Finally, probes on the synchrotron emission of electrons with comparable energies to those emitting inverse-Compton and detectable by CTA, can be derived by UV observations. As long as sources are not too absorbed by interstellar gas, simultaneous UV observations might be extremely useful.

X-ray and γ-ray from space. Thermal X-ray emission from gamma-ray sources can provide valuable information about plasma properties (i.e. temperatures, densities, energies). Moreover, the importance of studies of X-ray radiation via synchrotron and inverse-Compton increases as missions become capable of higher spatial resolution and sensitivity. Phenomena that are powerful enough to radiate thermal emission in the X-ray energy band are often associated with shock waves, accretion or high velocity outflows. It derives an expectancy for particle acceleration and gamma-ray emission as consequence. In particular, the hard X-ray / soft gamma-ray domain (0.1-10 MeV) represents a tremendously useful window on the non-thermal spectra of astrophysical sources. Obviously, at higher gamma energies potential synergies with CTA strengthen and the instrumental performance are a closer match to CTA. Two instruments on currently active space missions provide an overlap with CTA lower energy range, Fermi-LAT and AGILE-GRID. The combination with TeV measurements allows for the GeV range to be the key in identifying which radiative mechanisms dominate, i.e. among pion decay, bremsstrahlung and inverse-Compton.

Other gamma-ray instruments. There is a number of ground-based gamma-ray detectors which may be operative throughout CTA lifetime and albeit none of them would be a direct competitor there are obvious benefits from their complementary performances. One example among many is the High Altitude Water Cherenkov (HAWC) detector, with a 100% duty cycle and very wide field of view (~ 1 sr), observing the sky at TeV energies. Regardless of its modest ($\sim 0.5^\circ$) angular resolution and limited energy resolution, HAWC represents a competitive facility in sensitivity for very extended emission. By the time CTA will be active, it may provide a number of interesting steady sources for CTA to investigate. Mention must be given to the current generation IACTs (H.E.S.S., MAGIC and VERITAS) that are expected to continue operation into the CTA era. Synergies of interest are such as an extended monitoring for bright flaring sources and a number of other transient sources, in particular for cases when site's longitudes differ. Another project expected for the near future is ASTRI MINI-ARRAY

by an international collaboration between the Institute of Astronomy, Geophysics and Atmospheric Sciences of the University of Sao Paulo (IAG/USP), the Italian National Institute for Astrophysics (INAF) and the North-West University of South Africa. It will have 9 dual-mirror Cherenkov Telescopes the prototype of which was inaugurated in Serra la Nave, Catania, in September 2014. It will extend and improve the sensitivity (which is similar to H.E.S.S. in the 1-10 TeV energy range) to about 100 TeV.

Neutrinos and gravitational-waves. Despite the less precise identification (e.g through muon tracks reconstruction) of a source position, neutrino telescopes provide detection of the only completely unambiguous tracers of hadronic acceleration even out to high redshifts and beyond PeV energies. Individual neutrino sources with high enough flux might be very easily detectable with CTA and, with KM3Net and IceCube upgrades, this possibility is evermore hopeful. CTA is the ideal instrument to follow-up VHE neutrino clustering, necessary to localise and characterise the VHE accelerators. Even more, there is the topic of neutrino-generated alerts (ToOs or Targets of Opportunity) which would trigger a follow-up in order to localise and identify the source. Alongside neutrinos, the other flourishing messengers are gravitational-waves. Mergers of BHs, NSs and mixed systems are generators of gravitational-waves, events detectable by ground-based GW interferometers with the expectation of several to a hundred GW transients per year. However, until the advent of third-generation detectors the localisation errors will be relative large and asymmetric, especially if compared to CTA's field of view (localisation will greatly improved once more than three detectors and advanced observatories will be available). For follow-up CTA still retains many advantages though, with respect to most instruments and wavebands, including the large FoV, the flexibility to map very broad and non-circular error boxes (thanks to the large number of telescopes and the potentials of divergent pointing), the extremely quick response time (regardless of the extreme size of the array and telescopes) and a somewhat less ambiguous nature of counterpart identification (i.e. compared to the denser optical sky).

Chapter 3

Real-Time Analysis with the Cherenkov Telescope Array

In this chapter the real-time analysis structure and its role will be outlined, alongside the fundamental requirement influencing this work (i.e. short-timescales and sensitivity). The RTA role in the GW follow-up program will also be outlined (Section 3.1). In Section 3.2 the recent results on CTA differential and integral sensitivity will be presented, with focus on the short-timescale performances expected of CTA with respect to satellite science and existing IACTs. In Section 3.4 the analysis method used in this work (maximum likelihood analysis) will be described for unbinned analysis. In Section 3.5 the Wilk's theorem will be enunciated while Section 3.3 will be dedicated to Instrument Response Functions. The chapter will end with the description of the IRF degradation (Section 3.6 applied in order to test RTA performances at worsen sensitivity.

Technical issues, such as limited network bandwidth at the observatory sites and a huge expected data rate, prevent the observer from performing analysis off-site in real-time. Therefore, not without challenging requirements, an on-site analysis pipeline is mandatory to access raw data, compute the calibration and produce event lists. The on-site analysis (OSA), also referred to as Real-Time Analysis (RTA) or level A analysis, is in charge of data quality monitoring and automated science alert generation (SAG) with no more than 30 seconds of latency from the last acquired Cherenkov event contributing to the alert.

Delving into the RTA analysis architecture [34] [33] it must be said that parallel streams of the pipeline will be mandatory in case of simultaneous use of sub-array configurations. Moreover, the RTA availability during observation must be of about 95% at the very least. This system is conceived to allow real-time feedback to external alerts as well as serendipitous discoveries triggering internal alerts. Observations will thus require re-scheduling in order to follow-up the phenomena in real-time, as to maximise the facilities' network coordinated outcome. The RTA manages the camera data, both Cherenkov events and the technical data from auxiliary devices. It interfaces with: *i)* the data acquisition system (charged with the buffering of camera data and their streaming to the RTA); *ii)* the transient handler managing observation after receiving internal or external alerts; *iii)* the monitoring and control system, providing the performance and health monitoring of any CTA assembly.

The components of the RTA are the reconstruction system performing a fast reconstruction of the acquired events, the science alert monitoring which is charged with detection of unexpected astrophysi-

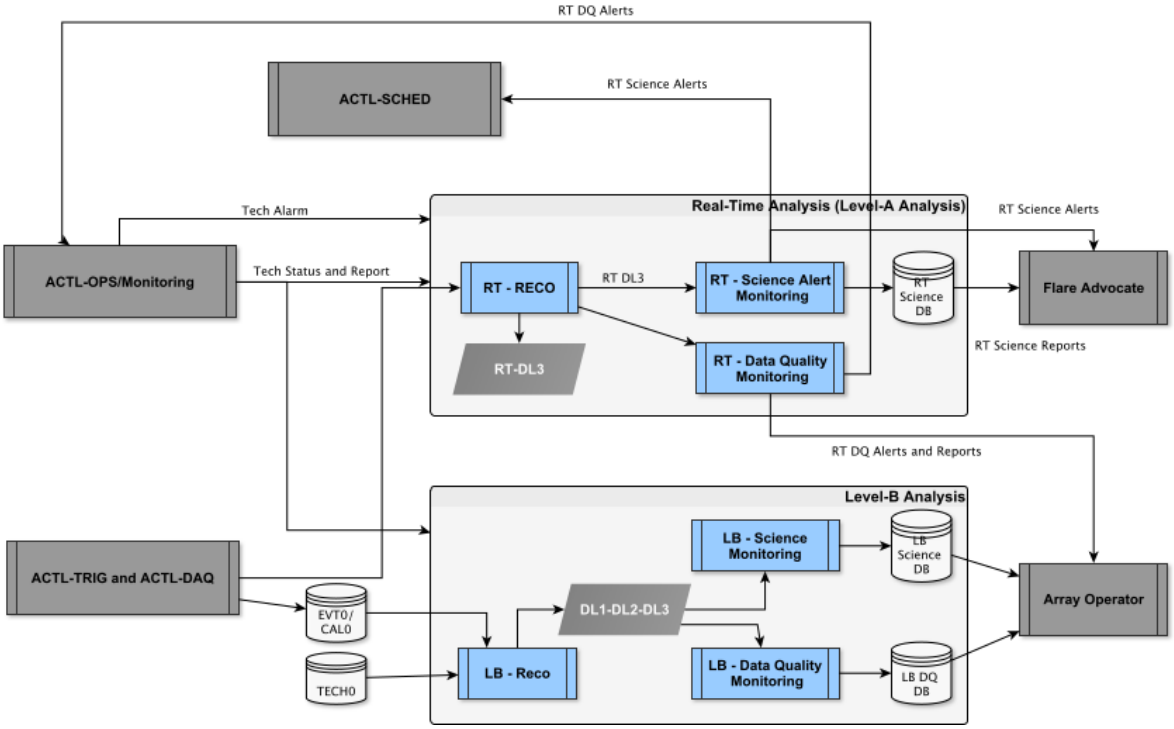

Figure 3.1: Real-Time Analysis architecture. **Credits:** Bulgarelli et al. 2015.

cal events and consequent alert generation, and the already mentioned data quality monitoring system which performs check and evaluates possible correction of observations in real time (i.e. pointing). This pipeline handles data quality alarms, sent whenever a given observation intake of data falls out of pre-defined quality criteria. Scientific products are to be stored in a dedicated database, alongside with the produced event lists and the summary of any RTA analysis containing the science reports. Since the RTA includes algorithms for science analysis, this work has required a tight collaboration and feedback exchange with the PHYS task group, specifically from the transient KSP and more particularly the GRB and GW working groups.

Proof of the feasibility of the CTA's data processing stream and of the fast inter-process communication architecture is the drive for the extensive prototyping and testing that are still ongoing nowadays. Another issue is represented by the data volume (expected from fraction of Gb/s to a few) which requires reduction from acquisition to higher level processing, scientific layered pipeline will hence run on heavily reduced data streams.

3.1 The key role of RTA in GW follow-up program

This work is focused on short GRB blind-search, hence a few more words will be spent to described the scenario of externally alerted GRBs and, in particular, for the RTA follow-up of GW transients. In Figure 3.2 the diagram of the RTA workflow in response to a GW alert is illustrated. After the observation scheduling has obtained the visibility windows and computed the most favourable sky coordinates for the observation with respect to the energy range, the alert uncertainty coverage and the observing time, an RTA pipeline must analyse each observation in real-time. RTA should be able to detect sub-minute emission, trigger deeper observation on the region in order to assess the detection of a candidate electromagnetic (EM) counterpart and issue scientific alerts to external observatories with low latency (less than 30 seconds from the last acquired event contributing to the alert).

In [102] the GW alert reception time was set to $\sim$ 3 minutes. In this work a latency of the order of few seconds (similar to satellite alerts) will be assumed for simplicity (Section 4.6.3 and 5.2.2),

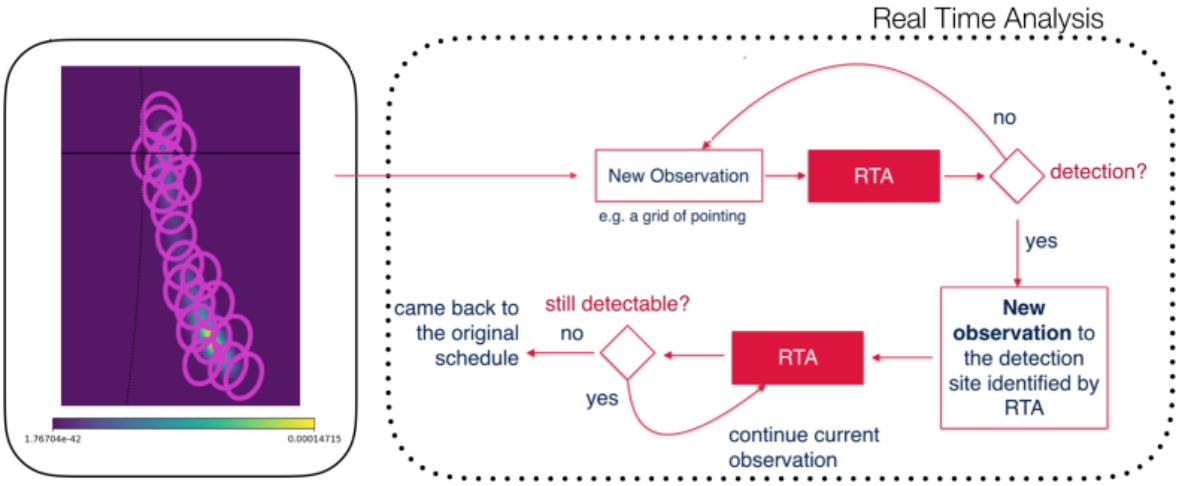

Figure 3.2: Real-Time Analysis diagram for the GW transients follow-up program. **Credits:** Seglar-Arroyo et al. 2019 and A. Bulgarelli (right).

although in Section 6.5 considerations on the alert latency assumptions will be offered, with respect to RTA detection performances since this work does not aim at designing an optimised follow-up strategy. From Figure 3.2 one can gather that as soon as the alert is received, an optimal observation is scheduled. RTA must analyse data simultaneously to the observation and determine if (and at which significance) a detection is found within the FoV. If no source is localised (eventually excluding known targets from the search), the array must be moved to the next pointing. The tiling procedure stops as soon as positive detection is achieved, at which point the observation stabilises and the tracking of the target starts. RTA shall continue to analyse data in real-time as long as the target remains detectable (the proposed strategy actually requires to follow-up for two additional hours from the last positive detection). The duration of each observation window should be dynamically determined as:

$$\int_{t_0}^{t_0+t_{obs}} \frac{dF(t)}{dt} dt = F_{5\sigma}^{int}(t_0, t_0 + t_{obs}) \tag{3.1}$$

where t_0 represent the observation start time, t_{obs} the time window for the observation and $F_{5\sigma}^{int}$ the minimum integral flux required to achieve a 5σ detection of the target. The observing time t_{obs} increases as $t - t_{merger}$ becomes larger to account for the temporal decay of the lightcurve. A 5σ detection will no longer be possible when $t_{obs} \longrightarrow \infty$. In this work, dynamic determination of temporal windows has not been implemented for two reasons: *i)* the study aims at investigating the shortest exposure time at worsen sensitivity conditions, in order to outline preliminary perspective of the SAG and to constrain the capability of short-timed analysis; *ii)* dynamic time window determination requires model assumptions on the temporal decay of the source, a study which the GRB and GW experts in CTAC are carrying out [64] [102] [3].

3.2 Short-timescale sensitivity

According to CTA design requirements, if a transient source is detected in the scanned time-scale, the low-latency science alert must have sensitivity not worst than a factor of two [35] with respect to the nominal CTA sensitivity. The sensitivity of an instrument is the minimum detectable in a fixed observation time, which for this work is computed from a steady test source in a given energy range. It depends on the effective area, angular resolution and rate of background events [132]. The integral sensitivity is the least detectable flux (of a steady source) with at least 5σ significance detection for $E > E_0$, where E_0 is each considered energy threshold. CTA integral sensitivity depends on *i)* the array configuration and telescope designs (i.e. effective, area, angular resolution, etc.); *ii)* the reconstruction algorithm (i.e. background rejection efficiency); *iii)* the source spectral properties (i.e. energy range, flux, variability, spectral shape) [36]. The sensitivity computation outcome, though, highly depends on the knowledge claimed over the background modelling at low energies and the ability to collect

enough photons at high energies. At low energies the night sky and cosmic-ray induced background are extremely high, causing systematics in the background subtraction and limiting the sensitivity for long exposures. The background statistics are the limiting factor around 1 TeV while for higher energies the occurrence of VHE photons naturally decreases, leaving detection to be dependant on the total effective area [36].

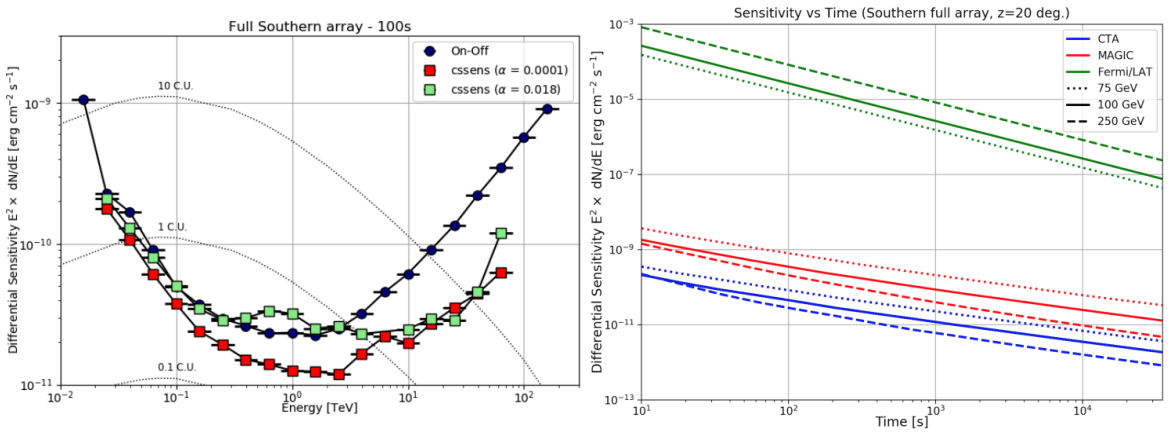

(a) (b)

Figure 3.3: **Left** CTA differential sensitivity curves for t_{exp} =100 s, obtained with standard aperture photometry and full-FoV maximum likelihood analysis. **Right** CTA South differential sensitivity (purple lines) as a function of the exposure time. The curve is compared to one of Fermi-LAT (red lines), MAGIC (orange lines) and VERITAS (light blue lines) at four selected energies (75, 100, 150 and 250 GeV). **Credits:** Fioretti et al. 2019.

CTA standard rules for integral (differential) sensitivity evaluation consider a number of energy thresholds (bins), i.e. five per decade equally space logarithmic thresholds (bins), in which the flux of a source is detected with a given minimum significance (i.e. TS$\approx \sigma^2$=25). The estimate is performed by means of a linear fit seeking the approximate flux normalisation that converges to the threshold significance of source detection. In [37] CTA differential sensitivity computed with a full field of view maximum likelihood method is compared to the standard on-off analysis used in aperture photometry [29]. The maximum likelihood analysis was found to predict up to $\sim$ 6 times better sensitivity for 100 s exposure time. In [37] was shown that the more optimistic result is due to a finer knowledge claimed over the background and the lack of a minimum source count requirement. If both methods are implemented under the same assumptions, they are shown to converge (Figure 3.3(a)). From this study, the comparison between CTA and MAGIC or Fermi-LAT sensitivity performances as a function of time was also carried out. In Figure 3.3(b) the sensitivity versus the exposure time of CTA, Fermi-LAT and MAGIC is shown for three energy ranges (75, 100, 250 GeV). At $t_{exp} < 100$ seconds CTA is 10 times more sensitive than MAGIC and up to 10^4 times more sensitive than Fermi-LAT.

3.3 Instrument Response Functions

Instrument Response Functions are mathematical description of the reconstructed photon arrival direction ($\vec{p}'$), energy (E') and time (t') with respect to the true quantities ($\vec{p}$, E and t respectively). Given a gamma-ray intensity of $I(\vec{p}, E, t)$, the expected event rate as a function of the reconstructed parameters is:

$$e(\vec{p}', E', t') = \int R(\vec{p}', E', t'|\vec{p}, E, t) d\vec{p} dE dt \times I(\vec{p}, E, t) \tag{3.2}$$

where $R(\vec{p}', E', t'|\vec{p}, E, t)$ describes the response of the instrument to an observation by linking the reconstructed quantities to their true value. For CTA (and IACTs in general), Instrument Response Functions (Equation 3.3) are factorised in: *i)* effective area ($A_{eff}(\vec{p}, E, t)$ in units of cm^2; *ii)* point-spread function ($PSF(\vec{p}'|p, E, t)$); *iii)* energy dispersion ($E_{disp}(E'|\vec{p}, E, t)$).

$$R(\vec{p}', E', t'|\vec{p}, E, t) = A_{eff}(\vec{p}, E, t) \times PSF(\vec{p}'|\vec{p}, E, t) \times E_{disp}(E'|\vec{p}, E, t) \tag{3.3}$$

where

$$\int PSF(\vec{p}'|\vec{p}, E, t) d\vec{p}' = 1 \tag{3.4}$$

and

$$\int E_{disp}(E'|\vec{p}, E, t) = 1 \tag{3.5}$$

In addition the IRFs[1] contain the description of the background rates as a function of energy and position within the field of view. The background rate is mostly composed by cosmic-ray hadrons and electrons that survive the gamma-ray selection criteria (cuts) [132].

3.4 Full-FoV maximum likelihood

This work has been carried out parallel to a twin master thesis project by Simone Tampieri [115], which the reader can refer to for the use of aperture photometry in the context of real-time analysis with CTA. This work implements a full field of view maximum likelihood instead, descendant from on-space data analysis technique. The aim is to investigate the feasibility and performances of this technique, and develop a pipeline for RTA with the available scientific tools (Section 5.1).

Three fundamental parameters characterise an observation: *i)* the reconstructed instrument direction, $\vec{p}'$; *ii)* the measured energy, E'; *iii)* the trigger time, t'. The maximum likelihood function $L_i(M)$ describes the probability of the collected data during a given observation to be drawn from a particular model M. For unbinned event lists (i.e. this work) the Poisson formulae is used for maximum likelihood estimation (MLE):

$$-\ln L_i(M) = e_i(M) - \sum_k \ln P_i(\vec{p}_k', E_k', t_k'|M) \tag{3.6}$$

where the sum is over all events k, P_i is the probability density conditioned to a given model M and e_i represent the total number of predicted events expected to occur during an observation given the model M. The latter is computed by:

$$e_i(M) = \int_{GTI} \int_E \int_{ROI} P_i(\vec{p}', E', t'|M) d\vec{p}' dE' dt' \tag{3.7}$$

in which GTI stands for Good Time Intervals, defining the contiguous temporal bounds for data intake, and ROI is the region of interest. For an arbitrary number of observations, the joint maximum likelihood is computed from:

$$-\ln L(M) = -\sum_i \ln Li(M) \tag{3.8}$$

This opens the possibility for multi-instrument and multi-wavelength event data analysis. It supports parallelisation in order to speed up computations. Description of an astrophysical source is parametrised by its spatial, spectral and temporal components (more in Section 5.1) while the background modelling is generally computed from a specific instrument description of events. The event probability density is obtained by convolving the model with the Instrument Response Function (Section 3.3):

$$P_i(\vec{p}', E', t'|M_j) = \int_{\vec{p},E,t} R_i(\vec{p}', E', t'|\vec{p}, E, t) \times M_j^S(\vec{p}, E, t) d\vec{p} dE dt \tag{3.9}$$

[1] Publicly available IRFs: `https://www.cta-observatory.org/science/cta-performance/`

where the primed quantities correspond to measured/reconstructed ones whilst non-primed quantities are true ones. The subscript j indicates a specific source model M_j. The factorisation of a source model is given by:

$$M^S(\vec{p}, E, t) = M_s(\vec{p}|E, t) \times M_E(E|t) \times M_t(t) \tag{3.10}$$

where M_s, M_E and M_t stand for the spatial, spectral and temporal[2] components of the model (the indices j have been dropped for conciseness). The maximum likelihood fit adjusts a subset of parameters (free parameters) in order to find the values that represent best the measured data. In doing so, convolution with the Instrument Response Function is applied.

The detection significance of the source model is described by a Test Statistic (TS) value:

$$TS = 2(\ln L(M_s + M_b) - \ln L(M_b)) \tag{3.11}$$

where $\ln(L(M_s + M_b)$ is the log-likelihood value obtain from source + background fitting with data. Under the hypothesis that a source + background model provides a satisfactory description of data, TS follows a χ^2_n distribution with n degrees of freedom. Therefore,

$$p = \int_{TS}^{+\infty} \chi^2_n(x)dx \tag{3.12}$$

is the chance probability that the log-likelihood improves by $TS/2$ when adding a source model M_s, due to statistical fluctuations only. For $n = 1$ the Test Statistic value relates to a Gaussian significance as $\sigma = \sqrt{TS}$ (more in Section 3.5 and Section 6.1).

3.5 Wilks' theorem

From [4]: *Assuming a population K in which a variate x has distribution $f(x, \theta_1, \theta_2, ..., \theta_h)$ dependant of $\theta_1, \theta_2, ..., \theta_h$ parameters, a simple hypothesis is one where θ_i have specified values. A set Ω of admissible hypotheses is considered one which is consistent with a set of simple hypotheses. Geometrically, Ω may be represented as a region in the h-dimensional space of the θ_i. A set ω of simple hypotheses is specified by taking all simple hypotheses of the set Ω for which $\theta_i = \theta_{0,i}$, where $i = m + 1, m + 2, ..., h$.*

Consider a random sample O_n of n individuals drawn from K, geometrically represented as a point in an n-dimensional space of the x_i. The probability density function associated with O_n is

$$P = \prod_{\alpha=1}^{n} f(x_\alpha, \theta_1, \theta_2, ..., \theta_h) \tag{3.13}$$

Let $P_\Omega(O_n)$ be the least upper bound of P for the simple hypotheses in Ω and $P_\omega(O_n)$ the least upper bound of P for those in ω. Then

$$\lambda = \frac{P_\omega(O_n)}{P_\Omega(O_n)} \tag{3.14}$$

is defined as the likelihood ratio for testing the composite hypothesis H that O_n comes from a population with a distribution characterised by values of the θ_i for some simple hypothesis in the set ω. When H is true, then O_n is from some population of the described set. Consider the existence of optimum estimates of θ_i, namely consider the existence of functions $\widetilde{\theta}_i(x_1, ...x_n)$ such that their distribution is

$$\frac{||c_{ij}||^{1/2}}{(2\pi)^{h/2}} e^{-1/2 \sum_{i,j=1}^{h} c_{ij} z_i z_i} (1 + \phi) dz_1, ..., dz_h \tag{3.15}$$

where $z_i = (\widetilde{\theta}_i - \theta_i)\sqrt{n}$, $c_{ij} = -E\left(\frac{\delta^2 \log f}{\delta\theta_i \delta\theta_j}\right)$ with E being the mathematical expectation, ϕ is the order of $1/\sqrt{n}$ and $||c_{ij}||$ is positive definite. Given the above, Wilk's theorem [4] enunciates that

[2] `http://cta.irap.omp.eu/ctools/users/user_manual/models_temporal.html`

Theorem. If a population with a variate x is distributed according to the probability function $f(x, \theta_1, \theta_2, ..., \theta_h)$, such that optimum estimates $\widetilde{\theta_i}$ of the θ_i exist and are described by Equation 3.15, then when the hypothesis H is true that $\theta_i = \theta_{0,i}$, $i = m+1, m+2, ..., h$, the distribution of $-2\log\lambda$ where λ is given by Equation 3.14 is, except for terms of the order $1/\sqrt{n}$, distributed like a χ^2 with $h - m$ degrees of freedom.

3.6 Sensitivity degradation

CTA performance (Section 3.3) values derive from Monte Carlo (MC) simulations based on the `CORSIKA`[3] air-shower simulation program and telescope simulation tool `sim_telarray`[27]. The `production3b (prod3b)` in use for this work, is updated with the most recent (at the time of writing) detector model of the CTA telescopes. The performance curves are obtained from two different types of gamma-ray simulations, on-axis and diffuse. The on-axis component locates the source at the centre of the FoV of each camera, while the diffuse component entails an arrival direction of the primary gamma-rays selected from a cone (20° of diameter) around the pointing direction. A parallel pointing technique is assumed. Simulations have been generated for a range or zenith angles (`prod3b-v1`, `prod3b-v2`), exposure times (`prod3b-v1`, `prod3b-v2`) and night-sky background (NSB) (`prod3b-v1`) for the southern and northern sites.

In order to represent the degraded sensitivity expected from RTA, to constrain detection rates and localisation precision, and to perform a realistic study for the pipeline feasibility in the RTA context, it was decided to deteriorate the IRF via manipulation of the effective area. Given an area A_{geo} perpendicular to the pointing axis and sufficiently large so that any gamma-ray whose trajectory does not cross A_{geo} has negligible probability of being detected, then $A_{eff} = \epsilon \times A_{geo}$ with ϵ being the overall detection efficiency for events with trajectory crossing A_{geo}. The IRF degradation performed aimed to obtain a not worse than a factor of two sensitivity at short exposure times. Whilst the effective area is a function of the position within the field of view and the energy, in this work we assume the simplest case of half effective area, at all positions and energies, with respect to the nominal IRFs. In order to take the effective area degradation into account in the background modelling, background rates were consequently re-normalised:

$$B_{degr} = \frac{B_{nom}}{A_{eff,nom}} \times A_{eff,degr} \tag{3.16}$$

Sensitivity computation was done by means of the `cssens` tool from `ctools` software package (Section 5.1 and 5.3.1). The tools utilises maximum likelihood fitting of a test source, compiling over a number of energy bins (differential sensitivity) or energy threshold (integral sensitivity) within a given energy range. Of relevance for this study is the integral sensitivity, since the analysis is performed unbinned (Section 3.4). The source spectrum assumed equals that in Section 5.1 (Crab model). The test source is fitted to simulated data and detection significance is retrieved as a function of the source flux. This is then varied to reach a given value, i.e. 5σ. In Figure 3.4(a) and Figure 3.4(c) the nominal and degraded effective areas, respectively, as a function of the energy and the off-axis angle are shown. Figure 3.4(b) and Figure 3.4(d) are the corresponding expected background rate for VHE (150 TeV threshold) for nominal and degraded IRFs, respectively. These values are taken from the latest CTA Performance IRFs for the South full-array configuration at averagely 40° of zenith angle and 30 minute of exposure. Nominal values are in blue, while degraded values are in red (see Chapter 5 for more details on the implementation for degrading the IRFs). Notice that, by degrading the sensitivity via the effective area, the background rate decreases. Therefore, a more realistic approach would require to degrade also the rejected background events by increasing their rates as a function of the energy and the off-axis angle. Since a precise characterisation of the IRFs degradation is not within the scope of this work, only effective area related degradation will be considered from hereon.

[3] https://www.ikp.kit.edu/corsika/

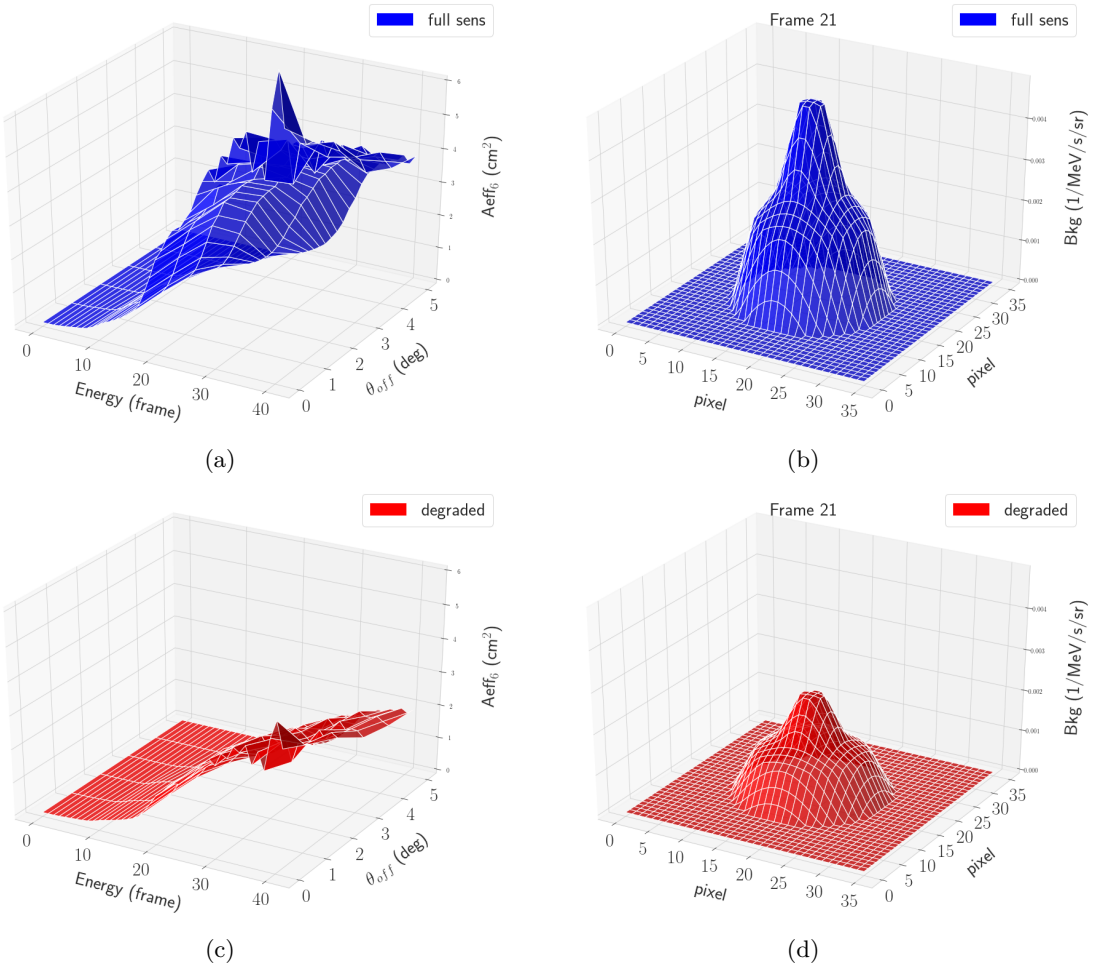

Figure 3.4: The top panels represent the effective area (a) and the background rate (b) of a nominal IRF. The effective area is given as a function of energy and off-axis angle, while the background rates are shown as a function of the off-axis at a given energy bin (i.e. from $\sim$ 125 TeV up to $\sim$ 200 TeV for the shown plots). The bottom panels show the same plots for degraded IRFs (effective area (c) and background rates (d)).

The differential flux sensitivity (νF_ν or $E^2 dN/dE$) is calculated with a required confidence of 5σ. In Table 3.1 the integral sensitivity values of an on-axis source at short exposure times (t_{exp} =1, 5, 10, 100 s) are reported in terms of the minimum detectable photon flux (ph/cm^2/s), and the as the test source spectrum (Crab) evaluated at the mean logarithmic energy multiplied by the energy squared (erg/cm^2/s) for the energy range from 30 GeV to 150 TeV (see Section 5.1 and 5.3.1 for more details, as well as [7] and [6]). In Figure 3.5(b) the curves of the integral sensitivity for nominal and degraded IRFs (`South_z40_0.5h` from `prod3b-v2`) are also shown. The plot represents the least detectable photon flux for a given energy threshold (top panel) for nominal and degraded IRF and the ratio between the two (bottom panel). Since better sensitivity corresponds to lower values of least detectable photon flux, the ratio never being lower than 0.5 is in agreement with RTA sensitivity requirements. In Appendix A one can find the plots for all considered exposure times. In Figure 3.5(a) the ratio between nominal and degraded integral sensitivity (0.03-150 TeV) as a function of the exposure time (t_{exp} =1, 5, 10, 100 s) is shown.

IRF	$t_{exp} = 1$ s	$t_{exp} = 5$ s	$t_{exp} = 10$ s	$t_{exp} = 100$ s
on-axis F (ph/cm^2/s) in 0.03-150 TeV				
nominal	3.7e-09	1.4e-09	8.6e-10	1.8e-10
degraded	6.9e-09	2.3e-09	1.4e-09	3.0e-10
on-axis E^{2}F (erg/cm^2/s) in 0.03-150 TeV				
nominal	3.4e-11	1.3e-11	7.9e-12	1.7e-12
degraded	6.3e-11	2.1e-11	1.3e-11	2.8e-12

Table 3.1: The table summarises the integral sensitivity within 0.03-150 TeV for an observation with CTA South full-array of an astrophysical object with the same properties as the Crab. The IRFs in use are the nominal and degraded version of `South_z40_0.5h` from `prod3b-v2`. The minimum detectable flux is given as photon flux (ph/cm^2/s) while sensitivity is evaluated at the mean logarithmic energy multiplied by the energy squared (erg/cm^2/s).

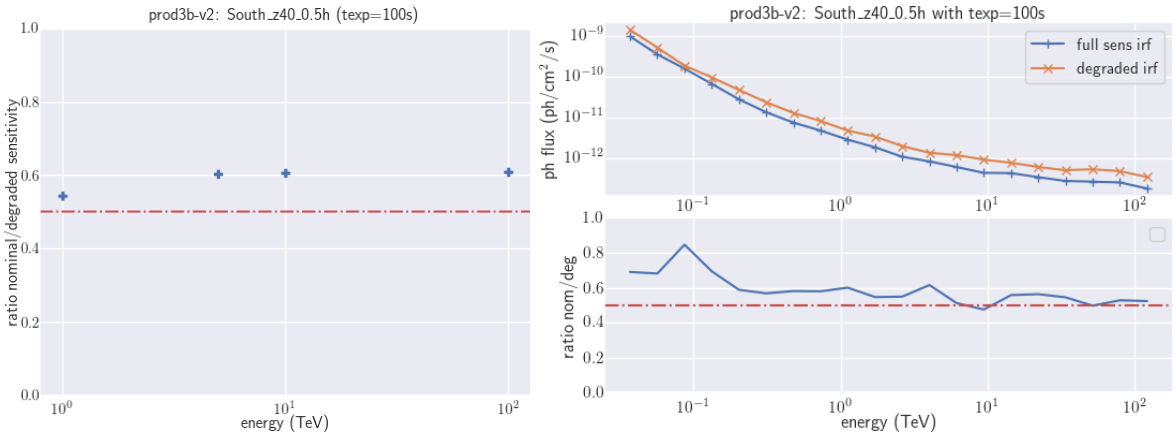

(a) (b)

Figure 3.5: The left panel shows the ratio between the nominal and degraded integral sensitivity (0.03-150 TeV) for a given exposure time. On the right the $t_{exp} = 100$ s integral sensitivity curve for given energy thresholds is shown. The RTA requirements are that the sensitivity must not be worst than the nominal by more than a factor of two.

Chapter 4

Focus on Gamma Ray Bursts

Wherein the transient KSP proposed by CTAC is further investigated (Section 4.1) with specific focus on GRBs. An introduction on the phenomena can be found in Section 4.2, with a brief description of the most widely accepted theoretical model (the fireball model) in Section 4.2.1. An overview of the emission mechanisms is presented in Section 4.2.2; in Section 4.2.3 the BNS progenitors of short GRB will be briefly described, with focus on the gravitational radiation produced by the system. The observing strategy proposed by the CTAC for GRBs is exposed in Section 4.3 and Section 4.4 summarises the science return to be expected of the program. In Section 4.6.1 the on-going work of the POSyTIVE project (POpulation Synthesis Theory Integrated model for Very-high Emission) is presented, followed by a state-of-the-art recap of recent VHE gamma-ray bursts detection by IACTs (Section 4.5). The extra-galactic background light absorption is introduced in Section 4.6.2 alongside few implementation details with respect to this work. The chapter concludes with the science case description (Section 4.6), introducing the template of the source in Section 4.6.3.

4.1 The transient KSP

The increasingly sought complementarity of MM/MWL astronomy has greatly improved the search for transients, and CTA will held a key role for alerts follow-up as well as serendipitous discoveries. The transient KSP expects to invest a great amount of observation time per year as well as consistency of observation throughout CTA lifespan. The anticipated amount totals to 390 h/yr/site for the two-year early phase, 125 h/yr/site for the first two years of full-array operation and 95 h/yr/site from the third year onward. Each target class (Section 2.3) has been given an appropriate scheduled plan (see Table 4.1). Data products will consist in spectra and light-curves for each positive detection, plus upper-limits for the fraction of alerts observable by CTA. Rights for data ownership should follow the proposed protocol of one-year proprietary, although in order to guarantee MM/MWL follow-up selected information should be rapidly communicated (i.e. Gamma-ray burst Coordinate Network, Astronomer's Telegrams, IAU circulars etc.). The CTA Consortium has estimated detection rates through extensive and detailed simulations, allowing measurements on performances' expectancy [1]. The source classes targeted by this KSP are briefly introduced in the following:

▷ *Gamma-Ray Bursts.* Based on external alerts albeit without excluding the chance of serendipitous discoveries, GRBs are going to be a major component for this KSP targets' list [47]. Thought to be triggered by particular and rare types of stellar collapse and mergers involving neutron stars [2] and/or black holes [66] these sources are among the most luminous and distant objects of the universe. They are, also, one of the most mysterious ones, with many basic aspects yet to be understood. Other than investigating GRB physics, CTA will use these targets as probes for cosmic-rays physics [134] [72], observational cosmology [66] and fundamental physics [55].

▷ *Galactic transients.* A broad range of compact galactic objects [65] exhibits various types of jets and winds that accelerate high-energy particles in sporadic outbursts. The production of such mechanism can be greatly clarified through CTA observations, including targets like: PWNe [67] with their relativistic outflows due to rotating NSs, flares from NSs with anomalously high magnetic fields known as magnetars, jet ejection from micro-quasars and other X-ray binaries [68] comprised of NSs and/or BHs accreting matter from a stellar companion, novae caused by the explosions on the surfaces of a white dwarf, and so on. The alerts are expected to be issued from monitoring facilities.

▷ *X-ray, optical and radio transients.* A large number of X-ray, optical and radio "transient factories" facility, both current and upcoming, are expected to generate large quantities of alerts from their regular monitoring of large areas of the sky [70]. Events such as tidal disruption, supernova shock breakout (SSB) and fast radio busts (FRBs) [69] will be studied on a wide range of wavelengths and CTA will be able to account for the VHE counterparts, when present, for a selected sample.

▷ *High-energy neutrino transients.* The follow-up of such sources is issued by neutrino observatories. Cosmic HE neutrinos are indicative of hadronic cosmic-ray production and whilst detected by the current facilities, their origin is yet unclear [71] [72]. This KSP can possibly give insights on their origin, and on extra-galactic and/or galactic cosmic-rays as well, by following-up appropriately selected alerts.

▷ *GW transients.* This program is based on GW observatories alerts [64], as gravitational waves have been detected for the first time in recent years [73]. More detections are expected in the near future and in order to best search for their electromagnetic counterparts [74], a large portion of CTA transient programs is dedicated for the follow-up of events such as these. Transients of this type are expected from, i.e., binary mergers of compact objects [75]. Suitable strategies are undergoing simulations and studies, due to the still large uncertainties for GW sources localisation.

▷ *Serendipitous VHE transients.* Issued by CTA itself via a Real-Time Analysis (RTA) pipeline running parallel to any scheduled observation. The RTA can recognise new transients or flaring states of known sources at very-high energies, anywhere in the field of view. Its role is to automatically issue alerts within 30 s [33] [35] (Section 3).

		Observation times (h/yr/site)		
Priority	Target class	Early phase	Years 1-2	Years 3-10
1	GW transients	20	5	5
2	HE neutrino transients	20	5	5
3	Serendipitous VHE transients	100	25	25
4	GRB	50	50	10
5	X-ray/optical/radio transients	50	10	10
6	Galactic transients	150	30	0(?)
	Total per site (h/yr/site)	390	125	95
	Total both sites (h/yr)	780	250	190
	Total in different CTA phases (h)	1560	500	1520

Table 4.1: Maximum observation times required for follow-up targets in the Transient KSP, taken from [1].

CTA Consortium defined a list of Top Level Use Cases for scientists to develop [101], among which is the observation of a GRB after an external alert. The developments can be traced through the Proceedings of Science published by transients, GRB and GW working group of CTAC and are expected to be published in Consortium Papers during the following months [64] [102] [53]. The following section will serve as introduction to the phenomena of Gamma-Ray Bursts, briefly presenting the history of their discovery and the model describing the their physical nature. A short paragraph will be dedicated in particular to short GRB and their progenitors, seeing how the GW follow-up of a short GRB is the science case in use for this work.

4.2 Gamma-Ray Bursts

Gamma-ray bursts are abrupt explosion of gamma-rays, isotropically distributed and of cosmological origin. They were discovered accidentally by the Vela satellites in the late sixties, during a monitoring mission of the "Outer Space Treaty"[1]. The discovery of GRBs was first announced to the scientific community in 1973 [113] and soon after corroborated by further studies [116] [117]. Several dedicated satellites and ground-base missions have been deployed since then. Worthy of notice is the BATSE detector on the COMPTON-GRO (Gamma-Ray Observatory) launched in 1991. Its observation of the isotropy of GRBs was key in understanding the extra-galactic origin of these phenomena [118]. In Figure 4.1 is the sky distribution of GRBs observed by BATSE, with colour gradient (from blue to red) describing the fluence of the event. Considering E the energy of a gamma-ray burst located at distance r from the observer, the fluence can be defined as:

$$S = \frac{E}{4\pi r^2} \tag{4.1}$$

assuming an isotropic burst. From Figure 4.1 is clear that bursts are distributed isotropically.

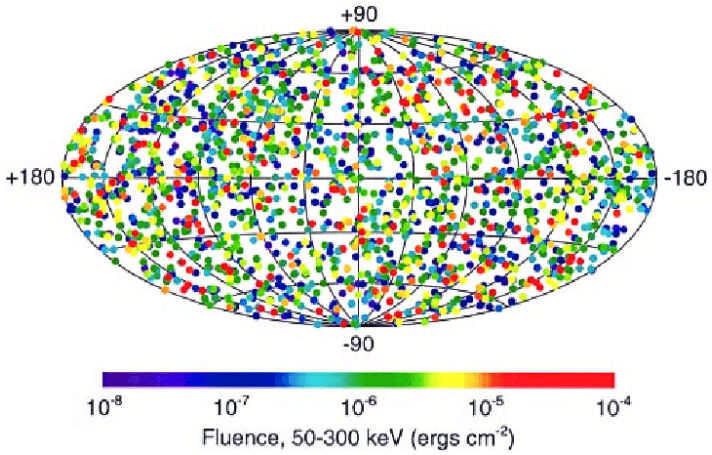

Figure 4.1: Distribution on the sky of 1,825 GRBs observed by BATSE. The map shows burst locations (without indicating position uncertainties) in galactic coordinates. There are no preferred directions, either of galactic or extragalactic significance. Colour code indicates the total burst energy. Bursts are distributed isotropically, independent of their brightness, duration, spectrum, or any other characteristic. **Credit:** D. Hertmann, 1999.

The discovery of X-ray transient counterparts to several GRBs by BeppoSAX [119] confirmed their cosmological origin via redshift measurements, soon followed by the observation of optical [120] and radio [121] counterparts as well. Their extra-galactic nature implies that GRBs must be extremely luminous sources. In fact, they are the most electromagnetically luminous objects in the universe at high energies, releasing $\gtrsim 10^{51} - 10^{53}$ ergs in a few seconds. Considering the average amount of observation by BATSE (one burst per day) and assuming that the rate of GRBs does not change with cosmological time, only one burst per million years per galaxy occurs [112]. The rate

[1] A treaty that forms the basis of international space law and forbids nuclear explosion in space, signed on 27 January 1967 and entered into force on 10 October 1967. Depository governments: United States, United Kingdom and Soviet Union.

is of course higher (and the energy is lower) when accounting for the beaming of the gamma-ray emission.

From observations, gamma-ray bursts appear as two-phased emitters, described by a *prompt emission* in the keV-MeV energy band and an *afterglow emission* from radio to gamma-rays. The former can last between $0.01 - 1000\,s$ and is characterised by rapid and irregular variability. The latter decays gradually over hours to weeks (or more). GRBs are typically classified based on the prompt duration[2] in short and long gamma-ray bursts. Phenomena with $T_{90} \lesssim 2\,s$ are known as *short-hard gamma-ray bursts* whilst phenomena with $T_{90} \gtrsim 2\,s$ are called *long-soft gamma-ray bursts* [88]. Short GRBs inner engines are thought to be mergers of compact object binaries (i.e. NS-NS, NS-BH), while long GRBs originate from massive stellar core-collapse events (the magnitude necessary for NSs/BHs creation). An extensive compendium of GRB theoretical and observational reviews can be found in [89]. The following paragraph will delve briefly into the theoretical model used to described these phenomena.

4.2.1 The fireball model

The most widely accepted model of a GRB, predicting all observed counterparts and the aforementioned two-phased radiation, is the relativistic fireball model. It explains the emitted gamma-rays as ultra-relativistic energy flows converted to radiation (i.e. kinetic energy of ultra-relativistic particles) and requires an accreting compact object (i.e. collapsar, binary of neutron stars, left hand-side of Figure 4.2) that produces a long energy flow in comparison to the size of the source. The inner engine is hidden from direct observation but the temporal structure of the radiation reflects the internal activity. Internal shocks (yellow coloured shocks in Figure 4.2) convert the energy of the relativistic shell to radiation during the prompt phase. At the impact of the outflow with the external medium, i.e. inter-stellar medium (ISM), the afterglow emission onsets due to energy dissipation via external shocks (orange coloured shocks in Figure 4.2).

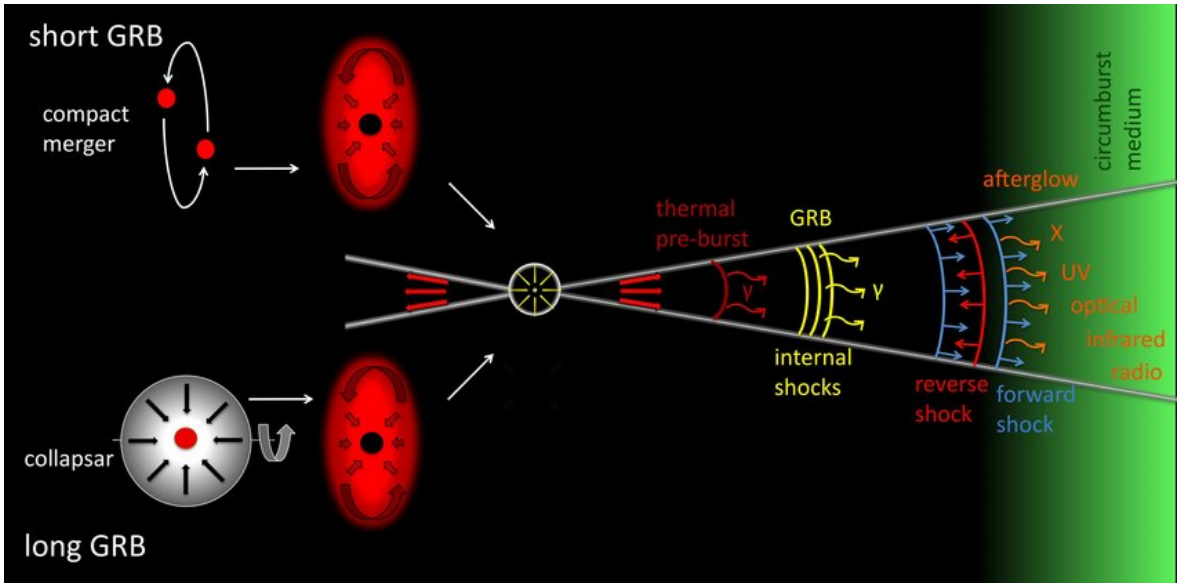

Figure 4.2: Progenitor models for short and long GRBs (left), and production sites of prompt and afterglow emission in the fireball model (right). **Credit:** A. Gomboc, 2012.

[2]The prompt duration is measured by T_{90}, a quantity that indicates the time necessary to accumulate from 5% to 95% of the counts. Alternatively T_{50} can be used, corresponding to the time required to accumulate from 25% to 75% of the counts in aforementioned energy band. While investigating extremely long gamma-ray bursts, the so called ultra-long gamma-ray bursts (ulGRBs), an alternative definition of GRB classes was proposed in Boer et al. (2015) because of the ambiguity in duration measures, due to T_{90} strong dependence on the energy band of the observation, the instrument duty cycle, etc. In this work an empirical parameter T_X was defined as *"the epoch at which the steep decay phase, monitored in X-rays (0.3-10 keV) just after the burst trigger, starts"*. This parameter can be considered as a proxy of the X-ray counterpart of the GRB burst duration typically estimated in gamma-rays [111].

A fireball is a large concentration of energy (radiation) in a small region of space that contains relatively few baryons [112]. This model was proposed by Goodman [122] (explosion mechanism) and by Paczynski [123] (steady wind mechanism from a continuous source). They demonstrated how a sudden release of large quantity of gamma-ray photons can lead to an opaque photon-lepton fireball via pair production. In this context, the term fireball refers to an opaque pure radiation-plasma (no baryons) whose initial energy is significantly larger than its rest mass. The effect of a baryonic load was considered only later in the model. In [124] [125] it was showed that under most circumstances the ultimate outcome of a fireball with a baryonic load will be the transfer of all the energy of the fireball into the kinetic energy of the baryons. If the baryonic load is sufficiently small the baryons will be accelerated to a relativistic velocity with $\gamma \approx E/M$, where

$$\gamma = \frac{1}{\sqrt{1 - \frac{v^2}{c^2}}} \tag{4.2}$$

is the Lorentz factor, E and M are the energy and mass of the fireball. If $\gamma \gg 1$ then the net result will be a Newtonian flow with $v \cong (2E/M)^{1/2}$. A seemingly contradiction arises from GRB data. Their spectrum is of the non-thermal form (power law spectrum photons) yet the short variations in their lightcurves imply a very compact object, hence optically thick sources. This apparent contradiction can be circumvented if relativistic motion is accounted for. The apparent variation in time would be shorter by γ^2 as compared with the intrinsic variability time-scale. As consequence, the apparent energies are larger than the corresponding energies in the progenitor's rest frame by a factor of γ.

4.2.2 The HE radiation mechanisms

Temporal properties of the HE prompt emission (yellow coloured GRB internal shocks from Figure 4.2) point toward an internal engine [17]. Theoretical and observational analyses suggest that during this early phase the afterglow emission plays only a sub-dominant role [90], becoming relevant only at the end of the prompt (except for the sometime presented low-energy excess [95]). Supporting this claim are a number of light-curves showing a steep-to-shallow decay in the GeV domain, interpreted as the transition between prompt and afterglow [91]. In [92] some proposed models present a delayed onset of the HE prompt component (yellow coloured emission from Figure 4.2) compared to the keV radiation, explained by different condition at the emitting region. The HE component may then arise from SSC or $\gamma - \gamma$ annihilation [93] [94]. The afterglow radiation (orange coloured emission from Figure 4.2) is thought to have an external origin, likely produced between the fireball and the external medium via, i.e., synchrotron radiation[103] [104] due to electrons accelerated at the external shocks, with possible contribution from SSC [105] [106]. Recent detections [40] [41] [108] will undoubtedly help in shading more light on the spectral properties of the VHE component, as well better constraining the predicted detection rates (Section 4.3).

4.2.3 Focus on short GRB progenitors as GW transients

Short GRB are the protagonists of this study for the role played in MM and MWL astronomy. The best progenitor candidates for short GRB are binary neutron star mergers or neutron star/black hole mergers, connection that has been strengthen in the last 10 years [144], due to the binary orbits decay caused by gravitational radiation emission [129]. The process can release approximately up to $5 \cdot 10^{53}$ erg, though most of it escapes as neutrinos and gravitational radiation (which can be detected through neutrino detectors and GW interferometers, respectively). Gravitational waves are predictions of Einstein's general theory of relativity, confirmed by a 30-year study of PSR1913+16 (the Hulse-Taylor pulsar)[3]. General relativity requires that for an accelerated, non spherically symmetric, mass distribution the resulting changes in the surrounding space-time curvature may propagate outward as a gravitational wave, carrying energy and angular momentum away from the system. In a BNS merger scenario, the orbital period of the system decreases due to the aforementioned loss of energy with rate:

[3]Russel Hulse and Joseph Taylor shared the Nobel Prize in 1993 for their discovery of PSR1913+16.

$$\dot{P}_{orb} = \frac{dP_{orb}}{dt} \propto -\frac{G^3 M^2 \mu}{c^5} \Big(\frac{4\pi^2}{GM}\Big)^{4/3} \frac{f(e)}{P_{orb}^{5/3}} \tag{4.3}$$

where

$$M = M_1 + M_2$$
$$\mu = \frac{M_1 M_2}{M_1 + M_2}$$

and where $f(e)$ is the term describing the impact on the orbit's eccentricity. From [131] the conclusion that the general relativistic quadrupole formula correctly predicts gravitational radiation is drawn. GW signal is therefore expected for non spherically symmetric systems such as short GRBs. The first evidence of this scenario was confirmed by observation of a BNS merger by Advance LIGO and Advance VIRGO (GW170817) and the electromagnetic counterpart detection by Fermi-GBM and INTEGRAL (GRB170817A) [133]. The priorities of the transient KSP (as exposed in Table 4.1) are driven by GW transients, such as short GRBs.

4.3 CTA observing strategy

Taking a step back from the focus on the short GRBs and GW transients, the present and following sections will summaries the GRB observing strategy proposed by the CTAC, as well as the expected science return. The primary source of alerts (for both long and short GRBs) are expected to be soft gamma-ray instruments, such as Swift, Fermi-GBM and SVOM (planned for launching no later than 2021). Wide-field instruments such as Fermi-LAT, DAMPE, HAWC and LHAASO [85] may possibly produce alert which CTA can follow-up on. Alongside those are other wave-band instruments such as GAIA and LSST or other messenger detectors like GW-interferometers and neutrino observatories [102] [64]. Finally, multi-messenger alerts from GW interferometers are also feasible for short GRB. In all these scenario, the RTA will play a key role in the localisation of the phenomena and the analysis in real-time for the follow-up program (Section 3 and 3.1). Although this work focuses on externally alerted GRBs, the possibility of serendipitous discoveries by the RTA must also be taken into account for a complete study. Being cosmologically distant objects, their rates are expected of equal values for CTA South and North. Considering EBL attenuation at higher energies, LSTs (Section 2.2) will be vital in follow-up observations having both the lower energy threshold and the fastest slewing capabilities. The full array configuration will be of importance for $z \lesssim 1$ redshifts, case in which TeV emission may be feasible to detection for bright events. The observing strategy proposed by CTAC is summarised in Table 4.2.

Strategy	Expected (yr^{-1})	Exposure (h)	Exposure (h/yr)
Prompt follow-up of accessible alerts	∼12	2	25
Extended follow-up for detections	0.5-1.5	10-15	10-15
Late-time follow-up of the GRBs not accessible promptly	∼1	10	10

Table 4.2: Summary of GRB follow-up strategy from [1]. CTA South and CTA North are expected to have an equal amount of required time.

First and foremost, prompt emission follow-up should be carried out with a full-array configuration whenever accessible, namely when these events occur during dark time and their zenith angle is no higher than 70°. The expected alarm rates are of about 5/yr/site for Swift or SVOM and 10/yr/site for Fermi-GBM which, after accounting for some overlap, would result in ∼ 12/yr/site alarm rate [1]. In case of localisation error regions larger than LSTs field of view, tiling strategies and/or a divergent pointing mode must be considered [3]. All available telescopes, especially LSTs, should be employed to guarantee the maximum sensitivity achievable. Once the RTA provides a positive detection, the observation scheduling should account for extended exposure as long as the target is visible and detectable. The latency for the RTA system to alert the VHE photon origin must be, as

previously stated, no more than 30 s. The predicted GRB *detection* rate is of $\sim$ 1/yr/site [44] [43] (recent detections of GRBs by IACTs may contradict these numbers [40], [41] [108]). Lastly, there are cases when the follow-up might not be promptly accessible with the full array, i.e. if a bright event is triggered outside the sites' sky visibility. The program should allow for late-time follow-up as soon as the target becomes visible. Additional follow-up during partial moon time is feasible and could increment the detection rates by up to 50%.

Simultaneous follow-up with other MWL facilities should be pursuit whenever feasible in order to cover as much of the electromagnetic spectrum as possible. These would allow for good parametrisation of the time-dependent, broadband spectra of the afterglow (i.e.) and most importantly would guarantee the extremely important redshift determination (by optical/IR telescopes) without which the scientific return might end up compromised. To this purpose, it is actually desirable to have a dedicated on-site telescope dedicated to CTA follow-ups. It should be able to localise the majority of afterglows with sufficient accuracy as to allow larger telescopes to follow-up on spectroscopic measurements. An IR instrument would be favourable as to cope with optically dark GRB which constitute a large portion of the afterglows, albeit the costs might render it an out-of-reach investment. Moreover, since SVOM will board an optical telescope with red coverage which is expected to localise up to $\sim$ 70% of the afterglows by itself, the need for a dedicated CTA instrument may become less urgent after its launch.

Last but not least, the other portion of observing time which could give scientific return for GRB science is the serendipitous VHE transient target science wherein the RTA will play a key role. The system will analyse data on different timescales, spanning from seconds to hours. The focus of this work is *very-short* timescales (no higher than 100 s). The sensitivity varies as a function of the exposure time and will also have dependence on the VHE sources present in the FoV at time of observation. It rests on the RTA system to grant observing time extension in case of positive detection, as well as issuing the alert to other MWL/MM facilities and reschedule the remaining observations planned for the night. As a rule of thumb, serendipitous detection should be followed-up during the same night or could be carried out the night after. If during data intake the spectral variability and flux patterns are identified, then the observation strategy may be optimised in real-time (i.e. number of hours to observe during the first night, number of telescopes in the configuration, etc.). The total estimation is of 100 h/yr/site during the early phase, in order to account for tests and possible fake alerts, while it would decrease down to 25 h/yr/site after the full array commissioning. Different from the previous programmes (GRB transients and GW transients) observations should be extended up to zenith angle below 60° in any weather conditions. These limits are susceptible of change. The predictions are from a one per $\sim$10000 hours of dark time observation down to one per $\sim$1000 hours [28] [46] [47]. The advantage of this program is, of course, the lack of time delays due to alerts latency and telescopes slewing time, or inadequate localisation which would require the tiling of large error regions as for the GW case. It should be noted that, though GRB events are expected to have isotropic distribution, targeting regions at high Galactic latitudes is largely favoured as to reduce to a minimum the Galactic plane absorption due to ISM density.

4.4 Expected science return

GRB measurements are foreseen in the form of spectra and light-curves for $\sim$1 GRB/yr/site with more than 100 photons above 30 GeV per event [47] [43] [44] and upper limits can be expected for $\sim$10 GRB/yr/site.

Spectra. A handful of well characterised spectra (up to multi-GeV energies) was selected from Fermi-LAT detections and extrapolated to very-high energies, without neglecting to apply an EBL absorption. This sample was used with the purpose of testing the reliability of detection which, down to intervals as short as 20 s of exposure time, resulted in several hundred photons above 30 GeV (with differences due to the assumed EBL). The VHE spectra that can be expected from CTA observations will be extremely valuable for further probes on the EBL at high redshifts through attenuation features, potentially beyond the feasible range for AGN observation.

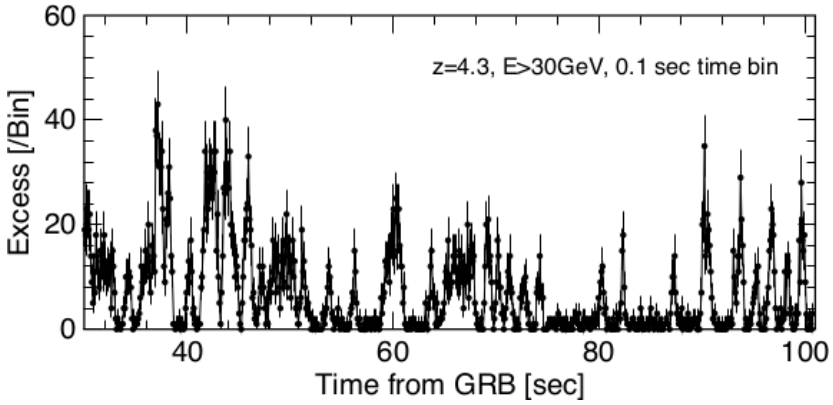

Figure 4.3: Simulated CTA light curve of GRB 080916C at z=4.3, for observed photon energies above 30 GeV with 0.1 s time binning and $t_0 = 30$ s after burst onset. See [51] for template details, and [52] for the EBL reference. More details on the simulation can be found in [47]. **Credit:** CTA White Paper, 2013.

Light-curves. As for the simulation of GRB spectra, light-curves were computed from templates of Fermi-LAT selected bursts extrapolated into the CTA band. An initial delay is taken into account in order to simulate the incoming alert latency and the slewing time of the telescopes ($t_{delay} = 30\,s$). CTA should still be capable of analysing light-curves with high temporal resolution for bright bursts (i.e. Figure 4.3). Of crucial value is the extraction of physics information on energy-dependence which could: *i)* clarify the poorly understood mechanism of GRB prompt and/or early afterglow emission; *ii)* reveal signatures of hadronic emission processes through their peculiar delays at high energies; *iii)* identify intrinsic spectral cut-offs from those due to EBL attenuation as it should remain time-independent; *iv)* probe LIV effects through their expected energy dependence.

Detection rates. The prediction previously discussed have been derived from a GRB population model tuned to match Swift observations, combining VHE assumptions on the spectra via extrapolations from Fermi-LAT observations. There could be an heavy bias on these estimates, as the Fermi-LAT detected GRB reflect only the most luminous phenomena. Thus, depending on their true power at very-high energies, the aforementioned detection rates might be either overestimated or underestimated (possibly the latter [40] [42]).

Source localisation. Another scientific return of extreme importance in the context of MWL and MM astrophysics, is the expected localisation of phenomena alerted via other MWL and MM facilities. In particular for alerts received from MM facilities, the uncertainties tend to cover large areas of the sky and follow-up campaigns would benefit from the more precise pointing information the CTA can provide. This work is the first attempt to constrain and quantify the RTA performance in MWL/MM transients localisation.

4.5 State of the art for very-high energy GRB science

There have been no clear detections for VHE (Section 4.2.2) gamma-ray burst afterglow emission before the year of 2018. On the 20th of July 2018, H.E.S.S. began the observation of a Fermi-GBM triggered gamma-ray burst (GRB180720B, at $z = 0.635$) approximately ten hours after the onset of the event ($T_0 + 10.1$h). With a $T_{90} = 48.9 \pm 0.4$ s, the burst is categorised as a long GRB, with isotropic energy of $E_{iso} = (6.0 \pm 0.1) \times 10^{53}$ erg[4] between 50 and 300 keV. H.E.S.S. observation achieved a detection significance of $\sim 5\sigma$ [41]. The VHE emission (lightcurve in Figure 4.4(a)) indicates the presence of very-energy particles in the afterglow radiation, consistent with efficient γ-ray emission seen in other astrophysical sources. The particle acceleration probably occurs at the forward shock (right hand-side in Figure 4.2), when the compression propagates through the circumburst medium. Two radiation processes have been suggested by the authors as plausible dominant contributions: *i)* synchrotron emission by an electron population in the local magnetic field and *ii)* synchrotron

[4] 1 erg = 10^{-7} J.

self-Compton scattering. The synchrotron self-Compton (SSC) component implies the expectancy of a double-bump feature in the spectral energy distribution, whereas a synchrotron model would predict a single broad component.

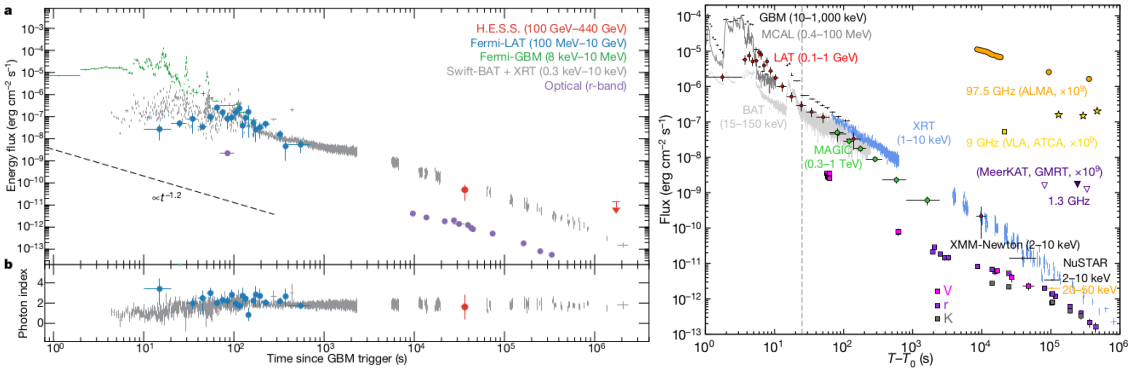

(a) (b)

Figure 4.4: **Left.** Multi-wavelength lightcurves of GRB180720B (in particular, H.E.S.S. measures correspond to red circles). The black dashed line indicates a temporal decay with $\alpha = -1.2$. The top panel represents the energy flux temporal evolution, while the bottom panel shows the respective spectral index. Error bars correspond to 1σ. **Right.** Multi-wavelength lightcurves (energy flux versus time) of GRB190114C. MAGIC measurements for the 0.3-1TeV energy range (green circles) are compared with lower frequencies data. The vertical dashed line marks approximately the end of the prompt-emission phase, identified as the end of the last flaring episode. Error bars correspond to 1σ. **Credits:** Abdalla et al. 2019 (a), and Acciari et al. 2019 (b).

Few months after H.E.S.S. pioneering detection, MAGIC observed a gamma-ray burst (GRB190114C, at $z = 0.4245$) triggered by Swift-BAT on January 14, 2019. Its duration was measured by Fermi-GBM ($T_{90} = 116$ s) and Swift-BAT ($T_{90} = 326$ s), classifying the event as a long GRB. Observation started at $T_0 + 57$ s and lasted up to $T_0 + 15\,912$ s. For the first time in very-high energy GRB science, TeV radiation was detected (E$>$ 0.2 TeV) with outstanding high significance (above 50σ in the first 20 minutes) [40] [42]. The authors found that the TeV lightcurve (Figure 4.4(b)) behaves similarly to those in the keV and GeV energy bands. Although prompt contributions to the TeV emission cannot be ruled out, the observed properties seem to suggest this component to be associated with the afterglow radiation. The isotropic equivalent energy radiated between $T_0 + 62$ s and $t_0 + 2\,454$ s is of $E_{iso} \approx 4 \times 10^{51}$ erg in the energy range between 0.3-1 TeV. Much of the high-energy emission (up to GeV energies) has been attributed to afterglow synchrotron emission of electrons. The TeV emission cannot be simply explained as spectral extension of the GeV radiation as it cannot explain the observed energetic[5]. The authors claim that a separate spectral component beyond the synchrotron emission is unequivocally confirmed by this observation.

A third detection was announced by H.E.S.S. on 30 August 2019 [108]. A follow-up observation of one of the nearest GRB afterglows (GRB190829, at $z = 0.0785$) was carried out under good conditions. The observation started at $t_0 + 4h20$ and lasted a total of 3h50. Preliminary on-site analysis shows a gamma-ray excess significance above 5σ compatible with the direction of GRB190829A. Further analysis are still on-going. It must be said that the template used for this work, described in the next section, predates the observations of GRB180720B, GRB190114C and GRB190829.

4.6 Science case: blind-search and follow-up of a short GRB afterglow

A blind-search and follow-up analysis pipeline was developed for this work (Chapter 5). The aim is to perform a blind-search on an externally alerted transient event over a region of the sky (comparable to the array field of view) in order to localise the transient source in the least possible amount of time.

[5]The energy of afterglow synchrotron photons is limited to a maximum value (synchrotron burn-off limit) which is dependent on the bulk Lorentz factor.

If positive detection is achieved, a follow-up observation with real-time full field of view maximum likelihood analysis is carried out for as long as the source remains detectable with significance over a given threshold (i.e. 5σ). The observation should last until 2 hours after the last acquired positive detection. The alert uncertainty is assumed comparable to CTA (LST) field of view, since this study does not aim at investigating tiling strategies [3]. The source can thus be found within a single pointing of the array. This can be obtained with alerts produced from observations of at least three gravitational interferometers (i.e. 2025 onward scenario) or from high energy satellites (i.e. Fermi-GBM). The average case scenario for the delayed start of CTA observations ($t_{delay} = t_{alert} + t_{slew}$) is assumed t_{delay} =30 s (∼10 s for the alert reception and ∼20 s to account for the slewing of the telescopes). These scenarios assume an immediate and automatic system of GW/satellite alerts which is clearly not realistic, but precise characterisation of the array response is not within the scope of this work, nor is the optimisation of observing strategy with respect to varying t_{delay}. The chosen t_{delay} =30, 50 s must be considered arbitrary use case assumptions in preliminary studies on SAG. Considerations on detection of fainter late-time observed sources can be found in Section 6.5. In this work both nominal and degraded sensitivity are considered (Section 3.6), within 30 GeV - 150 TeV energy range, as to investigate the RTA domain and feasibility with respect to the scientific requirements.

4.6.1 The GW COSMoS catalogue and the POSyTIVE project

The template in use is part of a larger project for population synthesis of the VHE emission of gamma-ray bursts. Specifically for short GRB, a connection between simulated EM counterpart and the a progenitor GW emission is provided by the population synthesis of the GW COSMoS catalogue [145]. A number of independent (randomised) realisation of HE counterpart are generated for a given GW detection and sky localisation uncertainty map of the simulated NS-NS mergers.

GW COSMoS. The catalogue is a public database of simulated NS-NS mergers, providing the associated GW detection and sky localisation with Advanced LIGO and Advanced VIRGO. In [2] [3] the GW detection rate, the GW sky localisation and the joint GW and gamma-ray detection rates are predicted under the assumption that each coalescence is associated with a short Gamma-ray Bursts. Data are given for a set of 1000 realizations (or runs), each one corresponding to an observing time of 1 year [2]. The facilities considered for EM counterpart detection are: the LAT and GBM instruments on-board the Fermi satellite and CTA.

POSyTIVE. The POpulation Synthesis Theory Integrated model for Very-high Emission is a project with the goal to realistically constrain the GRBs detection rates for CTA, enable preparatory studies on individually simulated GRBs and characterise the time-resolved spectra analyses expected from CTA performances. The output will be a library of simulated GRBs which can be used for strategy testing in the CTA follow-up program scheduling, or studying the physical parameters space wherein CTA will perform its science in the future. A mocked GRB population was created from 40 year data of MWL observations. Intrinsic spectra are also assumed, in order to calibrate the simulated GRBs with the observed sample, computing fluxes and fluences ($L_{iso,i}$ and $E_{iso,i}$, respectively) in the energy band wherein the real measurement is found. The afterglow onset time distribution is inferred from available measurements and lower limits. Prompt and afterglow emission for long and short GRBs are simulated for given position, redshift, isotropic energy, Lorentz factor and prompt duration [53].

▷ *Prompt models.* The prompt models of the simulated GRB population was investigated with a large set of synthetic spectra, given the isotropic energy, redshift, Lorentz factor and prompt duration. The possible contribution from relativistic protons [136] was neglected. The radiation mechanism at play are the synchrotron emission from accelerated electrons moving in an amplified magnetic field, and the inverse-Compton component due to synchrotron photons scattered to higher energies by relativistic electrons. Synchrotron self-absorption at low-energy and pair production via photon-photon annihilation channel are also taken into account.

▷ *Afterglow models.* The afterglow radiation comprises of a standard synchrotron and synchrotron self-Compton scenario (SSC) due to electrons acceleration by a forward shock. Parameters such as ϵ_E and ϵ_B describe the shock-dissipated energy fraction used to accelerate the electrons and to amplify the

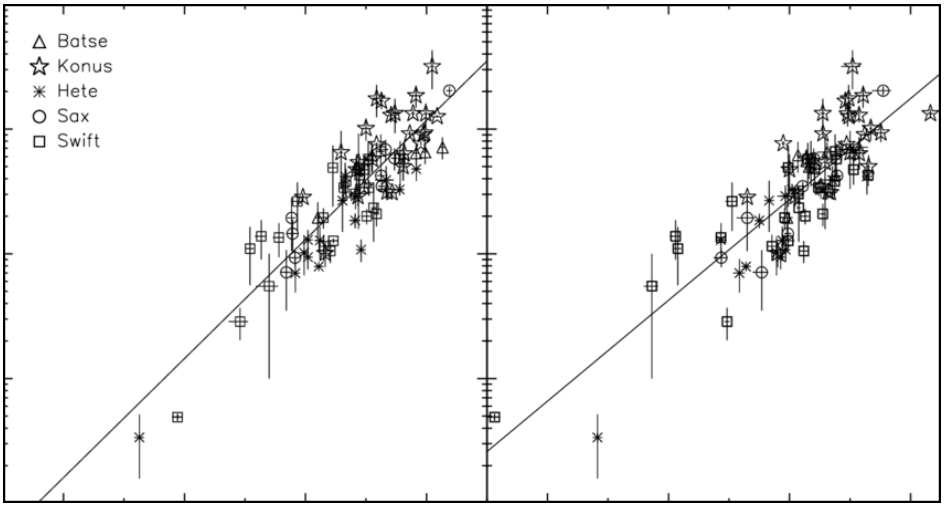

Figure 4.5: Correlations between E_{peak} and E_{iso} (left) and between E_{peak} and L_{iso} (right) for 83 GRBs with measured redshift and spectral parameters [135]. **Credits:** Nava et al. 2009.

magnetic field, respectively. The assumption is to have efficiently accelerated electrons distributed as a power law in their SED ($dN(\gamma)/\delta\gamma \propto \gamma^{-p}$ where γ is the electron Lorentz factor)[6]. In the modelling of the afterglow emission, the density distribution of the external medium is of obvious importance. A radial profile is assumed ($n(r) = n_0 r^{-s}$), with a different parametrisation for short ($s = 0$) and long ($s = 2$) gamma-ray bursts. Unfortunately, the uncertainties on the free parameters can greatly impact the resulting emission, effectively reducing the predicting power.

4.6.2 Extragalactic Background Light absorption

Being cosmologically distributed sources, GRBs are affected by the EBL absorption. The templates provided for this study did not account for it, thus it was necessary to natively compute the absorption. The extragalactic background light (emission in the 0.1-1000μm wavelength region, from IR to UV) comprises the integrated light from resolved and unresolved extragalactic sources, and the light from any truly diffuse background (excluding the cosmic microwave background). This diffuse background component of radiation is naturally affected by redshift and dilution of photons density due to the expansion of the universe, as well as the absorption and re-emission (in the IR wavelengths) by dust. The EBL plays a key role in the propagation of gamma-rays, since high-energy photons are attenuated by photon-photon interactions producing electron-positron pairs. This interaction effectively removes a quota of these photons from the observed flux, consequently modifying the spectra with absorption-like features. Many authors have tried to best understand and constrain EBL absorption and four main techniques have been efficiently developed [26]: *i)* forward evolution setup with initial cosmological conditions; *ii)* backwards evolution setup from a given prescription of current galaxy emissivity constrains; *iii)* galaxy evolution properties inferred over a set wavelength range; *iv)* direct observation of galaxy evolution properties over redshift.

Examples of EBL calculations are by Domìnguez et al. (2011) [26], Franceschini et. al (2008) [138] and Gilmore et al. (2012) [23]. In this work an EBL model from Gilmore et al. (2012) was implemented, after discussion and feedback with the GRB experts from the CTAC and members of the POSyTIVE project. In [23] two models were presented with different extinction recipes: *i)* a *"fixed"* model that maintains constant the parameters of the extinction recipe at all redshift and adjust them to match observed relations between UV and IR luminosity for nearby galaxies; *ii)* a *"fiducial"* model with redshift-dependant parameters, tuned to match the observed UV and optical luminosity functions (see [23]) at all redshift when measured. This study makes use of the fiducial model only, wherein the total dust extinction is scaled by a factor $(1 + z)^{-1}$ at non-zero redshifts, the opacity and lifetime of molecular clouds is scaled by a factor of z^{-1} at all $z > 1$. In order to attenuate the template's

[6]Possible modification to these spectra can be caused by Klein-Nishina (KN) effects.

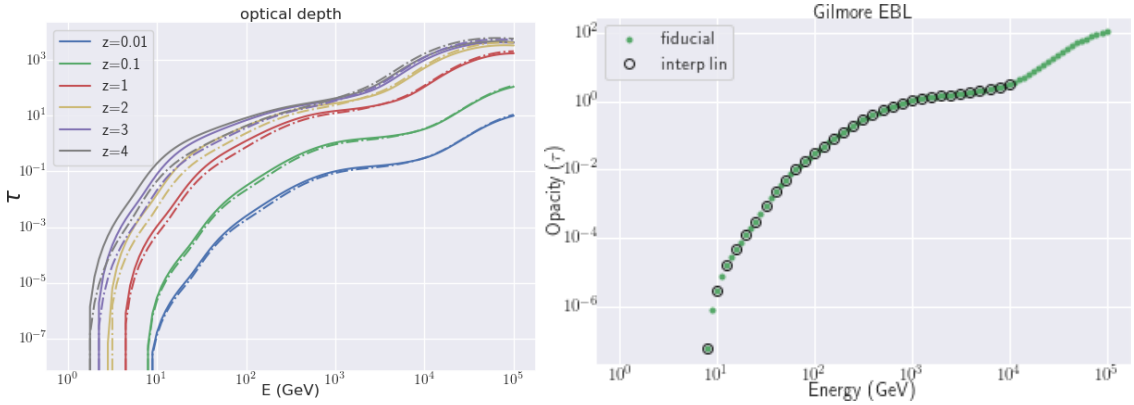

(a) (b)

Figure 4.6: **Top-left panel:** Optical depth dependence on energy given the redshift, as computed from the work of [23] for a selected set of redshift. In continuous lines are the *f*iducial model optical depth values, while in dash-dotted lines represent the *f*ixed model ones. **Top-right panel:** Interpolation from the opacity table of the fiducial model ($z = 0.1$), used to compute the absorbed spectra (Equation 4.4).As the template's energy bins do not necessarily correspond the optical depth (τ) table values, an interpolation between the two nearest energy values were used to extrapolate each energy bin τ_i.

flux with EBL absorption, optical depth values from the fiducial model tables[7] were used (Figure 4.6) according to template's redshift and the energy range of the simulation. The template spectra were modified with an exponential cut-off absorption, given by:

$$F^{ebl} = F \cdot e^{-\tau} \tag{4.4}$$

The optical depth for the fiducial model is (from [23]):

$$\tau(E_\gamma, z_0) = \frac{1}{2}\int_0^{z_0} dz \frac{dl}{dz} \int_{-1}^{1} du(1-u) \int_{E_{min}}^{\infty} dE_{bkg} n(E_{bkg}, z)\sigma(E_\gamma(1+z), E_{bkg}, \theta) \tag{4.5}$$

where E_{min} accounts for the redshifting of the gamma-ray energy, $E_{bkg} = 4m_e^2c^4/E_\gamma$ defines the characteristic energy and dl/dz is the cosmological line element:

$$\frac{dl}{dz} = \frac{c}{(1+z)H_0} \frac{1}{\sqrt{\Omega_m(1+z)^3 + \Omega_\Lambda}} \tag{4.6}$$

assuming a ΛCDM universe and cosmological parameters based on WMAP5 (5-year Wilkinson Microwave Anisotropy Probe) [23]).

4.6.3 Afterglow template

The afterglow emission spectra and lightcurves template `run0406_ID000126`[8] used in this study belongs to the first POSyTIVE catalogue and the simulation is based on GWCoSMOS catalogue of BNS mergers [3] (Section 4.6.1). As described in the above, an EBL absorption from [23] was applied. The template is a FITS format file of energy and time log-binned (ten bins per decade) spectra, from 0.1 to 10^4 GeV and from 0.1 to 10^6 s, with values given in ph/cm^2/s/GeV. The source has celestial coordinates (RA$_S$=33.057°, DEC$_S$=-51.841°) and redshift $z = 0.097$ corresponding to 430 Mpc of distance. The prompt emission of the gamma-ray burst is $E_{iso} = 1.48 \cdot 10^{51}\, erg$ of isotropic energy and the viewing angle is of 2.567 deg. The afterglow model is generated from a short GRB prompt interaction with circumburst medium (i.e. ISM, IGM). The BNS merger simulation from which it was computed was detected by $n = 3$ gravitational-waves interferometers with a combined signal-to-noise ratio equal to $SNR = 12.4$. For the scope of this work (blind-search of an externally alerted gamma-ray bursts), the source position is assumed unknown. Instead of the GRB coordinates, the pointing of the

[7] From Gilmore et al. (2012): `http://physics.ucsc.edu/ joel/EBLdata-Gilmore2012/`
[8] **Credits:** L. Nava

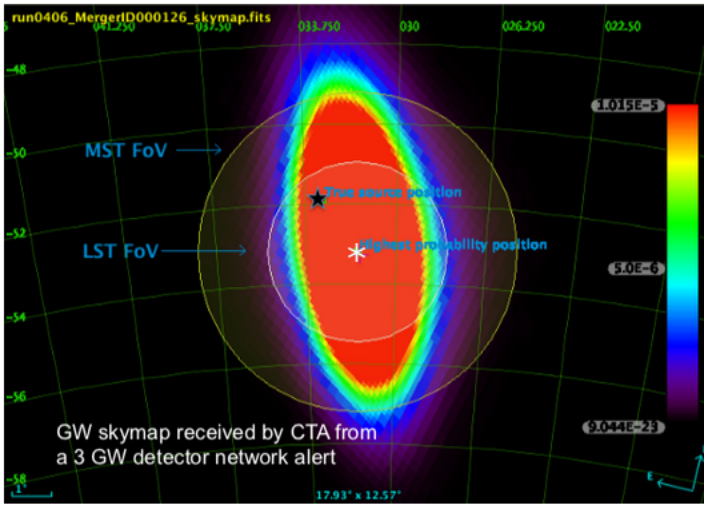

Figure 4.7: Simulated probability sky distribution corresponding to the simulated merger alert ID XXYY from the GWCosmos database [145]. The coordinates of maximum probability are used as pointing coordinates (white star symbol) for the RTA blind-search and follow-up. The true position (black star symbol) is assumed unknown. MST and LST field of view have been plotted for comparison with the alerted region size. **Credit:** Patricelli et al. 2018. Image by Stratta et al. CTA Symposium (2019).

array was aligned with the maximum probability centroid (RA_P=31.582, DEC_P=-53.211) of the alert localisation probability map, shown in Figure 4.7. As one can see from the probability map, the source falls within the LST field of view, thus only one pointing of the array is necessary for the observation. The simulated sky region is centred on the pointing of the telescope, hence the source is simulated with an off-axis angle given by the difference between the pointing coordinates and its true coordinates ($\theta^{off}_{RA} = -1.474$, $\theta^{off}_{DEC} = -1.370$).

The afterglow emission is described, as mentioned, over four orders of magnitude in energy, from 1 GeV to 10 TeV, and seven orders of magnitude in time, from 0.1 to 10^6 s. The source spectra is defined by ten log-spaced bins per energy decade, its lightcurves by ten log-spaced time bins per decade. In Figure 4.8 spectra and lightcurves of the template are shown, with and without EBL absorption for a number of temporal bins (spectra) and energy ranges (lightcurves). In the left panel one can find three spectra, corresponding to the afterglow emission between 50-63 s, $5\,000 - 6\,300$ s and $500\,000 - 630\,000$ s, approximately. The emission is, as expected, dominant in the low energy ranges (E$\lesssim$10 GeV), and the flux intensity decays with passing time (early time emission: blue continuous time and orange dot-dashed line; late time emission: purple continuous line and brown dot-dashed line). EBL absorption impacts on the intrinsic flux more relevantly for E$\gtrsim$100 GeV only, justifying the use of Equation 5.4 to compute the integral flux. On the right panel a sample of lightcurves is plotted for different energy ranges, featuring the integral flux on the y-axis. The integration is computed within the energy coverage for LSTs (20-150GeV), MSTs (150GeV-10TeV), SSTs (10-300TeV) and an arbitrary chosen full-array energy range used in this work (30GeV-150TeV)[9]. The temporal behaviour of the event rises to its peaking flux within the first 15-20 s from the afterglow onset (Section 4.2.1). The decaying power law is perfectly described from ∼250 s onward, due to the presence of a plateaued/multi-peaked regime previous to that. The highest integral flux is achieved, not surprisingly, for LST-only array configuration since there is no absorption attenuating the source. The continuous green line (unabsorbed lightcurve) and the red dot-dashed line (EBL absorbed lightcurve) are perfectly overlaid. When observing the afterglow with MST-only (purple and brown colours) or SST-only array (violet and grey colours) configurations the EBL attenuation weights progressively more on the integral flux, so much as to account for almost an order of magnitude difference in the SST-only lightcurve. Let's consider the chosen energy range for this work (30GeV-150TeV) though. The safe cut at low energy (which dominates the afterglow emission) reduces the integral flux by a significant fraction (≈15%) but the chosen threshold is low enough to avoid relevant attenuation. One can see from the difference

[9]The selection is based on safe cut suggestions for `ctools` software package general use.

in the integral flux between the unabsorbed (continuous blue line) and absorbed (dot-dashed orange line) lightcurves that the EBL attenuation is not relevant under the chosen conditions. To conclude, a comparison of this template with the recently observed GRB190114C lightcurve is presented in Figure 4.8. Data were taken from the MAGIC published results[10] and compared with the template flux integrated within the same energy range of MAGIC observation (300 GeV - 1 TeV). As one can see, this study is carried out on a model source up to 1.5 order of magnitude fainter. Therefore, any positive detection achieved by analysing events such as that of `run0406_ID000126` would also represent successful detection of brighter sources such as GRB190114C and GRB100720B (Section 4.5).

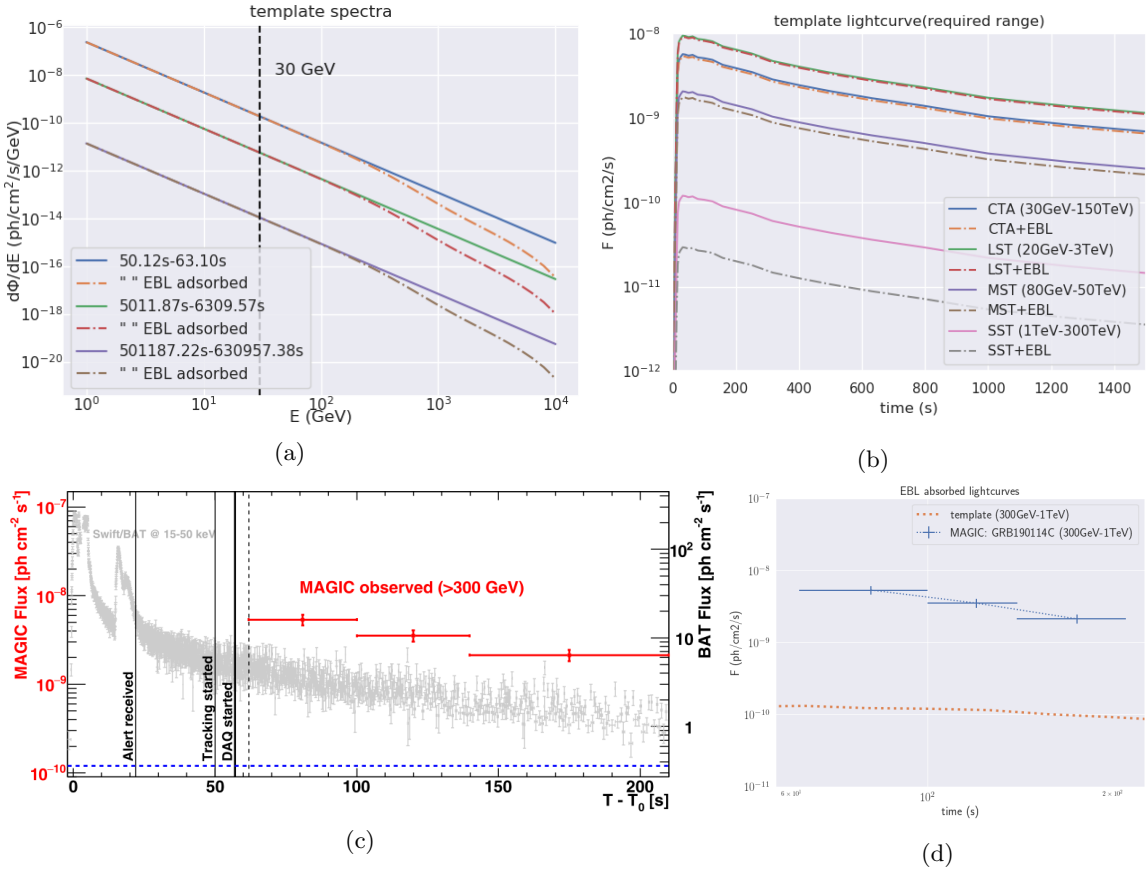

Figure 4.8: **Top left** A sample of the template spectra at different time windows ($\sim 50-60$ s, $\sim 500-600$ s and $\sim 5000-6000$ s). Continuous lines represent the unabsorbed modelhttps://www.overleaf.com/project/5d0759f24d6b483267ce7812 provided by the GRB experts of the CTAC, while dot-dashed lines represent EBL absorbed spectra. generated for this study. Note how the EBL absorption becomes relevant only for $E \gtrsim 100$ GeV. **Top right** Template lightcurves (integral flux as a function f the observing time, up to 1500 s) at different energy ranges. Continuous lines represent the unabsorbed model while dot-dashed lines represent EBL absorbed lightcurves. The plot shows the lightcurve for LSTs, MSTs and SSTs only configuration in the respective core energy range. Additionally, the CTA South full-array configuration in the energy range 30 GeV - 150 TeV is also shown. **Bottom** In order to compare the afterglow template lightcurve with real data, MAGIC detection GRB190114C [40] [42] has been reported with integral photon flux (above 30 GeV) as a function of time (left). The template lightcurve in the energy range of the MAGIC observation is shown for comparison (right). **Credits:** MAGIC collaboration (bottom left).

[10] `http://vobs.magic.pic.es/fits/#database`

Chapter 5

A prototype pipeline for RTA: blind-search and follow-up of GRBs

---

In this chapter one of the currently available science tools that allow for a maximum likelihood analysis of gamma-ray astronomy and IACTs data will be introduced (Section 5.1), alongside a brief description of those implemented in the code written for this study and an overview of source and background models. The pipeline developed will be outlined in Section 5.2 with a particular focus on inputs, outputs and setup (Section 5.2.1). Section 5.2.2 will present some details on the simulations, while in Section 5.3 a technical description of natively implemented utilities and side scripts will follow. Section 5.4 will conclude the chapter by constraining the theoretical context for post-processing data manipulation, namely stating definitions of the great-circle distance (Section 5.4.1), the Rayleigh distribution (Section 5.4.2) and confidence interval determination (Section 5.4.3).

5.1 Scientific tools: ctools and Gammalib

GammaLib software package is a general framework for the analysis of gamma-ray events data on top of which *ctools* software package is built. The latter is a suit of software tools enabling flexible workflow for IACT event data analysis.[6]. Both software packages are developed as open source codes[1][2] GammaLib is a single shared library package mostly written in C++. It contains classes, functions and some global variables needed to analyse gamma-ray event data, with all functionalities natively implemented. This strategy assures independence from operating systems and user-friendly installation.

In `Gammalib` an observation is defined as a period of time wherein an instrument was taking data in a stable configuration which can be described by a fixed Instrument Response Function. It should be noted that internally energies are stored in MeV and time zero is defined at 1st January 2010, 00:00:00 (TT).

[1] Download: `http://cta.irap.omp.eu/ctools/admin/download.html`
[2] Documentation: `http://cta.irap.omp.eu/ctools/` and `http://cta.irap.omp.eu/gammalib/`.

The analysis implemented in this work is that of a full-FoV maximum likelihood, with source description given by spatial and spectral models (Section 3.4).

Spatial models. Spatial source components can be either modelled as point-like sources, radially symmetric sources, elliptical or diffuse ones. Background-type objects are instead modelled without spatial parameters although the spatial characterisation is, in a way, taken into account by the convolution of data with the IRF of choice. In this work sources have been modelled as point-like objects, with Right Ascension and Declination in degrees. In Listing 5.1 a point-like source model example is reported, with coordinates values set to the short GRB true position (Section 4.6.3).

```
<source name="Src001" type="PointSource" tscalc="1">
    ...
    <spatialModel type="PointSource">
        <parameter
        scale="1.0" name="RA" min="-360" max="360" free="0"
        value="33.057" />
        <parameter
        scale="1.0" name="DEC" min="-90" max="90" free="0"
        value="-51.841" />
    </spatialModel>
</source>
```

Listing 5.1: Spatial model example. The source *name* attribute is arbitrary while $tscalc = 1$ implies that a TS value computation is required. The parameter *name* attribute identifies the coordinate and the coordinates system, while *value* and *scale* compute the coordinate value. *min* and *max* attributes identify the parameter range constraints for a maximum likelihood fitting (Section 3.4), where $free = 0$ identifies free parameters and $free = 1$ specifies fixed parameters.

Spectral models. Implemented spectral model collects a variety going from the simple power law to a user define model through external ASCII files, i.e. for the MC simulations described in Section 4.6.3). Among the models available there are constant functions, power law, broken power law and exponentially cut-off power law, logarithmic parabola and Gaussian profile. For this work a user defined function has been utilised for simulating the source, while the analysis assumes a simple power-law model, with spectral index fixed at -2.48 and pivot energy of the MeV order magnitude. The model is defined by the equation:

$$M_{spectral}(E) = k_0 \Big(\frac{E}{E_0}\Big)^{\gamma} \tag{5.1}$$

where k_0 corresponds to the intensity in $ph/cm^2/s/MeV$, E_0 is the normalisation[3] value in MeV ($E_0 = 1$ MeV) and γ is the spectral index. The integrated flux would thus be:

$$\Phi(E) = \int_{\Delta E} M_{spectral}\, dE \tag{5.2}$$

$$= k_0 \int_{\Delta E} \Big(\frac{E}{E_0}\Big)^{\gamma} dE \tag{5.3}$$

$$= \frac{k_0}{\gamma + 1} \Big[\Big(\frac{E_{max}}{E_0}\Big)^{\gamma+1} - \Big(\frac{E_{min}}{E_0}\Big)^{\gamma+1} \Big] \tag{5.4}$$

where E_{max} and E_{min} are the selected energy thresholds of the event.

In Listing 5.2 is an example for the user defined function model used for simulations. The source spectrum values are stored in an external ASCII file (i.e. *data/spec.out*) with data columns of energy (MeV) and spectral intensity (ph/cm^2/s/MeV). In Listing 5.3 is an example of a simple power-law model instead, similar to those that have been used for the maximum likelihood analysis in this work.

[3] PivotEnergy should always be a fixed parameter.

```
<source type="PointSource" name="Src001" tscalc="1">
    <spectrum type="FileFunction" file="data/spec.out">
        <parameter
        scale="1e+00" name="Normalization" min="1e-7" max="1000"
        free="1" value="1.00000" />
    </spectrum>
    ...
</source>
```

Listing 5.2: Spatial model example. The source *name* attribute and $tscalc = 1$ correspond to the spatial model ones. The spectrum parameters here presented are for an externally defined model with associated *file* attribute linking to spectral data. This model requires a normalisation *name* attribute, with *scale*, *value*, *free*, *min* and *max* attributes being the quantities previously described.

```
<source type="PointSource" name="Src001" tscalc="1">
    <spectrum type="PowerLaw">
        <parameter
        name="Prefactor" scale="1e-16" value="5.7"
        min="1e-07" max="1e7" free="1"/>
        <parameter
        name="Index" scale="-1" value="2.48"
        min="0" max="5.0" free="0"/>
        <parameter
        name="PivotEnergy" scale="1e6" value="1"
        min="1e-07" max="1000.0" free="0"/>
    </spectrum>
    ...
</source>
```

Listing 5.3: Spatial model example. The source *type*, *name* attributes and $tscalc = 1$ are as previously described. The spectrum is parametrised as a simple power-law, with Prefactor (i.e. intensity), Index (i.e. spectral index) and PivotEnergy (i.e. energy normalisation value) entries. *scale*, *value*, *free*, *min* and *max* attributes correspond to the aforementioned quantities.

Background models. The background modelling requires the specifications of the instrument (i.e. CTA, HESS, MAGIC, VERITAS) and the type of background to be applied. Among the choices are models based on the templates contained in the IRFs, which predict the background rate as function of the position in the field of view and measured energy in units of events/MeV/s/sr. No spatial component needs to be specified for the background model since the spatial (and spectral) information is already contained in this template, multiplying it by a spectral law (i.e. simple power law). An example is in Listing 5.4.

```
<source name="Background" type="CTAIrfBackground" instrument="CTA">
    <spectrum type="PowerLaw">
        <parameter name="Prefactor" scale="1" value="1.0"
        min="1e-03" max="1e+3.0" free="1"/>
        <parameter name="Index" scale="1.0" value="0.0"
        min="-5" max="+5.0" free="1"/>
        <parameter name="PivotEnergy" scale="1e6" value="1.0"
        min="0.01" max="1000.0" free="0"/>
    </spectrum>
</source>
```

Listing 5.4: Spatial model example. The source *type* and *name* attributes are as previously described, the background model lacks of course the entry for a TS value computation. The spectrum is parametrised as a power-law.

Tools description. The following list briefly describes all tools that were used in this work (for more in-depth information, see [6] [7]), either within the pipeline or through standalone utility scripts:

• `ctobssim`: performs a MC simulation of an astrophysical event, with instrument characteristics specified by the IRF. Inputs are: source and/or background model, calibration database and IRF, pointing direction, field of view, time interval, energy interval and the seed of the simulation allowing for multiple independent generation of the same event. The output is a photon list, or a collection of

photon lists.

• `ctselect:` applies event selection to an event list. Inputs are: a photon list or a collection of photon lists, selection centre's coordinates in astrophysical units, radius of the region of interest, time interval and energy interval. The output is a photon list, or a collection of photon lists.

• `ctskymap:` generates a count map, or skymap, of the observation with or without background subtraction. Inputs are: a photon list and a collection of photon lists, calibration database and IRF, energy interval, axes size, pixel size, image centre reference and background subtraction type (i.e. none, ring, IRF). The output is a FITS file count map of the event.

• `cssrcdetect:` executes a blind-search on a smoothed count maps through a peak-detection algorithm for a given number of sources, with localisation acceptance threshold above a given significance. Inputs are: a sky map, source type model (i.e. point-like), background type model (i.e. IRF), acceptance threshold (Gaussian sigma), maximum number of candidates allowed to be detected, correlation kernel radius (required to smooth the sky map) and eventually exclusion regions wherein known sources or contaminated regions are. Output are a DS9 region file with the detected candidates' coordinates and a compiled model.

• `ctlike:` performs a full field of view, multi-parametric maximum likelihood analysis for binned or unbinned analysis (Section 3.4). Inputs are: a photon list or a collection of photon lists, a source model or a model of a list of sources specifying free and fixed parameters, calibration database and IRF. The output is the best fit model, with adjusted free parameter values and relative errors and a optionally the test statistic value of the analysis.

• `cssens:` computes the differential or integral sensitivity using maximum likelihood fitting of a test source. Inputs are: a photon list or a collection of photon lists, source name, calibration database and IRF, exposure time, region of interest radius, energy interval and energy bins, type (i.e. differential, integral) and significance threshold (Gaussian sigma). The output is an ASCII table containing the mean logarithmic energy and the boundaries of the energy bin, as well as the sensitivity in terms of the minimum detectable flux in Crab units, in photons (ph/cm2/s) and in energy (erg/cm2/s). Finally, the sensitivity is also given as the test source spectrum evaluated at the mean logarithmic energy multiplied by the energy squared (erg/cm2/s).

5.2 Outline of the pipeline

The code is entirely written in Python3.6+ with natively implemented functionalities (Section 5.3) and using `Gammalib` and `ctools` (Section 5.1) software package utilities. The aim is to perform a blind-search for an externally alerted GRB and, if positive detection is achieved, to follow-up its afterglow emission with a full field of view maximum likelihood analysis (Section 3.4) performed in real time. Three versions of the analysis pipeline have been developed, accounting for different needs required by the study: *i)* `rta-followup.py` that executes a follow-up scenario along the streaming intake of data from an ongoing observation; *ii)* `rta-blindsrch.py` which consists in a single time-framed analysis gathering information on the statistical distribution of parameters, cycling over a sample of independent realisation of the same event; *iii)* `rta-wilks.py`, a single time-framed analysis on empty fields allowing for Wilks' theorem verification (Section 3.5). In Figure 5.1 a flow-charts is used to outline the workflow of the pipeline, highlighting the most important inputs, steps and outputs. Three main blocks group the most critical procedures: *a)* the setup, accounting for the generation of data due to lack of real observations; *b)* the RTA performance, including all necessary steps required by the analysis; *c)* the outputs which are both accessible real time and at later times for post-processing data manipulation. The part of the flow-chart that is engulfed in a red, continuous-line rectangle correspond to live tasks that the pipeline would require in a real-case scenario. The part contained by the red, dashed-line rectangle emphasises the critical part of the RTA performance instead (not implemented in Wilks' theorem verification).

Starting from the top left of the flow-chart, light-blue rectangles identify inputs for the simulation procedure. These include all the use-case assumptions (more in Section 5.2.1), a source template and the IRF. Green rectangles represent tools from `ctools` software package which have been utilised throughout the pipeline, i.e. `ctobssim` (Section 5.1). The setup is completed once the gamma-ray bursts afterglow has been simulated, step which takes place before the actual core of the code as it

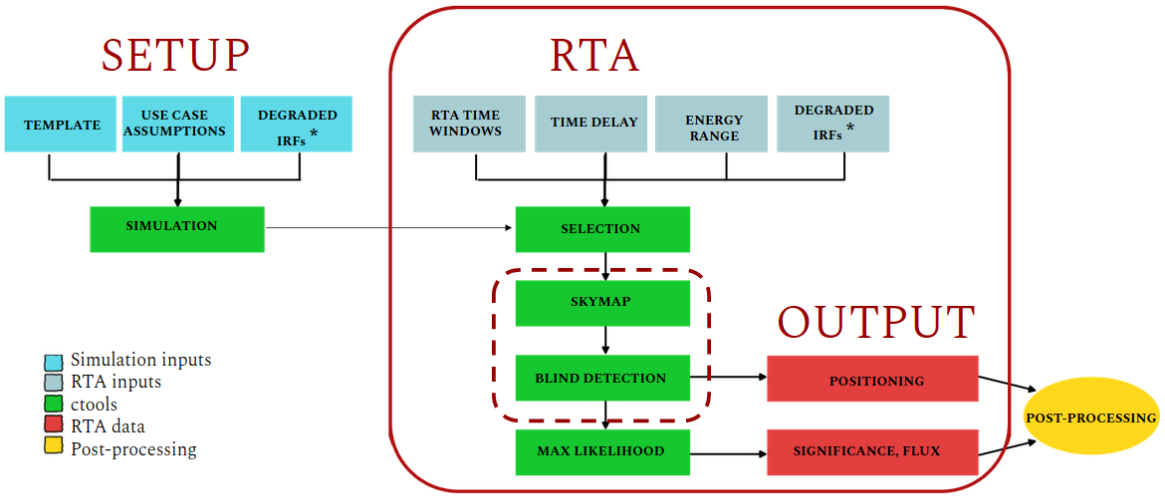

Figure 5.1: Flow-chart of the pipeline. Three main blocks are presented: the simulation setup (top-left), the RTA performance (centre) and the outputs generation (bottom-right). The post-processing data manipulation is executed using the pipelines' products. The colour code represents simulations input in light-blue, RTA inputs in cerulean, `ctools` tasks in green and outputs retrieving in red. In yellow is the post-processing data manipulation instead. Degradation of the IRFs has been emphasised among the outputs, for the crucial role played by the lower sensitivity expected by the RTA requirements.

would require substitution with the incoming stream of data for a real observation. The workflow then moves onto the pipeline's main block: the real-time analysis performance. Cerulean rectangles identify specific inputs required by the RTA (the integration time for time resolved analysis, the energy range, the delay accounting for the alert latency and the slewing of telescopes and, lastly, the IRF) while green rectangles again represent `ctools` utilities. Taking the simulated source along the RTA inputs, the code proceeds to execute data selection by producing photon lists of all events occurred within the specified time and energy intervals. While *iii)* jumps to the maximum likelihood analysis, *i)* and *ii)* follow through the production of a count map (with parameters as in Table B.1 of Appendix B.2) and the subsequent blind search for candidate sources (Section 5.1 `ctskymap` and `cssrcdetect` respectively). The final procedure performed by the RTA block of the pipeline is the maximum likelihood fit. Taking the selected data as input alongside the source and background models produced by the peak-search algorithm, it generates the best fit source and background models for a maximum number of candidates (Section 5.2.1). The outputs generated by the RTA block are obtained immediately after its conclusion, and are shown in Figure 5.1 within red coloured rectangles. Outputs are retrieved from models and data products, they are instantaneously accessible before their finale storage (i.e for displaying). Rather than displaying them on-the-fly, though, for the scope of this study it was chosen to store all outputs in data tables and access them only in post-processing.

5.2.1 Inputs and outputs.

The main inputs are: a configuration file, the calibration database and IRF, pointing coordinates, the delayed time for the start of the observation with respect to the onset of the transient emission, time frames duration, simulation and selection energy ranges, radius of the region of interest, sky map pixel size and pixel numbers for each axes, maximum number of candidates which are allowed blind-detection and their acceptance threshold, correlation kernel radius for the sky map smoothing and the minimum significance required for positive detections. Specific inputs for the statistical analysis pipeline are: the number of independent simulations required. Specific inputs for the follow-up pipeline are: the total duration of the observation, the duration of a single run during the observation and the total amount of additional time to follow-up with observation from the last acquired positive detection. Optionally, both pipelines can perform differently based on the use-case assumptions and specific

analysis choices: simulate and analyse data with nominal or integral sensitivity; compute the EBL absorption (Section 4.6.2) of an unabsorbed source; reduce the source intrinsic intensity by a given factor; compute IRF degradation and perform the analysis accounting for the worsen sensitivity; add an exponential cut-off to the power-law model; sort source candidates based on their significance instead of their counts excess. All inputs are summarised in Table 5.1. Additionally, most scripts (pipelines and utilities) also require a configuration xml file accounting for absolute paths and the list of source and background free parameter. An example is shown in Appendix B.1.

Version	Observation	Analysis	Choices
all	CALDB	trials	IRF degradation
	IRF	-	-
	pointing (deg)	-	-
	ROI (deg)	-	-
	ΔE (TeV)	-	-
	t_{exp} (s)	-	-
	dof	-	-
follow-up	t_{delay} (s)	σ_{blind} threshold	sGRB template
	t_{total} (s)	sky map pixel size (deg)	apply EBL
	t_{run} (s)	sky map axes size (pixels)	EBL table
	t_{add} (s)	smoothing corr. kernel rad. (deg)	add Exp. cut-off
	-	N_{max} candidates	scale src intensity
	-	$\sigma_{detection}$ threshold	sort candidates by TS
blind-search	Δt (s)	σ_{blind} threshold	sGRB template
	-	sky map pixel size (deg)	apply EBL
	-	sky map axes size (pixels)	EBL table
	-	smoothing corr. kernel rad. (deg)	add Exp. cut-off
	-	N_{max} candidates	scale src intensity
	-	$\sigma_{detection}$ threshold	sort candidates by TS
wilks	Δt (s)	-	src model
	-	-	bkg model

Table 5.1: This is a summary of all inputs required by the pipelines. The *Pipeline* entry specifies the pipeline that a specific input belongs to. *Observation* inputs (integer or float, except for calibration inputs) are all those describing the observation: the calibration database (CALDB) and IRF used for simulating the photon lists, pointing direction of the telescopes and region of interest (ROI), exposure time(t_{exp}) and energy interval (ΔE). The total observing time (t_{tot}) and run duration (t_{run}), the delay time (t_{delay}) and the additional data in-take time after the last positive detection (t_{add}) belong to the follow-up pipeline only. Time intervals (Δt) are required by the statistical pipelines instead. The *Choices* entry lists available options (either Boolean or file). The user can choose if the EBL absorption requires computation (apply EBL) before data simulation and from which EBL model (i.e. Gilmore et al. 2012) to draw the optical thickness values (EBL table); if the analysis should be computed with exponentially cut-off power law models (add Exp. cut-off) instead of simple power laws. In order to gain a sample of source brightness with a single template, one can decide if the intrinsic intensity of the source should be decreased or increased with respect to its nominal value (scale src intensity). Another key option is to degrade the IRF to obtain a sensitivity similar to what is expected from RTA (IRF degradation). The source template (sGRB template) for the simulation of the source is also a user choice (Section 4.6.3). Count excesses may be arbitrarily ordered by their best fit significance rather than their count rate (sort candidates by TS), for higher reliability in identifying the source. The *Analysis* entry refers to the setup of the pipeline (either integer or float). The code can be executed for a number of trials (trials), namely the number of independent realisation of the event to simulate and analyse. Acceptance thresholds are required both for the peak-search algorithm detection of candidate sources (σ_{blind}) and the identification of positive ($>5\sigma$ post-fit) detections ($\sigma_{detection}$). Sky maps axes size, pixel size and smoothing correlation kernel radius (smoothing corr. kernel rad.) are required inputs for running the blind-search of the source and can impact either on computation time (pixel size $<< 0.02^{\circ}$) or the localisation precision (pixel size ($>> 0.02^{\circ}$). The analysis can be carried out for a number of candidate sources, if a maximum number higher than one is given (N_{max}).

Outputs of the pipelines are: sky maps (tables and images) and DS9 regions, first guess models and best fit models, tables of stored parameter values and computed physical quantities. Specific outputs of the statistical analysis pipeline are: distributions and confidence regions and/or intervals in the considered parameters' space. Tables of stored parameter values include: simulation ID, time interval

(s), number of detected candidates, source first guess coordinates (°), number of positive detections, source best fit coordinates, source integral photon flux (ph/cm^2/s) and test statistic value ($\approx \sigma^2$). Concerning the follow-up code, outputs are: light-curves. Tables of stored parameter values contain: time frame ID, time interval (s), number of detected candidates, source first guess coordinates (°), number of positive detections, source best fit coordinates, source integral photon flux(ph/cm^2/s) and relative statistical uncertainty, test statistic value. All outputs are summarised in Table 5.2.

Output	all	follow-up	blind-search	Wilks
data tables	-	Δt (s)	t_{exp}	t_{exp}
	-	N^{src}_{blind}	N^{src}_{blind}	-
	RA (deg)	$N^{src}_{detection}$	$N^{src}_{detection}$	-
	DEC (deg)	Flux (ph/cm^2/s)	Flux (ph/cm^2/s)	-
	TS (σ^2)	Flux errs (ph/cm^2/s)	-	-
other	src model	sky maps	sky maps	-
	bkg model	candidate regions	candidate regions	-
	src & bkg models	flux points	-	-
	-	upper limits	-	-
post-processing	-	complete light-curve	distributions	distributions
	-	-	confidence regions	p-values

Table 5.2: Pipeline products are grouped as data tables or other output types (i.e. sky maps, regions, models) through *Output* entry. As for the inputs table, to which pipeline a specific output belongs is determined by the entries: *Both*, *Follow − up* or *Statistical*. Data tables contain the number of count excess detected by the peak-search algorithm and their fraction resulting in positive detection, source coordinates (RA/DEC) and an integrated flux estimate alongside the detection significance, the time interval or the exposure time. All pipelines produce sky maps, regions and model files. In post-processing, the follow-up analysis delivers light-curves, while from the other pipelines one can obtain parameter distributions and confidence regions.

Except for a few inputs that were varied throughout the various tests, this study was executed with a fixed setup. The reason behind this choice laid in minimising the variables that may impact on the performances, in order to unambiguously study the parameter space. From here onward, therefore, as general setup of the pipeline the values presented in Table B.1 from AppendixB) will be implied, in agreement with the use-case assumptions (Section 4.6) and the template's choice (Section 4.6.3). The reader should keep in mind that the setup presented in this work may not correspond to RTA final strategy. This study is a preliminary investigation of a still unexplored parameter space.

5.2.2 Afterglow simulations

Independent realisations of the afterglow were generated with `ctobssim` using the template described in Section 4.6. Each Δt segment of the burst was generated singularly. To optimise the computation time and work with data similar to real photon lists, all segments of the observation were merged (Section 5.3) in photon lists of length t_{run} = 1200 s. Events were simulated under nominal and degraded sensitivity condition (Section 3.6), using the `South_z40_0.5h` instrument response function from `prod3b-v2` calibration database. The simulated FoV was centred on the centroid of the localisation probability map (Section 4.6.3 and with a radius of 5°. As a result, the burst true position appears with an off-axis (in both coordinates) of about 1.5 degrees approximately. The use of the full-array in parallel pointing mode will be implicitly considered hereinafter, with $r_{FoV} = 5\,deg$. Furthermore, the aforementioned assumptions on the alert reception time and the array slewing time are made (total t_{delay} =30,50). Although not an overly conservative choice the assumptions remain within reasons since the worst case scenario for LST are required to be t_{slew} <50 s ($t_{slew} < 90$ s for the full array)[4] at the time of writing. Simulations were performed both at nominal and degraded sensitivity in order to compare RTA perspectives on blind detections versus full sensitivity analysis. More details on the MC simulations can be found in Appendix B.3.

[4]CTA Science Performance Requirements: `https://www.cta-observatory.org/science/cta-performance/`

5.3 Code utilities

The code[5] developed for this thesis project is publicly available on GitHub[6]. It comprises of Python files containing all classes and functions (`pkg_blindsearch.py`, `module_plot.py` and `module_statistics.py`), pipelines (`RTAblind.py` and `RTAbkg.py` for to the statistical analysis pipeline, `RTAlightcurve.py` for the follow-up analysis pipeline), and other scripts (`irf_degradation.py`, `templates.py` and `sensitivity.py`). The pipelines have already been outlined in Section 5.2, hence the following will focus on utilities and side scripts descriptions.

5.3.1 class Analysis()

The class is defined in `pkg_blindsearch.py` Python file and handles the analysis procedures for the pipelines. The setup can be accordingly tuned via user accessible public fields, namely keywords that are accessible from the environment outside the class and that can be used to modify the class' attributes (i.e. the energy range, time interval, etc.). A handful of its methods simply invoke `Gammalib` and `ctools` software package utilities (see Section 5.1) but most are natively implemented. A brief introduction of the main functionality of the class is hereinafter presented, with references to the most important methods grouped by their purpose:

***i)* Producing user defined spectral models.** From the template FITS table (see Section 4.6.3) the user defined spectral models necessary for the source simulation are computed, and the source models generated. This is achieved by invoking `loadTemplate()`. This method accesses the template data and generates the required source models (of the user defined type). It makes use of already generated spectra tables, with energy (MeV) and intensity (ph/cm^2/s/MeV) columns, though if required by the pipeline setup it automatically invokes the computation of new ones (`__extractSpec()`). When computing spectra tables, users have the choice to normalise the intrinsic spectra of the source, i.e. to sample a range of brighter and/or fainter gamma-ray bursts (`makeFainter()`). Note that since the standard use of this method is rendering a source fainter than its nominal value, to generate brighter spectra the normalisation factor should be within 0 and 1.

***ii)* Implementing EBL absorption.** The class provides a sequence of methods which add an EBL absorption to unabsorbed source templates. The EBL model is user defined (default is Gilmore [23] fiducial EBL model) and the EBL absorption is implemented as an exponential attenuation of the spectral intensity (see Section 4.6.2) due to optical thickness. The method which computes the attenuation and generates the resulting FITS table is `fitsEbl()`. It invokes `__zfetch()` if the pipeline requires the determination of the redshift value nearest to the source's among those available in the τ table. It requires the source redshift to be known, either declared within the template itself or initialised in the pipeline setup. Through `__addEbl()` method the new EBL absorbed template is then created.

***iii)* Degrading the Instrument Response Function.** To emulate a worsen sensitivity for the real-time analysis, it is necessary to degrade the IRF (see Section 3.6 for degradation details). The procedure is computed by invoking `degradeIrf()`, which can either degrade the background counts only, the effective area only with subsequent background counts re-calibration, or both. The effective area degradation is coded in `__degrAeff()` method, while background counts degradation (either as consequence of the effective area degradation or background counts degradation proper) in `__degrBkg()`. The default choice is to degrade the effective area only. Depending on the user permissions in the calibration database folder, the code my automatically require the root password to modify this files.

Some additional features are: *i)* `photonFluxPowerLaw()` and `photonFluxExpCutOffPowerLaw()` which compute the integral photon flux within a given energy range, for a simple power law and an exponentially cut off power law respectively; *ii)* `totalDelay()` class method, which draws a random total delay ($t_{delay} = t_{alert} + t_{slew}$) time from a given distribution (uniform, normal, Poisson) within a given

[5] GitHub repository: `https://github.com/ambra-dipiano/thesis`
[6] GitHub is a Microsoft subsidiary providing hosting for software development version control using Git.

range of values; *iii)* `appendBkg()`, `appendEventsSinglePhList()` and `appendEventsMultiPhLists()` which allow to append background events to a source-only photon lists, append multiple observations into a single photon-list or append events from a long observation (or many) in multiple photon lists each of a given duration.

The `ctools` software package scripting is encoded within this class, two Python modules (`ctools` and `cscripts`) that allow using all tools and scripts as Python classes. The `gammalib` module is required as well. Each tool is initialised by invoking the respective Python class and via class `Analysis()` public field the user can adjust the setup of each tool parameters from the RTA pipeline. Recalling Section 5.1, here are the specific tools setup as used in this work:

• `ctobssim:` the source model is given by the template spectra in each energy bin (Listing 5.2) while the background model is taken from the template contained within CTA Instrument Response Functions (Listing 5.4). The calibration database in use is the latest available, `prod3b-v2`, and the IRF is `South\_z40\_0.5h` (nominal or degraded). From Listing 5.5 the pipeline retrieves the sky coordinates of the centroid of the probability map provided by the alert, which are used as pointing coordinates. The field of view is fixed at 5° of radius and the energy range is between 30 GeV and 150 TeV. The time interval of each simulation correspond to that of the template. With natively implemented functions (see Appendix 5.2.2) these photon lists are manipulated in order to obtain data of given duration (i.e. 1200 s) that can be treated as one would real observations. The seed of the MC simulation is iteratively increased in order to obtain independent realisations of the same event.

• `ctselect:` observations are selected in time in order to simulate the incoming batch of data of given exposure time (i.e. 1, 5, 10 and 100 s). The field of view and energy range are maintained as the above, and so are the pointing coordinates.

• `ctskymap:` from each selection a sky map is generated. This is performed by integrating in energy and time, maintaining the same parameters setup as the above. The pixel size of the count map is fixed to 0.02° and the pixel number of each axis of the map is automatically set to $R_{FOV} * 2/d_{pix}$, where R_{FOV} is the field of view radius and d_{pix} the size of one pixel. The background subtraction method selected is that of deconvolution with the IRF, namely `South\_z40\_0.5h` (nominal or degraded) from `prod3b-v2`. The image centre of reference is, once again, passed as the pointing coordinates.

• `cssrcdetect:` the peak-search algorithm that performs the transient blind-search is executed with a sky map in input. A Gaussian smoothing is applied with correlation kernel radius of 0.1°. Candidates (from 1 to 5 at maximum) are searched over the full field of view (except for a priori excluded regions) with Gaussian acceptance threshold of 5σ. The source spectral model is given as in Listing 5.3 and the source spatial model is given as Listing 5.1. Additionally, a background model is appended as well (Listing 5.4).

• `ctlike:` after some manipulation of the models of the candidate sources (Section 5.3.2), the full-FoV maximum likelihood analysis is performed on the selected events. Free parameters for a one degree of freedom analysis are the background spectral index and intensity, as well as the source intensity (for dof=3 analysis the source coordinates are both set free). The calibration database used is `prod3b-v2` and the IRF is `South\_z40\_0.5h` (nominal or degraded). A Test Statistic is required.

• `cssens:` worthy of mentioned although not included in the RTA pipeline, is the tool allowing for the sensitivity computation. A selection of events is given in input, alongside the source and background models. The calibration database is `prod3b-v2` and the IRF is `South\_z40\_0.5h` (nominal or degraded). Within a given energy range (30 GeV - 150 TeV) the differential or integral sensitivity are computed for a given number of energy bins or energy thresholds, respectively. For this work, the integral sensitivity was computed for one energy interval within the given energy range, and for twenty. In order to compare CTA nominal and degraded sensitivity with the currently operating IACTs, the sensitivity computation was also performed within H.E.S.S., MAGIC and VERITAS energy ranges (Appendix A).

5.3.2 class ManageXml()

The class is defined in `pkg_blindsearch.py` Python file and contains a handful of methods created with the goal to modify xml files or access the information therein contain. A brief description of the most important methods is presented in the following order: *i)* accessing xml information and parameter attributes; *ii)* halving the spectral intensity of subsequently detected candidate sources; *iii)*

sorting of the candidates' list by their significance.

***i)* Accessing parameter values.** A series of recursive methods allow to access parameter values (such as right ascension, declination, spectral index, spectral intensity or test statistic and relative statistical errors) of all candidates and/or a specific one. Some of them are the following: `loadTs()` which access the candidate significance, `loadRaDec()` to access its coordinates and `loadSpectral()` and `loadPrefErr()` for accessing its spectrum parameter values and the source intensity statistical uncertainty. By default, the class access the values for the first candidate in the observation list. Alternatively, the highest TS candidate can be selected instead.

***ii)* Decreasing spectral intensities.** Since the analysis can be carried out on a sample of candidates identified by the peak-search algorithm, a more realistic scenario would require a decreasing spectral intensity for each subsequent excess listed instead of all candidates having the same arbitrarily assumed spectral intensity. The `modXml()` method was implemented in order to halve the spectral intensity of the source model for each subsequent candidate, with respect to the previous one. The first count excess will be described by a simple power law model such as Listing 5.3, the following with feature progressively halved intensity values.

***iii)* Sorting candidates by their significance.** An optional feature (`sortSrcTs()`) is to sort the candidates by their test statistic value, from highest to lowest. This reduces the chances of assuming background fluctuation or spurious contaminating events as astrophysical objects. If the candidates' list is kept to a reasonable size (about 5) the computation time is not heavily effected for short exposure times (about 1.5-6.5 s of computation time for the maximum likelihood fit). Outputs from the pipeline are saved, by default, for the assumed source only.

Among others, are also the following features: *i)* `setTsTrue()` method which sets source models to require a TS computation from the analysis; *ii)* `prmsFreeFix()` which fixes and frees parameters for the maximum likelihood fit, with a number of degrees of freedom as required by the configuration file (Appendix B.1).

5.3.3 Miscellaneous

The `pkg_blindsearch.py` Python file contains some more utilities, among which are the `ConfigureXml()` class and a handful of functions. The former handles all required paths (also creating the necessary folders if missing), the latter contains utilities such as: *i)* `getDof()` which given a configuration file returns the number of degrees of freedom (i.e. number of free parameters); *ii)* `getTrueCoords()` returning the source position as given by an observation or a template file; *iii)* `getPointingAlert()` which returns the telescope pointing (Listing 5.5) with either a randomised off-axis angle added to the source true position or as the centroid of a given localisation probability map (i.e. from external alert such as this work's scenario); *iv)* `checkTrialId()` that, if an output table file exists, skips the already computed trials.

5.3.4 Side scripts

A handful of side scripts are available in the repository[7]. They were developed for secondary needs, from plotting purposes to post-processing data manipulation.

`modul_plot.py` comprises of pre-defined plotting functions which allow for in-analysis images production as well as post-processing data display. Some of the utilities therein contained allow to produce count map, spatial residual map and TS map images from existing FITS tables. Spectra and light-curve plotting functions are also included, as well as utilities for the 3-dimensional display of an IRF effective area and background rates (either nominal, degraded or the comparison of both).

`module_statistics.py` contains functions for the post-processing data analysis. Data can be visualised in histograms and their distributions can be fitted with theoretical ones. It also includes

[7] https://github.com/ambra-dipiano/thesis

```
...
import healpy as hp
...
# retrieve telescope pointing coordinates from alert probability map ---!
def getPointingAlert(merge_map=None):
  # load map ---!
  map = hp.read_map(merge_map)
  pixels = len(map)
  axis = hp.npix2nside(pixels)
  # search max prob coords ---!
  pmax = np.argmax(map)
  theta, phi = hp.pix2ang(axis, pmax)
  pointing = (np.rad2deg(phi), np.rad2deg(0.5 * np.pi - theta))
  return pointing
```

Listing 5.5: The function makes use of healpy Python library to load a BNS merger localisation probability map from a GW alert ($merge_{map}$). The coordinates corresponding to the highest probability ($pmax$) of the event position are returned as pointing coordinates for the array.

functions for confidence regions and confidence interval determination, as well as parameter space 2-dimensional map display. A few example of those will be presented in Chapter 6.

```
...
# energy ranges
if erange == 'fullsys':
    LST = (min(en, key=lambda x:abs(x-20)), min(en, key=lambda x:abs(x-150)))
    MST = (min(en, key=lambda x:abs(x-150)), min(en, key=lambda x:abs(x-5000)))
    SST = (min(en, key=lambda x:abs(x-5000)), min(en, key=lambda x:abs(x-300000)))
else:
    LST = (min(en, key=lambda x:abs(x-20)), min(en, key=lambda x:abs(x-3000)))
    MST = (min(en, key=lambda x:abs(x-80)), min(en, key=lambda x:abs(x-50000)))
    SST = (min(en, key=lambda x:abs(x-1000)), min(en, key=lambda x:abs(x-300000)))
CTA = (min(en, key=lambda x:abs(x-30)), min(en, key=lambda x:abs(x-150000)))
...
```

Listing 5.6: Snippet of the energy range selection code. The energies are contained in a numpy (Python library) array, en, and are expressed in GeV. LST, MST, SST and CTA full-array energy ranges (both required and full-system sensitivity provision) are accounted for.

`templates.py` script accesses data from a template for gamma-ray burst afterglow emission. The script plots spectra for a sample of time bins (Section 4.6.3) both EBL unabsorbed and absorbed. It also computes the integral photon flux over given energy ranges (i.e. LST, MST, SST and CTA full-array as shown in Listing 5.6) and graphs the resulting lightcurves, comparing the absorbed integral photon flux with the unabsorbed one. An example is Figure 4.8(b) wherein the attenuation due to EBL absorption is heavily reducing the integral photon flux at all times for the SST range lightcurve, contrary to the full-array energy range light-curve whose integral flux is dominated by the unabsorbed low-energy radiation (up to few hundreds of GeV).

`degradation.py` (Listing 5.7) has the use of creating a degraded copy of a whole calibration database, stored in the same location of the original one. By default, the name of the degraded calibration database would be similar to that of the nominal one, substituting the prefix "prod" with "degr" but maintaining the same version suffix for coherence purposes. The script degrades all IRFs therein contained by a given factor (either by their effective area, their background counts or both) and updates the calibration database index. Notice that only the calibration database name will be changed, while the IRFs will preserve their original label (i.e. the degraded copy of Shouth_z40_0.5h from prod3b-v2 will be South_z40_0.5h from degr3b-v2).

`sensitivity.py` computes the nominal and degraded sensitivity for a given source (see Section 3.2 for `ctools` sensitivity computation) for a number of energy bins. The sensitivity can be either differential or integral. The output of the scripts are sensitivity tables (Section 5.1) and plots such as

```
from pkg_blindsearch import Analysis
import os

# IRFs files ---!
caldb = 'prod3b-v2'
irf = os.listdir(os.environ.get('CTOOLS') + \
      '/share/caldb/data/cta/' + caldb + '/bcf/')

# degrade ---!
for fits in irf:
  irfObj = Analysis()
  irfObj.irf = fits
  irfObj.caldb = caldb
  irfObj.degradeIrf()

print('%s degradation completed.' %caldb)
```

Listing 5.7: The script creates a degraded copy of an entire calibration database (i.e. prod3b-v2). The output will have the same version suffix of the original one, while the prefix "prod" will be substituted with "degr" (i.e. degr3b-v2).

Figure 3.5, making use of `module_plot.py` functions.

Lastly, `wilks.py` allows to compute the Wilks' theorem verification from a sample of empty-fields analysis. The script performs TS distributions and derives the p-values for respective significance thresholds. Plots for probability and cumulative distribution functions are also generated (Figure 6.3).

5.4 Post-processing analysis tools

The post-processing manipulation of data is of critical importance when the parameter space is as wide as the one at hand and its optimisation still largely unexplored. After simulating and analysing through maximum likelihood fit samples of $10^4 - 10^6$ independent realisation of the same event, free parameter distributions must be studied in order to find the statistical uncertainty of the pipeline. In the following, the theoretical tool required by the post-processing data manipulation will be presented.

5.4.1 Vincenty's Formulae

The quality and accuracy of the source localisation have been analysed, for the purpose of this work, both as the module between a single detected coordinate and its true value and the great-circle distance ($\Delta\Theta$) of the candidate source position from the true position of the gamma-ray burst. $\Delta\Theta$ is the shortest distance between two points placed over a spherical surface, measured along the surface itself. In spaces with curvatures different from zero, straight lines are replaced by geodesics and great-circles are geodesics whose centres are coincident with the sphere's centre.

Let P and Q be two distinct point on a spherical surface and $\Delta\Theta$ be the central angle between them, then its value is given by the spherical law of cosines if one of the poles is used as third auxiliary point.

$$\Delta\Theta = arccos(sin\phi_P sin\phi_Q + cos\phi_P cos\phi_Q cos(\Delta\lambda)) \tag{5.5}$$

where ϕ_i, λ_i are the points' coordinates in radians. The problem of using this equation with numerical computation is that there might be poor handling of floating-point precision. Among the most numerically stable formulas the following has been chosen to guarantee numerical stability at all distances and locations (for in-depth derivation of the formula please refer to [11][12]):

$$\Delta\Theta = arctan\frac{\sqrt{(cos\phi_Q sin(\Delta\lambda)^2 + (cos\phi_P cons\phi_Q - sin\phi_P cos\phi_Q cos(\Delta\lambda)^2}}{sin\phi_P sin\phi_Q + cos\phi_P cos\phi_Q cos(\Delta\lambda)} \tag{5.6}$$

From here onward spherical distances will always refer to Equation 5.6, with values in units of degrees.

5.4.2 Rayleigh Distribution

Since the spherical distance between the candidate position and the source's true coordinates is a function of two independent random variables normally distributed (as it will be shown in Section 6.2) it is useful to briefly introduce the *Rayleigh Distribution*[13],[21]. The *Rayleigh* distribution describes the continuous probability distribution for non-negative valued random variables. As derived in [14] this distribution also describes a sample $z = f(x, y)$ when x, y are independent random variables normally distributed ($x \sim G(\mu_1, \sigma_1)$, $y \sim G(\mu_2, \sigma_2)$) and $z \geq 0$.

A random variable z is said to have the Rayleigh distribution with scale parameter γ if its probability density function (PDF) is given by:

$$p(z) = \begin{cases} \frac{1}{\gamma} e^{-\frac{z}{\gamma}}, & \text{if } z \geq 0 \\ 0, & \text{otherwise} \end{cases} \tag{5.7}$$

and cumulative distribution function, $Pr(Z \leq z)$:

$$Pr(z) = \frac{1}{\gamma} \int_0^z e^{-\frac{x}{\gamma}} dx = 1 - e^{-\frac{z}{\gamma}} \tag{5.8}$$

The *100q percentile* (ξ_q), with $0 \leq q \leq 1$, is defined by the equation:

$$P(\xi_q) = q \tag{5.9}$$

$$\xi_q = -\gamma ln(1 - q) \tag{5.10}$$

in particular, the *median* is:

$$\xi_{0.5} = \gamma \ln 2 \tag{5.11}$$

The peak of the distribution is easily found in relation to its scale parameter γ as

$$f_{max} = f(\gamma; \gamma) = \frac{1}{\gamma} e^{-\frac{1}{2}} \approx \frac{0.606}{\gamma} \tag{5.12}$$

with

$$\sqrt{\hat{\gamma^2}} \approx \sqrt{\frac{1}{2n} \sum_{i=1}^{N} z_i^2} \tag{5.13}$$

a biased maximum likelihood estimator which can be corrected as derived in [22] but is sufficient for the scope of this work. The Rayleigh distribution is completely specified when the parameter γ is known. If $Z = z_1, z_2, ..., z_N$ is a sample of N independent observations from a Rayleigh distribution, the joint probability density of Z as a function of γ is given by:

$$L(\gamma) = \frac{1}{\gamma^N} e^{-\frac{\sum z_i}{\gamma}} = \frac{1}{N} e^{-\frac{Nc}{\gamma}} \tag{5.14}$$

where

$$c = \frac{1}{N} \sum_{i=1}^{N} z_i \tag{5.15}$$

with c being a sufficient, *unbiased* estimator. If such a thing does exist one can also automatically derive the maximum likelihood estimate.

The variance of c is:

$$var\, c = \frac{\gamma^2}{N} \tag{5.16}$$

Moreover, since $2z_i/\gamma$ is a χ^2 variate with 2 degrees of freedom and $z_1, ..., z_n$ are independent, then

$$\frac{2Nc}{\gamma} = \frac{2\sum_{i=1}^{N} z_i}{\gamma} \tag{5.17}$$

is also a χ^2 variate with $2N$ degrees of freedom. Thus the distribution c is given by the following equation:

$$dP(c) = \begin{cases} \frac{N^N}{\gamma^N \Gamma(N)} e^{-\frac{Nc}{\gamma}} c^{N-1} dc, \text{if} c \geq 0 \\ 0, \text{otherwise} \end{cases} \tag{5.18}$$

5.4.3 Confidence interval estimation

Since the distance between the detected position of the candidate source and its actual coordinates is non-negative by definition, and is moreover a function of two independent Gaussian distributed random variables, the statistical circular error regions can be derived from a Rayleigh distribution. In order to establish confidence limits with a coefficient $1-\alpha$, on must determine from χ^2 tables two numbers (χ_1^2, χ_2^2) such that:

$$Pr(\chi^2 \leq \chi_1^2) = \alpha/2 \tag{5.19}$$

$$Pr(\chi^2 \leq \chi_2^2) = 1 - \alpha/2 \tag{5.20}$$

then, if c is defined as in Equation 5.15

$$\chi_1^2 \leq \frac{2Nc}{\gamma} \leq \chi_2^2 \tag{5.21}$$

with N degrees of freedom and probability $1-\alpha$. Therefore

$$\frac{2Nc}{\chi_2^2} \leq \gamma \leq \frac{2Nc}{\chi_1^2} \tag{5.22}$$

will be $100(1-\alpha)$ percent confidence limits for γ. In Table 5.3 some values for the probability threshold q and relative values of z_c are reported. These values are plotted over a *Rayleigh* distribution PDF and CDF in Figure 5.2.

confidence levels

q	0.6827	0.9545	0.9973	0.99994
$z_c(RA)$	1.52	2.49	3.44	4.41
$z_c(G)$	$\pm 1\sigma$	$\pm 2\sigma$	$\pm 3\sigma$	$\pm 5\sigma$

Table 5.3: The table records z_c values for each q probability confinement threshold. The properties of the distributions are: location parameter at zero for both cases, scale parameter $\gamma = 1$ and $\sigma = 1$ for the Rayleigh and Gaussian distribution respectively. Values are given in unit of degrees. Sample size is of 1e6.

In this work z_c values have been calculated for each of the confidence levels in Table 5.3 in order to draw circular confidence region centred on the samples' mean and of radius $r = z_c(\gamma)$.

Alternatively an elliptical error region for the coordinates can be derived from the parameters' covariance, wherein each axes of the ellipse contains the $1-\alpha$ probability. The equation for the containment region thus becomes:

$$\left(\frac{x}{\sigma_x}\right)^2 + \left(\frac{y}{\sigma_y}\right)^2 = s \tag{5.23}$$

where s determines the scale of the ellipse, hence must equal the χ^2 value for any given probability value and N degrees of freedom, i.e. if $N = 2$ and $q = 0.95$ then:

$$P(s < 5.991) = 1 - 0.05 = 0.95 \tag{5.24}$$

resulting in a confidence region such as:

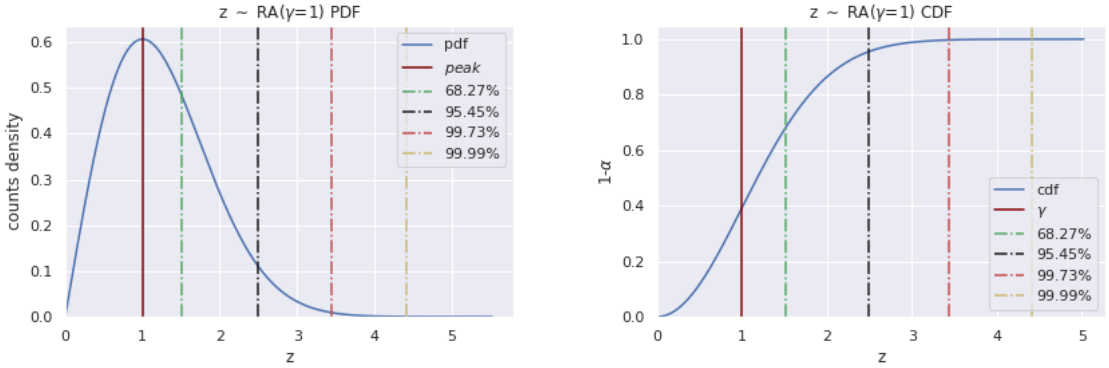

(a) Rayleigh probability distribution function.

(b) Rayleigh cumulative distribution function.

Figure 5.2: Confidence thresholds for a *Rayleigh* distribution of scale parameter $\gamma = 1$.

$$\left(\frac{x}{\sigma_x}\right)^2 + \left(\frac{y}{\sigma_y}\right)^2 = 5.991 \tag{5.25}$$

From this, one can draw confidence regions relative to a specific set of confidence levels, i.e. $\sigma = 1, 2, 3, 5$ as done in this work. If needed, the tilting of the ellipses can be computed from the covariance matrix.

Chapter 6

Results

In this chapter results from the statistical analysis performed with the RTA prototype pipeline will be presented, as well as mocked RTA follow-up analysis of a short GRB afterglow event. In Section 6.1 the verification of Wilks' theorem and the p-values determination will be summarised for the implemented full field of view maximum likelihood analysis. In Section 6.2 the peak-search algorithm efficiency and precision will be constrained for a number of exposure times and use-case assumptions (i.e. EBL, sensitivity) in order to set a lower limit on the required minimum integration time for a blind-search. In Section 6.3 the detection significance and the integral flux estimation will be investigated, alongside the selection of a minimum exposure time required by the analysis for positive detection (here defined as a blind-detection with maximum likelihood significance equal or larger than 5σ). Finally, Section 6.4 and Section 6.5 will summarise an extensive study on the follow-up performances via RTA of a short GRB afterglow, at different time delays (comprising the latency of the incoming alert and the telescope slewing time) and intrinsic source brightness. It will be shown how similar events to those detected by MAGIC [40] [42] and H.E.S.S. [41] could be well within the RTA observing capability.

Before presenting the results it might be useful to remind the use-case assumptions, the simulation parameters and the follow-up observation setup. Tests were run under the assumption of an external alert for a short GRB (Section 4.6) follow-up, received with localisation uncertainty comparable to the field of view of CTA. The scenario relates either to satellites' alerts (i.e. Fermi-GBM) or future prospects on GW alerts once third-generation interferometers will be available (i.e. KAGRA, ET). The observation can thus be carried out without accounting for tiling strategies [3] [64] [1] and requires one pointing only to cover the alerted region. A full array configuration was considered (`South_z40_0.5h` instrument response function from `prod3b-v2` calibration database). Nominal and degraded sensitivity were both accounted for, with a required *not worse than a factor of two* degradation (Section 3.6). The main goal was to perform a ***blind-search*** of the alerted transient and a follow-up with full field-of-view maximum likelihood analysis at short timescales. Products of the analysis are detection coordinates, flux estimation and significance of the detection alongside relative errors. Preliminary tests (Section 6.2) were run with and without EBL spectral absorption (Section 4.6.2), while the core section of the study accounts for EBL absorbed sources only. A summary of the specific setup for each test phase can be found in Table 6.1 while the general setup for the pipeline is presented in Table B.1 of Appendix B. The goal was to constrain: *i)* the pipeline efficiency in blind-search detection; *ii)* the localisation precision; *iii)* the significance estimation using full-field of view maximum likelihood fit;

iv) and verify a short-timescale follow-up feasibility with already existing scientific tools (Section 5.1). In Figure 6.1, snapshots at all considered exposure times of the count maps injected into the peak-search algorithm during RTA (Section 5.2) are show. The sample size is given in number of trials (independet realisation). The overlaid regions identify the count excess that is assumed being the source.

test phase	EBL	IRF	t_{delay} (s)	Δt (bin)	R_{FoV} (deg)	E (TeV)	dof	sample	candidate
empty fields	-	N	0	1,5,10,100	5	0.03-150	1, 3	10^6	first
preliminary	no/yes	N, D	30	1,5,10,100	5	0.03-150	1	10^4	first
intermediate	yes	N, D	30	5,10,100	5	0.03-150	1	10^4	highest σ
final	yes	N, D	50	10,100	5	0.03-150	1	10^4	highest σ
light-curves	yes	N, D	30/50	10,100	5	0.03-150	1	1	highest σ

Table 6.1: Summary of the test phases and their main setup. EBL entry indicates spectral absorption, IRF specifies if the analysis was carried out with nominal (N) or degraded (D) instrument response function. The sample size is given in number of trials (independent realisation of the same event), while t_{delay} clarifies the starting time of the observation while Δt accounts for the exposure time considered in the analysis ROI and energy range parameters are maintained at fixed value. The candidate selection can be either the first one identified by the blind-search (first) or the post-fit highest significance one.

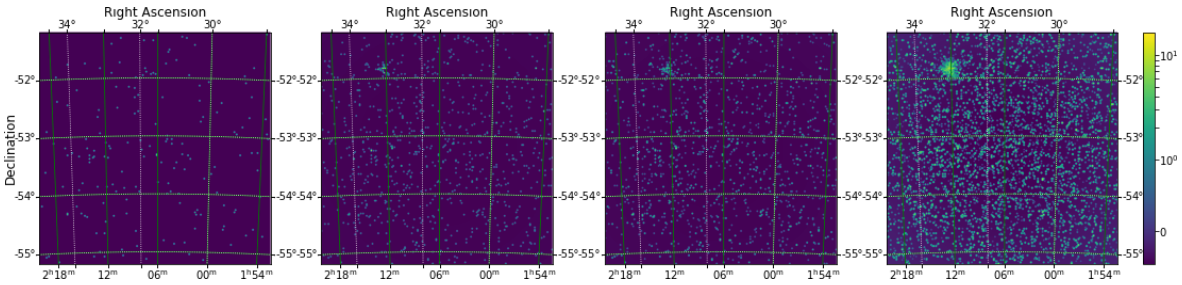

Figure 6.1: Sky maps for 1, 5, 10, 100 s exposure time (from left to right). Axes are in Galactic latitude and longitude, as well as right ascension and declination. The peak-search algorithm is required to localise the count excess with acceptance threshold of at least 5σ. The maps were produced with `ctskymap` tool, using 0.02° pixel size.

6.1 Verification of Wilks' theorem and p-values determination

Wilks' theorem verification is critical to evaluate how the pipeline performs and the science tools feasibility for the considered analysis. Moreover, it is also necessary to evaluate detection significance by means of the relation between Test Statistic values, p-values and, i.e., Gaussian sigma. In `ctools` documentation it is reported that the TS of the full field of view maximum likelihood equals σ^2 in first approximation, for analysis with one degree of freedom (dof). If Wilks' theorem [4] is verified, one can compute the p-values of given TS thresholds and therefore derive the corresponding Gaussian significance (Section 3.5). As in [24], empty fields were simulated over a 10^6 trials sample for t_{exp} of 1, 5, 10, 100 s. A full field of view maximum likelihood analysis, with 1 and 3 degrees of freedom, was executed assuming the presence of a Crab-like source. The resulting TS distributions were compared to a $\chi^2_N/2$, with $N = 1, 3$ degrees of freedom. A factor of 2 comes into play when considering a minimum flux that cannot be negative [25] and thus half of the data can either be excluded or arbitrarily equalled to zero. Tests validated the analysis carried out with the previously described setup (Section 5.1 and Section 5.2.1) for dof=1 at all considered exposure times (an example for $t_{exp} = 100$ s is given in Figure6.2 with dof=1 (a) and dof=3 (b), see Appendix C for more), allowing to relate to a Gaussian significance for a given TS threshold (i.e. TS$\geq$25) when 1 degree of freedom is considered. Whereas the same analysis performed with 3 degrees of freedom did not reach convergence (TS distributions do not follow a χ^2 distribution at any of the considered exposure times)[1]. The cause might be too large parameter ranges in the source model (Section 5.1). Further testing with stricter ranges (i.e. a

[1]Please note that tests were performed only for short exposure times, hence there is no claim on the behaviour at longer time-scales for more than one degree of freedom.

fraction of degree around the injected coordinates) are thus required in the future. As a consequence of what reported above and the fact that within the RTA context a dof=1 maximum likelihood could suffice, further tests for the pipeline assessment were executed with dof=1 only.

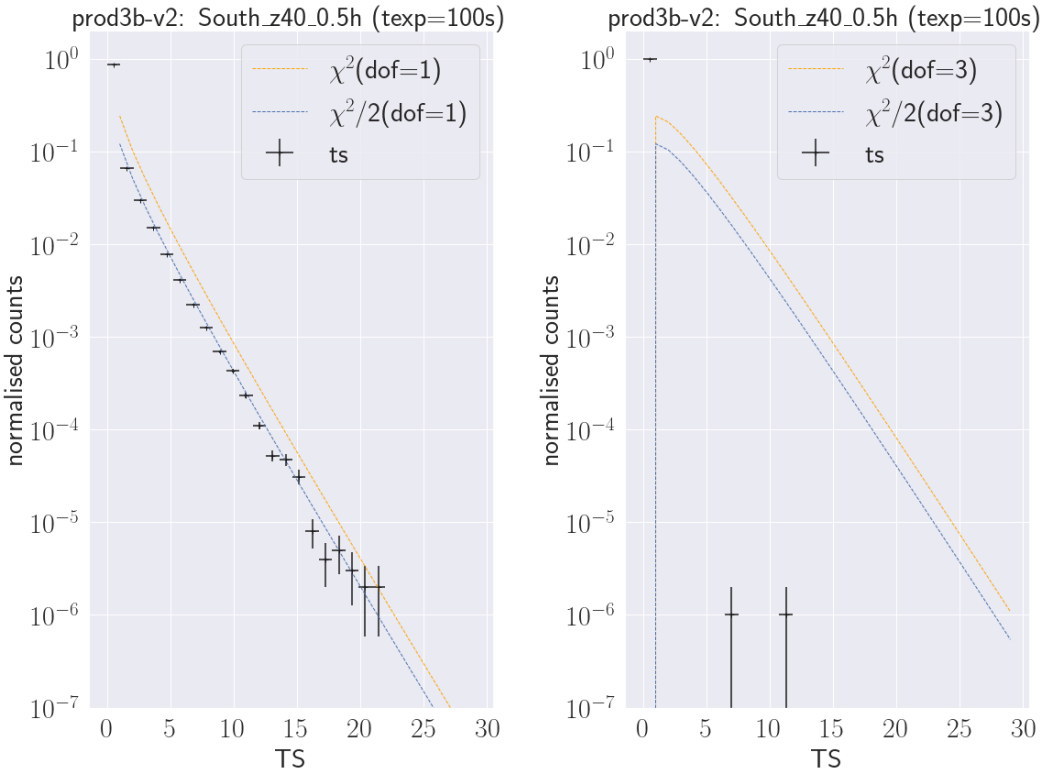

(a) degrees of freedom = 1.

(b) degrees of freedom = 3.

Figure 6.2: The plots show the resulting TS distribution (black dots) from 1e6 empty fields best fit to the source's model template (exposure time t_{exp} = 100 s). Considered degrees of freedom are dof=1 (left) and dof=3 (right). The distribution is compared with a $\chi^2/2$ (blue dashed line) and a χ^2 (orange dashed line). Agreement with Wilks' theorem is found for dof=1 maximum likelihood analysis (left), whilst for dof=3 (right) convergence was not reach.

In statistics there are two types of errors that one can obtain from hypothesis testing: the *false negatives* and the *false positives*. *False negatives*, or type II errors, occur when the hypothesis is rejected though actually true; *false positives*, or type I errors, are those recurring when the hypothesis is accepted but in fact false. From a χ^2 distribution one can compute the probability to obtain a false positive (p-values), namely the probability that a TS$> h$ (h being a given TS threshold) is obtained for detections in an empty field. From the agreement with Wilks's theorem (Section 3.5) for dof=1 maximum likelihood analysis, p-values (Figure 6.3) could be computed as:

$$P(TS \geq h) = \int_h^{\infty} \phi(\hat{h}) d\hat{h} \tag{6.1}$$

where $p = P(TS \geq h)$ represents the probability to obtain a false positive with TS$\geq h$ in an empty field (Figure 6.3). With respect to Equation 3.12, the probability distribution function (ϕ) used for the integration was a $chi^2_n/2$, due to the constraints on the source flux (positively defined) [25].

6.2 Preliminary tests: minimum t_{exp} required for an efficient blind-search

A preliminary phase was designed to test the EBL absorption (Section 4.6.2) natively implemented in the pipeline (Section 5.3) from Gilmore et al. (2012) [23] and the degradation of IRFs. Additionally,

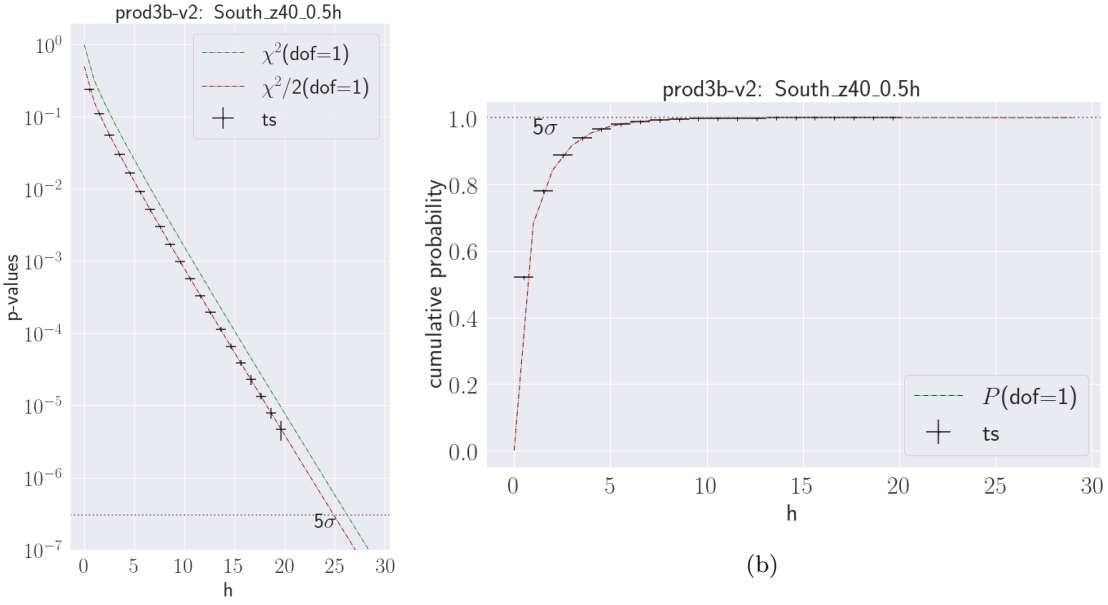

Figure 6.3: **Left** The figure shows the $\chi^2_1/2$ (red dot-dashed line) derived p-values (p) for unit-valued TS thresholds (black crosses), with 100 seconds of exposure time. χ^2_1 is also plotted for comparison (green dot-dashed line). **Right** Here is shown (red dot-dashed line) the cumulative curve (1-p) for the same TS thresholds (black crosses) as the left panel. In both panels the 5σ p-value has been highlighted by an horizontal grey line.

these tests allowed the investigation of the proficiency of the peak search-algorithm[2], available from the `ctools` software package (Section 5.1). Tests were run with CTA nominal sensitivity and, in parallel, accounting for RTA sensitivity degradation in order to constrain the loss in detection efficiency (the Gaussian acceptance threshold was set to 5σ) and localisation precision ($\Delta\theta < 0.5°, 0.2°, 0.1°$). No maximum likelihood fit was implemented, hence the significance of the detection ($> 5\sigma$) only refers to the acceptance threshold required by the peak-search algorithm (Section 5.2.1). The pipeline setup corresponds to that shown in Table B.1 from Appendix B. The considered exposure times were t_{exp} =1, 5, 10, 100 s and a total delay time of 30 seconds was accounted for. In this scenario t_{alert} is considered of few seconds (similar to satellite alert latency or an hypothetical automatic alert system for GW facility). The energy range selected accounted for the southern full-array configuration, with safe cuts from 30 GeV to 150 TeV [7]. Among the candidates identified by the blind-search the source was assumed to be the first one detected (Section 5.1).

Blind-search localisation. Data products are lists of coordinates, statistical errors and blind detection rates. In Table 6.2 all the analysed parameters for the positioning of the candidate source are summarised. While the averaged precision of the peak-search algorithm is scarcely affected by the EBL absorption and IRF half-sensitivity degradation, detection rates drastically decrease at very short exposure times (Table 6.3). From these results one can anticipate that t_{exp} =1 s is not feasible for blind-searches of sources of any brightness (less than 75% of detection rate for an EBL absorbed afterglow with CTA nominal sensitivity and less than 40% with RTA degraded sensitivity, as shown in Figure 6.4(c)). t_{exp} =5, 10 s might be reliable for bright sources, although the detection significance of must be studied before drawing any conclusions.

Figure 6.4 summarises the preliminary results. The right panel shows the positioning of the mean detected source coordinates (over a sample of 10^4 independent realisation of the same event) with respect to the true position of the GRB, for absorbed afterglows (Section 4.6.3). The positioning uncertainties are represented by the error bars for both nominal (blue) and degraded (red) sensitivity. The central panel displays the mean of the computed spherical distance distribution (Section 5.4.1)

[2]The very first results of this study was presented in poster format [114] by G. Stratta, A. Di Piano et al. at the first CTA Symposium held in Bologna, May 2019.

for EBL absorbed (nominal sensitivity in green colour and degraded sensitivity in blue colour) and unabsorbed (nominal sensitivity in yellow colour and degraded sensitivity in red colour) as a function of the exposure time. As expected, the positioning precision improves with longer exposure, yet it is clear that while within the first 5-10 s the uncertainty drastically changes this behaviour and smoothens for exposures above 10 s. This translates in a small gain in localisation precision for relatively (with respect to RTA short-timescales) large increase in exposure time above $t_{exp} = 10$ s. The left panel represents the detection rates at 1 s of exposure time, as mentioned.

In Appendix D the parameter distributions of coordinates (individually presented) and the spherical distance between the true position of the source and the detected location are displayed for all considered exposure times. Each plot compares the performances for different initial assumptions on EBL absorption and IRF degradation. These plots show how, singularly, both coordinates are normally distributed around the true coordinate value (as evident in Table 6.2). After computing the great-circle distance between the detected coordinates and the true position of the source, data should follow a Rayleigh (Section 5.4.2) distribution. One should keep in mind that these results are still biased by the intrinsic flux of the source (issue addressed in Section 6.5) and the IRF degradation process (Section 3.6). In particular, IRF degradation via reduction of the effective area only translates in lower re-computed background rates which probably contributes to the high averaged localisation precision (Table 6.2) independently from the detection rates (Table 6.3). In conclusion, from this testing phase an initial lower limit could be set for the minimum exposure time required for reliable blind-search within RTA context (t_{exp} =5 s) which will be accounted for in further analyses.

t_{exp} (s)	RA (deg)		DEC (deg)		$\Delta\Theta$ (deg)
	μ	σ	μ	σ	γ
EBL unabsorbed & nominal sensitivity					
1	33.057	0.032	-51.840	0.021	0.02
5	33.057	0.016	-51.841	0.011	0.01
10	33.056	0.011	-51.841	0.01	0.008
100	33.054	0.001	-51.840	0.009	0.007
EBL unabsorbed & degraded sensitivity					
1	33.057	0.045	-51.840	0.028	0.028
5	33.057	0.022	-51.841	0.013	0.013
10	33.057	0.016	-51.841	0.011	0.01
100	33.055	0.004	-51.840	0.01	0.007
EBL absorbed & nominal sensitivity					
1	33.058	0.055	-51.840	0.034	0.034
5	33.057	0.026	-51.841	0.016	0.016
10	33.057	0.019	-51.841	0.012	0.012
100	33.055	0.007	-51.840	0.01	0.008
EBL absorbed & degraded sensitivity					
1	33.059	0.072	-51.840	0.047	0.046
5	33.057	0.036	-51.841	0.022	0.022
10	33.057	0.026	-51.840	0.016	0.016
100	33.056	0.012	-51.841	0.01	0.009

Table 6.2

t_{exp} (s)	Rates (%)			
	No Det.	$\Delta\Theta < 0.5°$	$\Delta\Theta < 0.2°$	$\Delta\Theta < 0.1°$
EBL unabsorbed & nominal sensitivity				
1	0.35	97.71	97.71	97.62
5	0.0	100.0	100.0	100.0
10	0.0	100.0	100.0	100.0
100	0.0	100.0	100.0	100.0
EBL unabsorbed & degraded sensitivity				
1	0.22	74.27	74.21	73.55
5	0.0	99.99	99.99	99.99
10	0.0	100.0	100.0	100.0
100	0.0	100.0	100.0	100.0
EBL absorbed & nominal sensitivity				
1	4.57	76.13	75.97	74.55
5	0.01	99.99	99.99	99.99
10	0.0	100.0	100.0	100.0
100	0.0	100.0	100.0	100.0
EBL absorbed & degraded sensitivity				
1	0.76	39.64	39.27	36.98
5	0.77	98.69	98.69	98.53
10	0.0	99.96	99.96	99.95
100	0.0	100.0	100.0	100.0

Table 6.3

Tables: **Left** Gaussian distributed quantities are characterised by their mean and standard deviation, Rayleigh distributed variables are described by the parameter γ (Section 5.4.2) instead, equal to the mode of the distribution. Note that for Rayleigh distributed data, mean and mode do not correspond. Specifically, $\mu = \sqrt{\frac{2}{\pi}}\gamma$. **Right** Detection rates of the peak-search algorithm for a range of exposure times (t_{exp} =1, 5, 10, 100 s) and different use-case assumption (EBL unabsorbed, EBL absorbed, CTA nominal sensitivity and RTA degraded sensitivity). Values are given for none detection rate (i.e. the fraction of events in which the peak-search algorithm could not detect any candidate source), and the fraction of events whose localisation precision is below a given threshold ($\Delta\Theta < 0.5°, 0.2°, 0.1°$). Let's consider $t_{exp} = 1$ s, i.e. When the algorithm provides an excess location, this has an uncertainty of 0.046° at degraded sensitivity (1σ=0.055 for the distribution of right ascension values and 1σ=0.034 for declination values) when both EBL absorption and sensitivity degradation are accounted for. Although the result appear to be promising, exposure time considered, one must ascertain the rates at which such performances are obtain. For accuracy better than half 0.2° the detection rate is less than 75% at best (EBL absorbed source observed with RTA sensitivity degradation performance) and drastically drops down to less than 40% when accuracy better than 0.1° if the RTA sensitivity degradation is accounted for. Moreover, there still is no boundary on the detection significance which is expected to further lower these rates. On the opposite side, $t_{exp} \geq 5$ s show a promising efficiency of the peak-search algorithm which now requires the study of the related detection significance.

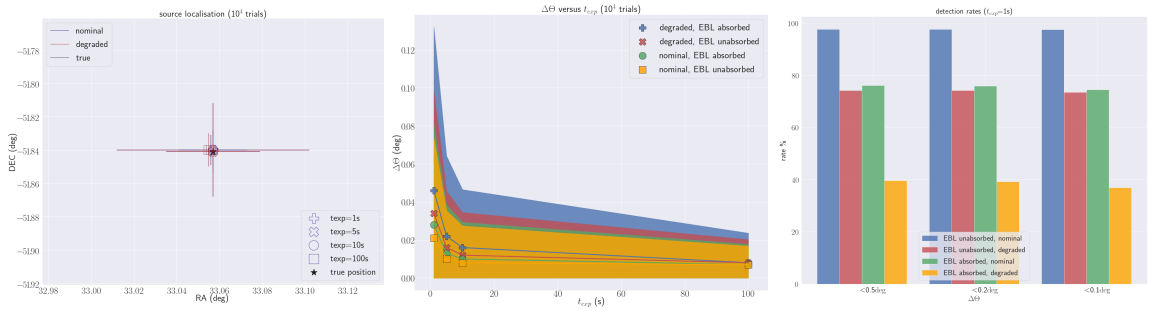

(a) (b) (c)

Figure 6.4: **Right** Equally to the (a) panel, this plot shows the mean positioning of an EBL absorbed afterglow as given by the peak-search algorithm. Once more, in blue are results from CTA nominal sensitivity analysis while in red are RTA degraded sensitivity results. The uncertainty measure is, as expected, worse for the RTA scenario. **Centre** Spherical distance between the detected location of the afterglow and the true position of the source. The uncertainty represents the spherical distance of 1 standard deviation error in right ascension and declination, from zero (the spherical distance is intrinsically defined $\Delta\Theta \leq 0$). **Left** Detection rates at t_{exp} =1 s, for EBL unabsorbed and absorbed afterglows observed with CTA nominal sensitivity and RTA sensitivity degradation. The sample is composed of 10^4 independent realisations of the same event (Section 4.6.3).

6.3 Intermediate tests: minimum t_{exp} required for significant detections

The next step was, for the intermediate tests, to evaluate the maximum likelihood significance of the blind-search detections. The goal was to constrain the short timescales performances and frame a minimum required exposure time for the full field of view maximum likelihood RTA pipeline (i.e. within the considered t_{exp} =5, 10, 100 s). The setup can be found in Appendix B (Table B.1) and refers to what introduced in Section 5.2.1. With respect to the preliminary phase, the most significant (post-fit) candidate is now assumed as the source (i.e. instead of the first detected candidate) for performances comparison. The total delay time was set t_{delay} =30 s with the same considerations of the preliminary phase (see Section 5.2.2). The energy range considered is 30 GeV - 150 TeV, representing a full South array configuration with suggested safe cuts [7]. Tests were run for EBL absorbed sources (Section 4.6.2) with CTA nominal sensitivity and RTA degraded sensitivity (Section 3.6).

Blind-search localisation, detection significance and flux estimation. Data products are lists of coordinates, integral flux estimations and detection significance with related statistical errors. Moreover, detection rates for a given significance threshold (i.e. $\sigma \geq 5$) are given in Table 6.5 alongside the aforementioned. Differently from the preliminary phase, rates now indicate the fraction of events localised within a given spherical distance from the true position of the source ($\Delta\Theta < 0.5°, 0.2°, 0.1°$) only accounting for $\sigma > 5$ detections. The significance of a detection is given by the Test Statistic value of the maximum likelihood, which appear to be normally distributed in a sample of 10^4 independent realisation of the same event (Figure 6.5(b)). From Section 6.1 and Section 3.5 the relationship between TS ad Gaussian significance can be derived as $TS = \sigma^2$, hence values are provided in terms of $\sqrt{TS}$. In Table 6.4 one can find the spherical distance, detection significance and integral flux distribution parameters (Gaussian μ and σ for detection significance and integral flux, Rayleigh γ for the spherical distance). The localisation precision (Figure 6.5(a)) is $\Delta\Theta < 0.1°$ for the full energy coverage at both nominal and degraded sensitivity for exposure times above 100 s. Note the improvement in the source localisation with respect to Table 6.2 for EBL absorbed sources analysed at CTA nominal sensitivity and RTA degraded sensitivity. This is due to the analysis of a number of candidates (i.e. $N_{src} = 5$), the most significant of which is assumed to be the source, contrary to the previous strategy of assuming the first detected candidate as the source without any further investigation. In Appendix E the confidence region for the localisation parameters are shown as computed from a Rayleigh distribution (Figure E.2) compared to those derived from the covariance of the normally distributed coordinate values (Figure E.3). The detection significance distribution is also presented within the same appendix, comparing the significance at different exposure times both for nominal and degraded sensitivity (Figure E.2). In Table 6.5 detection rates are reported as slightly lower than Table 6.3, because of the

further constraints of the aforementioned minimum significance threshold for positive detection. From these results, $t_{exp} = 5$ s was assumed to be an unreliable lower limit for efficient positive detection at short exposure times (Figure 6.5(c)). In order to maintain a conservative approach, a minimum $t_{exp} = 10$ s will hereinafter be required. In this way, a localisation precision $\leq 0.1°$ should be granted for.

t_{exp} (s)	Significance (σ)		F (ph/cm^2/s)		$\Delta\Theta$ (deg)
	μ	σ	μ	σ	γ
nominal sensitivity					
5	12.6	1.6	5.9e-9	1.1e-9	0.016
10	17.8	1.6	5.8e-9	7.7e-10	0.012
100	53.4	1.8	5.4e-9	2.8e-10	0.008
degraded sensitivity					
5	9.0	1.5	5.9e-9	1.5e-9	0.022
10	12.6	1.6	5.9e-9	1.1e-9	0.016
100	37.7	1.8	5.4e-9	4.0e-10	0.009

Table 6.4

t_{exp} (s)	Rates (%)			
	No Det.	$\Delta\Theta < 0.5°$	$\Delta\Theta < 0.2°$	$\Delta\Theta < 0.1°$
nominal sensitivity				
5	0.01	99.98	99.98	99.39
10	0.0	100.0	100.0	100.0
100	0.0	100.0	100.0	100.0
degraded sensitivity				
5	0.77	98.69	98.69	47.81
10	0.0	97.96	99.96	98.31
100	0.0	100.0	100.0	100.0

Table 6.5

Tables: Gaussian and Rayleigh distributions of the parameters (left) and detection rates of $\sigma \geq 5$ detection (right). See Table 6.2 and Table 6.3 for reference. Values are given for a range of exposure times ($t_{exp} = 5$, 10, 100 s) and different use-case assumption (CTA nominal sensitivity and RTA degraded sensitivity). Let's consider $t_{exp} = 5$ s, i.e. When the algorithm provides an excess location, this has an uncertainty of 0.022° at degraded sensitivity (0.016° at nominal sensitivity) at the mode of the Rayleigh distribution, which is better than what reported in Table 6.2 due to the analysis of a sample of candidates among which the most significance is assumed to be the source (instead of the first identified). The detection rates (for a given significance threshold, i.e. 5σ) also seem promising. For accuracy better than half 0.2° the detection rate is higher than 98% at degraded sensitivity and higher than 99% at nominal sensitivity. It drastically drops down to less than 50% when accuracy better than 0.1° is required if the RTA sensitivity degradation is accounted for, which is an indication that $t_{exp} \geq 5$ s would be a better, more conservative choice if one was to account for late-time or average-to-faint sources detection with the RTA.

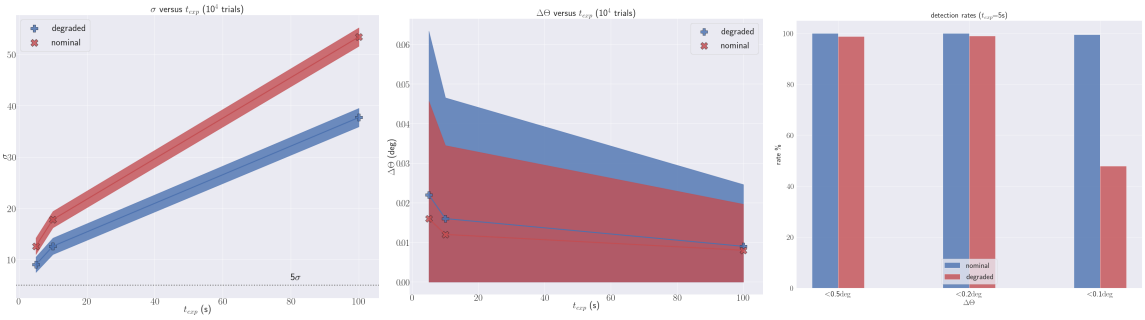

(a) (b) (c)

Figure 6.5: **Left** The average significance of the detection is displayed (with 1 standard deviation uncertainty) as a function of the exposure time. Nominal sensitivity analysis is shown in red, while degraded sensitivity analysis is in blue. As expected, within the RTA context the same event is detected with lower significance. **Centre** Average localisation precision for nominal (red) and degraded (blue) sensitivity analysis. The uncertainty represents the spherical distance of 1 standard deviation error in right ascension and declination, from zero (the spherical distance is intrinsically defined $\Delta\Theta \leq 0$). The average significance of the detection is displayed (with 1 standard deviation uncertainty) as a function of the exposure time. Nominal sensitivity analysis is shown in red, while degraded sensitivity analysis is in blue. As expected, within the RTA context the same event is detected with lower significance. extbfRight Detection rates at t_{exp} =5 s, for EBL unabsorbed and absorbed afterglows observed with CTA nominal sensitivity (red) and RTA sensitivity degradation (blue). The sample is composed of 10^4 independent realisations of the same event (Section 4.6.3).

6.4 Light-curves: follow-up of a short GRB afterglow with the RTA prototype pipeline

Once a positive detection is achieved by the RTA, the follow-up observation is scheduled for as long as the GRBs remains detectable, plus 2 additional hours after the last acquired positive detection. The strategy for RTA would be to integrate in time, from time windows of a few seconds up to half an

hour. This work presents a simplified strategy for RTA follow-up analysis, with fixed time windows of 10 s and larger integrated time windows of 100 s. Therefore, the time of the last acquired positive detection refers only to short-time analysis, as the sensitivity improves at increasing exposure times (Section 3.2, Figure 3.3). In Appendix A the expected lower boundary for the minimum flux is given as a function of the exposure time (Figure A.1). The sensitivity was computed assuming the GRB being at on-axis position, hence from the follow-up analysis one can expect higher values (both for 10 and 100 s of exposure time) due to the unknown location of the transient which translates in an off-axis analysis. The follow-up analysis was performed for a single event with different time delay assumptions: an average case scenario of $t_{delay} = 30$ s and a worst case scenario of $t_{delay} = 50$ s. As explained in Section 4.6.3 and Section 5.2.2, these latency values are representative of automatically generated alerts (i.e. from current on-space observatories). Since a fixed time binning has been chosen, the initial time delay is of no relevance. The lower boundary of each time bin could be assumed as the starting time of the observation. The general setup of the pipeline refers to Table B.1 in Appendix B.2, and Table 6.1. The energy range covered from 30 GeV up to 150 TeV, matching the full-array configuration coverage. Analysis were executed both with nominal and degraded sensitivity in order to compare nominal and degraded sensitivity performances (Section 3). Table 6.6 represents a summary of the performances of the follow-up analyses with the RTA prototype.

In Figure 6.6 are presented results from the t_{delay} worst case scenario. The comparison is between 10 s (left) and 100 s (right) binned light-curves for nominal (blue) and degraded (red) sensitivity. The error bars account for the time integration interval along the x-axis, and for flux uncertainty as provided by the maximum likelihood algorithm (Section 5.1) along the y-axis. The bottom panel of the figure shows the decrease in the significance for each detection (or upper limit) as a function of the exposure time. The observation starts at t_{delay}[3] from the onset of the afterglow emission, and lasts until two hours after the last acquired positive detection. In case of positive detection it means that a maximum likelihood significance of $\sigma \geq 5$ is implied. If compared to real observations (Section 4.5 and Figure 4.6.3), one can conclude that the CTA can detect and correctly analyse data via real-time analysis at very-short exposure times ($t_{exp} = 10$ s) with high significance ($\sigma > 5$) as long as the GRB is not too faint ($F \geq 10^{-10}$ ph/cm^2/s with $t_{exp} = 10$ s and $F \geq 4 \cdot 10^{-10}$ ph/cm^2/s with $t_{exp} = 100$ s for unbinned analysis in 30 GeV - 150 TeV) or localised too late ($t_{delay} > 10^3$ s with $t_{exp} = 10$ s and $t_{delay} > 2 \cdot 10^3$ s with $t_{exp} = 100$ s). The localisation precision is lower than 0.05°. Note that upper limits plateau around sensitivity thresholds of Table 3.1, with a slight degradation due to the unknown off-axis position of the source.

If one asks oneself, would the RTA have been able to detect phenomena such as GRB190114C and/or 180720B? From Section 4.6.3 comparison between the used template and the real observations have been drawn. From the lightcurve comparison between MAGIC data and the template in use (within the same energy range of 300 GeV 1 TeV), a 1.5 order of magnitude difference in the integral flux was found, with the template being the fainter. Nonetheless, with RTA degraded sensitivity the simulated afterglow could be observed with $5 \leq \sigma \leq 20$ detection significance for the first ∼30 minutes using fixed exposure times of 100 s (Figure 6.6(b)) over a much wider energy range than MAGIC or H.E.S.S. observation. For the first ∼10 minutes of the mocked follow-up, the RTA could even detect the source with only 10 s of exposure time, reaching a detection significance $5 \leq \sigma \leq 12$. Even better, computing the integral sensitivity for 100 s of exposure time in H.E.S.S. and MAGIC detection energy ranges (100 GeV - 440 GeV the former and 300 GeV - 1 TeV the latter), the question was more directly answered with *yes*. The foreseen RTA integral sensitivity for H.E.S.S. detection (100 GeV - 440 GeV) is of a minimum integral energy flux half to one order of magnitude fainter than that observed for GRB180720B, with 100 s of exposure time (lower than the exposure time of H.E.S.S. detection). With respect to MAGIC energy range, with 100 s exposure time (also averagely lower than the exposure time of MAGIC detections) the integral sensitivity is of about a one to two order of magnitude fainter minimum integral flux than GRB190114C. About H.E.S.S. detection, the minimum exposure time to obtain an integral photon flux (100 GeV - 440 GeV) of about $4.5 \cdot 10^{-11}$ ph/cm^2/s (computed from the Extended Data Table 1 of [41] at fixed spectral index) is 150 s for CTA nominal and 300 s for RTA degradation. Prospects on the RTA foreseeable capabilities of detecting similar events can therefore be positively derived.

[3] As an alternative, one can arbitrarily consider $t_{delay} + nt_i$ where n is the number of the assumed first time bin and t_i is its lower boundary.

IRF	t_{exp} (s)	t_{delay} (s)	t_{+2h} (s)	t_{end} (s)	$F_{plateau}$ (ph/cm^2/s)
N	10	30	1575	8780	$7.85 \cdot 10^{-10}$
N	100	30	3080	10330	-
D	10	30	1135	8340	$1.14 \cdot 10^{-9}$
D	100	30	1980	9230	-
N	10	50	1575	8780	$7.85 \cdot 10^{-10}$
N	100	50	3100	10350	-
D	10	50	1135	8340	$1.14 \cdot 10^{-9}$
D	100	50	2000	9250	-

Table 6.6: Summary of the RTA prototype performances on a short GRB afterglow follow-up analysis. For each test the IRF of reference is indicated as either nominal (N) or degraded (D). The exposure time of the time binned analysis can be found in the t_{exp} entry, while t_{+2h} and t_{end} represent the time of the last acquired positive detection (to which 2 hours of observation are added) calculated at the bin centre and the total duration of the follow-up given at as uppermost boundary of the bin, respectively. Finally, the entry $F_{plateau}$ represents the constant value around which the upper limits distribute (when present). It can be assumed as indicative measure of the degradation in sensitivity with respect to Table 3.1, due to the off-axis position of the source within the field of view.

6.5 Final tests: statistical study at decreasing intrinsic source brightness

A final phase of tests comprised of EBL absorbed sources with varied intrinsic spectral intensities. From the above, exposure times of 10 and 100 s were considered within the energy band covering from 30 GeV to 150 TeV. Parameter distributions were studied over 10^4 trials sample, including for positioning parameters, integral flux estimation and detection significance. The analysis setup refers to Table B.1 in Appendix B.2, with specific summarised in Table 6.1. The time interval was arbitrarily selected from the follow-up analysis as the one corresponding to the most significant detection ($\Delta t = (90, 100)$ s for $t_{exp} = 10$ s and $\Delta t = (50, 100)$ s for $t_{exp} = 100$ s). Both nominal and degraded sensitivity were accounted for in order to obtain performances comparison.

Preliminary study on the impact of the intrinsic source intensity. All the aforementioned tests (blind-search localisation, integral flux estimation and detection significance determination) were performed for sources of different flux (nominal, 1/2 and 1/3) of the simulated short GRBs afterglow[4]. Each test comprised a sample of 10^4 realisations of the event which were then analysed for $t_{exp} = 10, 100$ s with the RTA prototype pipeline. In Table 6.8 detection rates for a range of spherical distance thresholds are shown, while Table 6.7 summarises the source localisation, the integral photon flux estimate and the detections significance (in Figure 6.7 an example for degraded sensitivity analysis at $t_{exp} = 10$ s, see Appendix G for more). The average spherical distance (left panel) increases as the source flux decreases, broadening the spread of the distribution meaning that the performances degrade in accuracy for the source localisation. Estimating the flux (central panel) becomes less precise as well, due to the lower count number of the source with respect to a given background level. As one can expect, for lower flux values the significance of the detection decreases. The spread of significance distribution is independent from the source flux (right panel). What is of interest is the mean, which is significantly lower at decreasing flux although its decrease is slower than the decrease in flux (a source that has a third of the template flux is detected with more than a third of the significance that a source of the template nominal flux is detected with).

While the intrinsic flux level (for the considered sample) has limited influence on detection rates for t_{exp} =100 s time binning, the impact on very-short exposure times (i.e. t_{exp} =10 s) is important as the sensitivity limit is sooner reached. One can conclude that initial integration time of $t_{texp} = 10$ s is feasible for the RTA for bright sources or fast reacting follow-up analysis for highly significant detection ($\sigma > 5$). As the delayed time increases (or for fainter sources that are below the sensitivity limit for very-short exposure) an initial time integration of 100 s should be used instead. To further constrain the reliability of the pipeline and to avoid source related biases, extensive tests with different simulated GRBs (i.e., spectra, light-curves) and with different observing condition (i.e. zenith angle, array site, array configuration and off-axis angle) are required. Furthermore, sensitivity degradation is

[4]One can also read these results as the study of a single source at different times of its decaying emission.

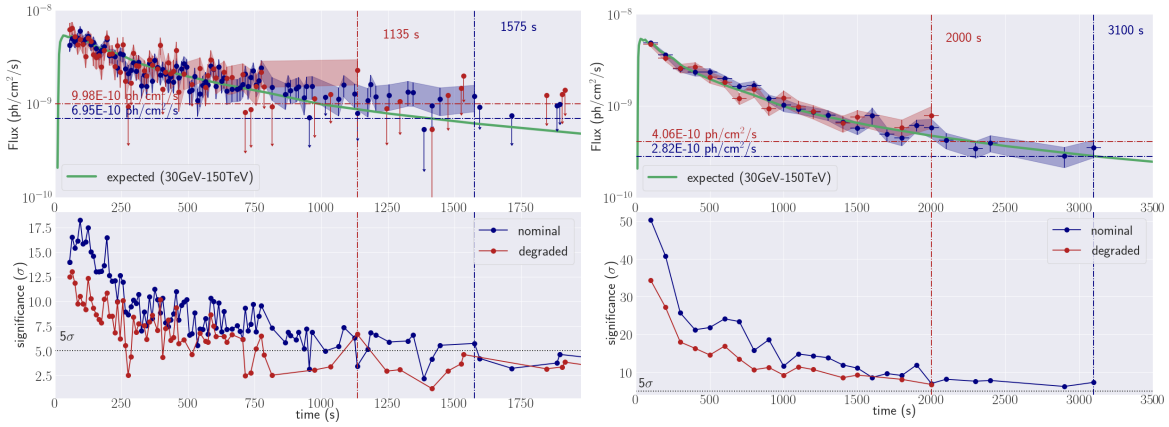

(a) (b)

Figure 6.6: GRB afterglow lightcurves for a 10 s time binned RTA analysis (left) and a 100 s RTA time binned analysis. Nominal (blue) and degraded (red) sensitivity analysis are compared with the expected (green) in each case. The expected is plotted directly from the EBL absorbed template, within the indicated energy range (30 GeV - 150 TeV). Both plots present the lightcurves (integral photon flux as a function of the observation time) in the top panel, while the bottom panel shows the change in detection significance as a function of the observing time. Horizontal lines have been drawn at the on-axis sensitivity for nominal (blue dot-dashed line) and degraded (red dot-dashed) sensitivity with t_{exp} =10, 100 s as well as the 5σ significance threshold (grey dotted line). Vertical lines have been drawn at the time of the last positive detection acquired by the RTA pipeline for nominal (blue dot-dashed line) and degraded (red dot-dashed line) sensitivity. All lightcurves have been shown for a fraction of the observation duration, equal to t_{last}+400 s where t_{last} represent the time of the last acquired positive detection between nominal and integral sensitivity (in Appendix F the full extension of the follow-up observation can be found).

not sufficiently described by effective area reduction only (as shown by these results and the previous ones) as the re-normalised background rates are not representative of less scrupulous background rejection expected of the RTA. Hence, further investigation should require the degradation of the background rates as well as the effective area.

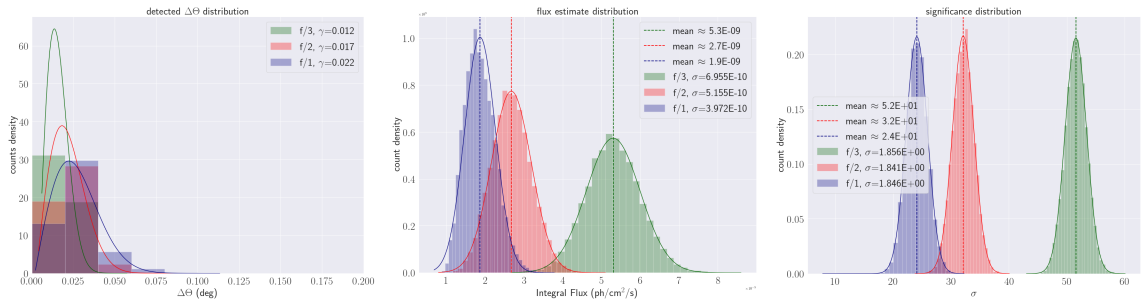

(a) (b) (c)

Figure 6.7: Statistical distribution of spherical distance between the true source position and the detected coordinates (left), the integral flux estimate distribution (centre) and the distribution of the detection significance (right). Data were derived by the analysis of a 10^4 sample of trials, accounting for RTA degraded sensitivity. Nominal intrinsic source flux (blue), a half (red) and a third (green) have been displayed of t_{exp} = 10 s (see Appendix G for more). Histograms are fitted with theoretical distributions characterised by their parameters as summarised in Table 6.7.

IRF	I_{src}	$\Delta\Theta$ (deg)	F (ph/cm^2/s)		Significance (σ)	
		γ	μ	σ	μ	σ
$t_{exp} = 10$ s						
N	-	0.012	5.3e-09	6.95e-10	16.7	1.6
D	-	0.016	5.31e-09	9.98e-10	11.8	1.6
N	1/2	0.017	2.67e-09	5.15e-10	10.4	1.5
D	1/2	0.023	2.81e-09	6.52e-10	7.6	1.3
N	1/3	0.022	1.86e-09	3.97e-10	8.0	1.3
D	1/3	0.027	2.23e-09	4.67e-10	6.5	1.0
$t_{exp} = 100$ s						
N	-	0.008	5.11e-09	2.82e-10	51.6	1.8
D	-	0.01	5.12e-09	4.06e-10	36.5	1.9
N	1/2	0.01	2.57e-09	2.18e-09	32.1	1.8
D	1/2	0.013	2.58e-09	3.11e-10	22.7	1.9
N	1/3	0.013	1.72e-09	1.91e-10	24.1	1.8
D	1/3	0.018	1.74e-09	2.69e-10	17.1	1.9

Table 6.7

IRF	I_{src}	Rates (%)			
		No. Det.	$\Delta\Theta < 0.5°$	$\Delta\Theta < 0.2°$	$\Delta\Theta < 0.1°$
$t_{exp} = 10$ s					
N	-	-	98.36	98.36	98.36
D	-	0.01	93.92	93.92	93.92
N	1/2	0.2	97.36	97.36	97.36
D	1/2	8.16	78.93	78.93	78.85
N	1/3	9.34	79.96	79.96	79.94
D	1/3	36.03	32.37	32.38	32.29
$t_{exp} = 10$ s					
N	-	-	99.33	99.33	99.33
D	-	-	99.57	97.55	97.55
N	1/2	-	99.35	99.35	99.35
D	1/2	-	98.73	98.72	98.72
N	1/3	-	99.67	99.66	99.66
D	1/3	1.68	94.04	94.01	94.01

Table 6.8

Tables: Gaussian and Rayleigh distributions of the parameters (left) and detection rates of $\sigma \geq 5$ detection (right). See Table 6.2 and Table 6.3 for reference. Values are given for a range of exposure times ($t_{exp} = 10$, 100 s) and different use-case assumption (CTA nominal sensitivity and RTA degraded sensitivity). See also Table 6.4 and Table 6.5 for reading examples.

Chapter 7

Conclusions

In this chapter the main results from my project will be summarises in order to draw the final conclusions. Improvements that this work could further benefit from will also be outlined, both in terms of further testing of the pipeline and code implementation, allowing to generalise the prototype to all transient classes and internal alerts as well as external ones. Finally, the future prospects of this study will be presented at the chapter's end.

To conclude the dissertation, the questions posed in Chapter 1 will be answered in the following summary. Topics that will be considered are: *i)* the feasibility of implementing a full-FoV maximum likelihood analysis from `ctools` software package in the RTA, requiring that the prototype false alarm rate abides to the Wilks' theorem (Section 3.5); *ii)* the efficiency and accuracy of these algorithms within the context of MWL/MM transient follow-up, namely the localisation precision and detection rates for the blind-search and follow-up real-time analysis of a short GRB afterglow; *iii)* the comparison between RTA and nominal CTA performances, due to the non-optimal working condition of an automated real-time analysis pipeline, as well as with currently operating IACTs and their most recent observations.

• First of all, a prototype pipeline (Chapter 5) for the RTA has been developed, with the implementation of the full-FoV maximum likelihood analysis method integrated within the `ctools` software package. The pipeline also relies on natively implemented features for data handling, model manipulation and strategy optimisation. Post-processing pipelines and other utility scripts have been produced as well.

• In Section 6.1 the algorithms were tested on a large sample of empty fields (10^6 trials) for verifying the Wilks' theorem, as to ascertain the false alarm rate at very-short exposure times never reached before (down to 1 s). In case of a dof=1 analysis, tests confirmed that the algorithm Test Statistic values distribute abiding to the Wilks' theorem and can therefore be associated with relative p-values. The relation TS=σ^2 is hence confirmed also at very-short exposure times. A warning must be raised for 3 degrees of freedom analysis for exposure times below 100 s, as the TS distribution is found not in agreement with the Wilks' theorem with respect to the used setup (Chapter 5). If required, one should beforehand test if the Wilks' theorem can be verified by (i.e.) narrowing the ranges of the free parameters to stricter values.

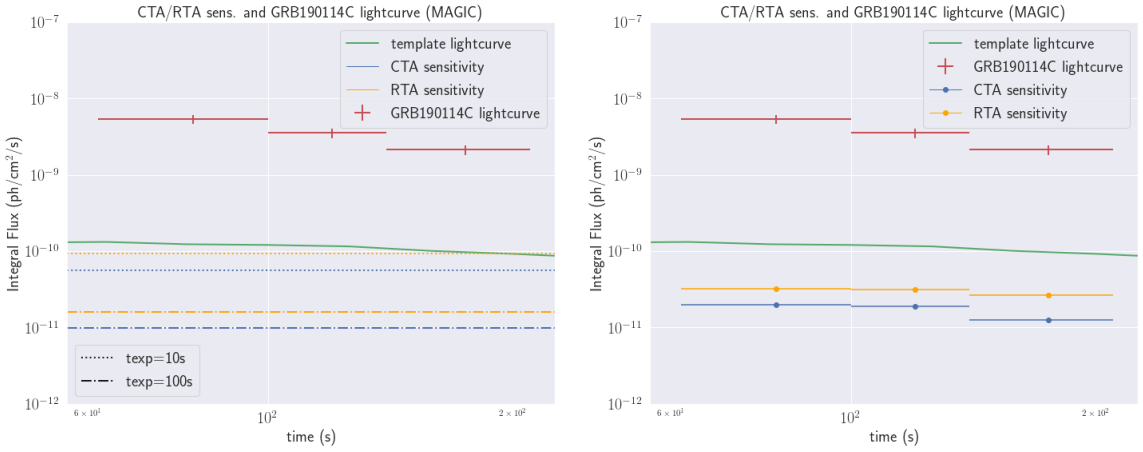

(a) (b)

Figure 7.1: Template lightcurve and GRB190114C lightcurve seen by MAGIC, in the energy range 300 GeV - 1 TeV. The integral photon flux is plotted as a function of the observing time. One can see that the template in use for this study is of about 1.5 order of magnitude fainter than the afterglow detected by MAGIC. In panel (a) the integral photon flux is compared with the CTA and RTA sensitivity (nominal in blue and degraded in orange) at fixed exposure time of 10 and 100 s (dotted and dot-dashed lines respectively). In panel (b) the same curves are compared with the CTA nominal (blue) and RTA degraded (orange) sensitivity for exposure times equal to MAGIC lightcurve time bins (from left to right, $t_{exp} = 38.2, 39.8, 70.28s$). **Credits:** MAGIC collaboration (GRB190114C lightcurve).

• The computation of these algorithms is fast enough to be feasible for the RTA, at least for short exposure times. The time required by the maximum likelihood to be performed on $t_{exp} = 100$ s selected data is approximately summarised in Table 7.1, alongside the duration of the other computationally heavy tasks performed by the pipeline (see Section 5.3 and Appendix 5.2.2 for details on data handling).

	initial setup	sky map	blind-search	likelihood
t_{CPU} (s)	6.5	1.7	1.2	1.4

Table 7.1: Required computation time for the main tasks performed by the RTA pipeline, for $t_{exp} = 100$ s. Please note that reported numbers are indicative.

• The accuracy of the localisation improves of up to a factor of 2 if a number of candidate sources are analysed (i.e. 5) and the source is assumed after evaluation of the maximum likelihood significance as the one returning the highest value above a given threshold, i.e. $\sigma > 5$ (Table 6.2 and Table 6.4). The efficiency of the peak search algorithm also improves up to 100% detection rate for $t_{exp} \geq 5$ s, with respect to Table 6.3. Naturally, the rates are somewhat lower (from a few percents up to a few tens percent) when requiring 5σ detection at least (Table 6.5). The computation time does not exceed feasibility when implementing this feature, measuring up to 0.7 s for $t_{exp} = 10$ s of data with 5 candidate sources and 2.5 s for $t_{exp} = 100$ s, approximately.

• The precision of the source localisation has been found lower than 0.05° for $t_{exp} \geq 5$ s even if sensitivity degradation is taken into account within the RTA requirement of half nominal sensitivity at worst (Chapter 3 and Section 6.3). The localisation accuracy does not exceed this threshold even if fluxes approaching on-axis sensitivity limits are considered, although their detection efficiency drops (none detection rate >30%) at very short exposure times ($t_{exp} \leq 10$ s). A minimum exposure time of 10 s is required in order to detect at least 90% of the events with integral photon fluxes down to $\sim 5 \cdot 10^{-9}$ ph/cm^2/s in the energy range 30 GeV - 150 TeV, with accuracy better than 0.02° and significance above 5σ. If a minimum exposure time of 100 s is required, the RTA could be capable of detecting more than 90% of the events with integral photon fluxes as low as $\sim 1.5 \cdot 10^{-9}$ ph/cm^2/s, with more than 5σ significance and accuracy better than 0.02°, in the energy range from 30 GeV to 150 TeV (Section 6.5).

• Although this work was carried out with simulated data, comparing to the recent observations of

GRB afterglows from currently operating IACTs may shed some light on the actual prospective of the RTA performance. CTA nominal performances have been (and still are) extensively tested by the CTA Consortium members, but the realistic expectation that could be hold for the RTA have never been explored before. As one may recall from Section 4.5, MAGIC detected GRB190114C with significance above 50σ for the first twenty minutes of observation, which started approximately 50-60 seconds after the burst trigger [40] [42]. The integral photon flux (above 300 GeV) is 1.5 order of magnitude brighter then the template used for this study (Section 4.6.3). Still, with fixed temporal windows at $t_{exp} = 100$ s (no further time integration was considered), achieved significance between 50σ and 15σ within the first 2000 s of follow-up at CTA nominal sensitivity in the energy range from 30 GeV to 150 TeV, and significance between 35σ and 10σ at RTA degraded sensitivity for the same follow-up. For the first 10 minutes of follow-up, the outstanding performances of CTA could even enable detection of similar events with significance over 5σ ($5 \leq \sigma \leq 20$ for CTA nominal performance and $5 \leq \sigma \leq 15$ for RTA) at exposure times as low as 10 s. In order to achieve a more direct comparison between the observation of GRB190114C and the CTA/RTA detectability of similar phenomena, the released lightcurve has been plotted with CTA (nominal) and RTA (degraded) integral sensitivity limits (given as the minimum detectable flux in ph/cm^2/s) in the energy range 300GeV-1TeV of MAGIC observation (Figure 7.1). The template (green continuous line) integral flux is given for reference, in the same energy range (300 GeV - 1 TeV) of the GRB190114C lightcurve as seen by MAGIC (red data points). In panel (a) these curves are compared with the minimum integral photon flux detectable above 5σ by CTA in the same energy range. The exposure times of these threshold (blue for CTA nominal sensitivity and orange for the RTA degraded sensitivity) are 10 s and 100 s, in dotted and dot-dashed lines respectively. In panel (b) the same lightcurves from GRB190114C and the template in use, in the energy range from 300 GeV to 1 TeV, are compared to the minimum detectable flux above 5σ at the exact exposure times from MAGIC lightcurve (t_{exp} =38.2, 39.8, 70.28 s). Both the afterglow template and the GRB190114C fluxes are well above the sensitivity limits of CTA nominal (blue data points) and RTA (orange data points). Additionally, H.E.S.S. detection in the energy range 100 GeV - 440 GeV [41] was computed from the Extended Data Table 1 of [41]. At fixed spectral index, the integral photon flux was found of about $4.5{\cdot}10^{-11}$ ph/cm^2/s. It would have been detectable by CTA nominal sensitivity with 150 s of exposure time and by the RTA with 300 s of exposure time ($F_{min} \sim 4 \cdot 10^{-11}$ ph/cm^2/s) .

7.1 Improvements and future prospects

Although this project answered the questions posed at the beginning of the study, further implementation and testing may improve the knowledge of the expected RTA performances, as well as the pipeline itself. Moreover, collaborations opportunities arose with the GRB and GW experts of the CTA Consortium, not only for confrontation and feedback during regular meetings of the GRB and GW experts of the CTA Consortium, but also for possible contributions for their on-going work.

• Other tests that may improve the performances of the analysis are connected with the parameter space (Section 5.2.1). This being the start of the investigation for the RTA alert generation and real-time data analysis, most of the parameters were either kept at default value (i.e. from `ctools` software package) or arbitrarily fixed. Among the parameter that may impact on the performances and that were not tested during this work, are: *i)* sky maps parameters; *ii)* acceptance threshold and smoothing for the peak-search algorithm; *iii)* initial time delay; *iv)* other assumptions on the source model; *v)* further tests on dof>1 analysis. While some of these merely require some testing, a few would need further implementations and study.

i) Sky maps parameters. The pixel size of the count map used in input to the peak-search algorithm may impact the localisation precision of the source. The gain in precision should be compared with the expenses in computation time in order to better optimise the performances of the RTA.

ii) Acceptance threshold and smoothing. The peak-search algorithm may actually be utilised with more relaxed requirements (i.e. $\sigma \geq 3$) as long as the analysis is performed over a number of candidates to whom more conservative thresholds may later be applied (i.e. maximum likelihood significance above 5σ). It may allow for detection at later times as what found in this search, while still maintaining

very short exposure times (it may lower the none detection rates). The smoothing kernel and its radius may also have some impact, specifically on the localisation accuracy (as per the sky map parameters).

iii) Initial time delay. Although some statistical studies have been carried out at different intensities, a more thorough investigation on a randomised time delay (or simply more similar to the current average GW alert latency) would be of great value. The pipeline already allows to randomise the time delay within a given range, but for this work it was preferred to minimise the variables by choosing an arbitrary time delay.

iv) Source model assumptions. Not only tests should be run for a population of (updated) GRBs, both short and long accounting for the prompt emission as well as the afterglow, but also for other transient classes. The RTA (especially the SAG) should be optimised and generalised. It would imply the implementation of a dynamical configuration of the pipeline, based on the knowledge claimed over the observed target (either from other observations or from real-time analysis developments). Although features such as these cannot be finely tuned in an automatic pipeline, further investigation may give some results and predictions. Moreover, the model assumed during the analysis (which should not be confused with the models assumed for the simulation of sources) may be of different type than a simple power law. Broken power laws as well as exponentially cut-off power laws may be interesting choices to investigate, as long as the comparison of gain versus feasibility is weighted.

v) Degrees of freedom. Since the RTA must automatically generate science alerts, treating the source coordinates as free parameters may be of importance. Before quantifying the benefits on the localisation, the Wilks' theorem should be verified. As already mentioned, a possibility may be to give strict ranges for the parameters during the maximum likelihood analysis. Studies in this direction should still consider the gain versus feasibility issue, as computational time is expected to increase for higher dof analysis.

• Further studies on the IRFs degradation are crucial. In this work we have degraded the CTA sensitivity via the reduction of the effective area only. While this achieved to worsen the sensitivity up to a factor of two at worst, a more realistic scenario would require a more complete degradation. First of all, there was no energy dependence accounted for the effective area degradation. Secondly, the background rates should be raised in order to better represent a degradation in the background rejection as a function of the energy and the off-axis angle. Thirdly, the PSF and energy dispersion may also be degraded for finer investigation. One should adjust these factors in order to obtain a total degradation of half the nominal sensitivity at worst.

• Further implementation for the pipeline would comprise of the time integration strategy of the RTA, the re-pointing after a positive detection is achieved and, possibly, a dynamically determined minimum exposure time. The first improvement would require for the RTA to integrate the incoming data until a positive detection is achieved, between a minimum and maximum boundaries on the exposure time. It would require further investigation on the verification of the Wilks' theorem for higher exposure times (especially if higher dof analysis are considered). This is connected to the topic of the time windows determination. By assuming a temporal behaviour beforehand, one may optimise the exposure length as in [3] which is of critical importance in the case of MWL/MM alerts with large localisation uncertainties (i.e. for the current GW follow-up). Finally, the on-axis analysis of the transient should be studied for completeness. Due to the computation time and complexity involved in the simulation process, photon lists were generated for off-axis sources only. Once a positive detection is acquired, though, the array should be re-pointed in order to optimise the observation of the phenomena. The pipeline allows to analyse data on-axis with the source, but the simulations themselves are still accounting for some off-axis angles.

• Finally, future prospects of this work involve the collaboration with GRB experts of the CTA Consortium. During the last year, this project was regularly submitted to the attention of the GRB and GW experts of the CTA Consortium in order to strengthen the collaboration between the RTA and PHYS working group (groups of CTAC members tasked with the different developments in preparation for the CTAO). Other than gaining feedback from other members of the Consortium (i.e. during

regular working group meetings and Consortium meetings), possible collaborations were called for. In particular, some of the GRB experts may be interested in merging some features of this pipeline with their on-going work for the CTAC (data handling and blind-search specifically).

Acknowledgements

Some may say I have spent all my words in the previous chapters and that none remains for giving proper thanks. I'd rather say that thank yous shouldn't require explanations.

To my supervisor, my co-supervisors and the researchers of the Bologna INAF/OAS institute, lovely people whom I met and worked with. To my thesis-twin, the undergraduate crew and the friendly neighbours beyond the glass wall. To the people of CTA and DIFA Bologna. To my family and friends; the new ones, the old ones and those who stuck with me since I can remember. To the close by and the faraway friends. To my favourite chef in the world and to the other half of my brain. To those who taught me so much more than music and I dare add, even to a stranger or two. And to you, who have read all these words without skipping chapters.

Thank you.

Post Scriptum.
There are a few more words ahead, sorry not sorry.

Appendices

Appendix A

Integral sensitivity at very-short exposure times

From Section 3.6, the sensitivity degradation due to CTA performance was derived. Here one can find the full test sample for the integral sensitivity degradation, via effective area reduction. In Figure A.1, the integral sensitivity of CTA nominal (blue) and RTA degraded (orange) performance are given as a function of the exposure time. The sensitivity is evaluated in terms of the minimum integral photon flux required to achieve at least 5σ detection. Integration was performed within 30 GeV and 150 TeV energy range. In Figure A.2 the minimum integral photon flux required to detect an on-axis Crab-like source with at least 5σ of significance is given for 1, 5, 10 and 100 s of exposure time. The integral sensitivity is computed over 20 energy thresholds in the range from 30 GeV to 150 TeV. Additionally, in each plot bottom panel the ratio between the nominal (blue) and degraded (orange) sensitivity is displayed. In order to abide to the RTA requirements, the ratio should be above 0.5.

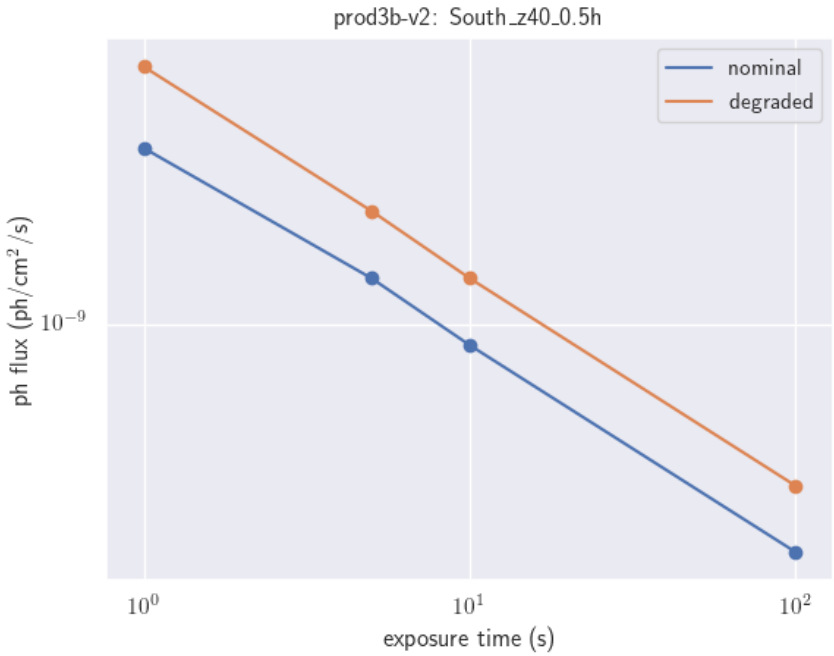

Figure A.1: Minimum detectable integral flux as a function of the increasing exposure time, for a point-like source positioned on-axis and within the energy range 30 GeV - 150 TeV. Data are reported for both nominal (blue) and degraded (orange) sensitivity.

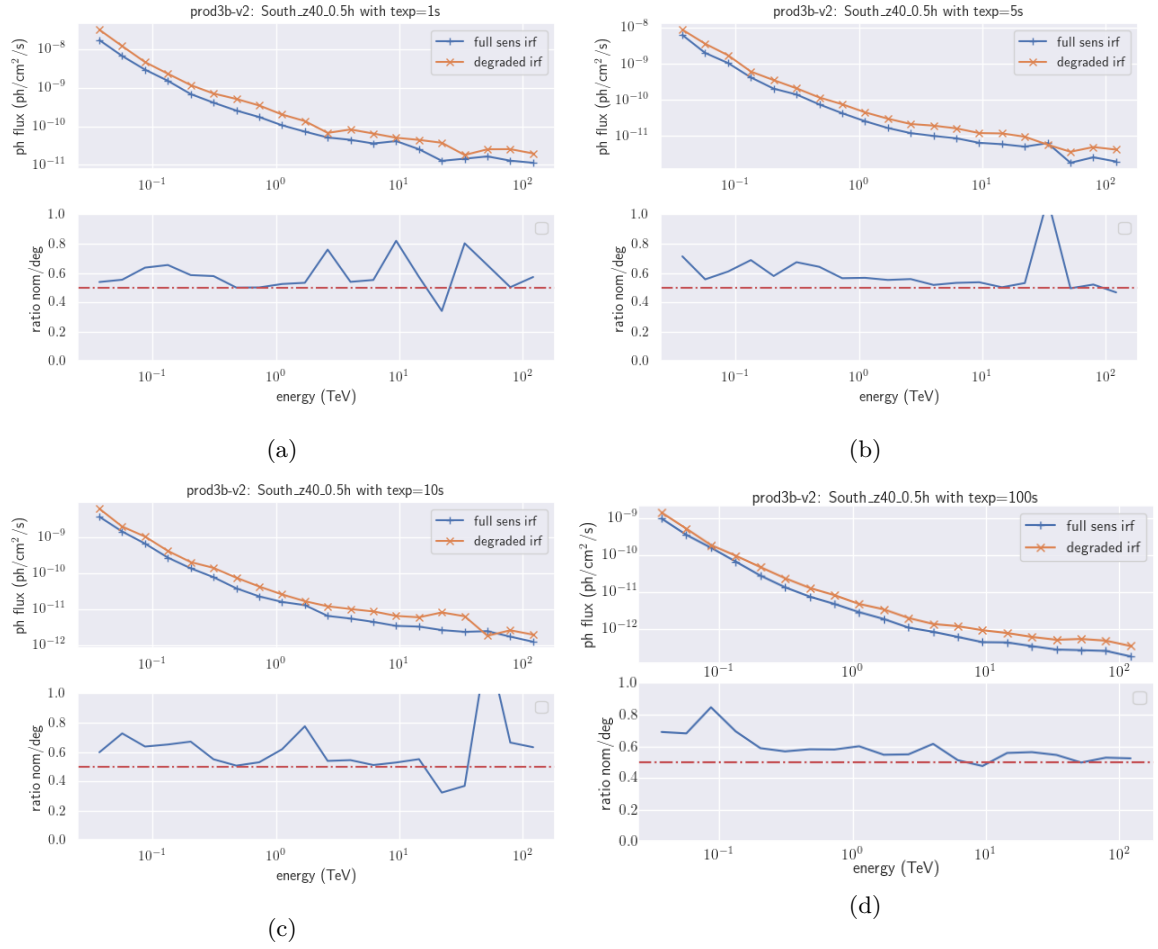

Figure A.2: In the panels are shown the integral sensitivity curves for given energy thresholds and exposure times. Panel (a) $t_{exp} = 1$ s, panel (b) $t_{exp} = 5$ s, panel (b) $t_{exp} = 10$ s, panel (d) $t_{exp} = 100$ s. Each plot is paired with the ratio between nominal and degraded sensitivity. The RTA requirements are that the sensitivity must not be worse than the nominal by more than a factor of two.

Appendix B

Code development and pipeline setup

The pipeline described in Chapter 5 requires a configuration file with explicit paths (data, simulations, pipeline products, etc.) and free parameters. The wide parameter space setup is declared before the actual scripting of the pipeline, though future implementation will require to integrate these information in a dedicated configuration file. In Appendix B.1 an example of the configuration file is reported, while the complete pipeline setup can be found in Appendix B.2. In Appendix B.3 the manipulation of the `ctobssim` MC simulations is explained in further details, with focus on the conversion from template to real-like data format.

B.1 Configuration xml file.

Example of a configuration xml file, for one degree of freedom maximum likelihood analysis. The tree structure for the absolute paths assignment can be simplified by initialising the same path to multiple sub-elements, if convenient. Concerning the degrees of freedom of the maximum likelihood analysis, they are determined by the difference between $M_2(dof) - M_1(dof)$, where M_1 is a background only model and M_2 is a background+source model (Section 3.4).

```
<?xml version="1.0" encoding="utf-8"?>
<config>
  <dir>
        ...
  </dir>
  <xml>
    <src idAttrib="name">
      <free prm="Prefactor" />
    </src>
    <bkg idAttrib="name">
      <free prm="Prefactor" />
      <free prm="Index" />
    </bkg>
  </xml>
</config>
```

Listing B.1: The snippet shows an example of configuration xml file, with *config* root element. The tree structure branches in *dir* element, comprising of one sub-element per required path, and *xml*. The latter is organised in *src* source and *bk* background sub-elements, each one containing as many *free* parameters as required for carrying out the analysis.

B.2 Pipeline setup

The following table presents the general setup of the pipeline, as used for this study. Note that changeable inputs will be presented with all their investigated values. Table B.1 is organised in four

columns: to the utmost left are listed all parameters, variables and inputs. From left to right are then listed the respective values for the follow-up, the blind-search and the Wilks theorem verification versions of the pipeline respectively.

B.3 MC simulations with `ctobssim`

As explained in Section 4.6.3, source events are generated independently for a number of temporal bin (ten equally spaced log-bins per decade). In order to obtain a real-like data photon list to feed to the pipeline, methods such as `appendEventsSinglePhList()` and `AppendEventsMultiPhLists()` have been implemented among the utility methods of class Analysis (Section 5.3). These methods simply append the single time bin generated photon lists into one (or many) of duration $\Delta t_{total} = \sum_i^N \Delta t_i$, where N is the total number of time bins from the template and the Good Time Intervals (GTI) are set to the edges of Δt_{total} unless differently specified (Listing B.2).

```
# created one FITS table containing all events and GTIs ---!
def appendEventsSinglePhList(self, GTI=None):
  if GTI == None:
    GTI = []
    with fits.open(self.input[0]) as hdul:
      GTI.append(hdul[2].data[0][0])
    with fits.open(self.input[-1]) as hdul:
      GTI.append(hdul[2].data[0][1])
  self.__singlePhotonList(sample=self.input, filename=self.output, GTI=GTI)
  return
```

Listing B.2: The method presented allows to create single photon lists from collected observations. The GTI are set to the extremity of the time interval unless otherwise specified.

Consider an observation model of two components: one point-like source and the background, such as the one in Listing B.3. Photon lists are generated with `ctobssim`, an MC simulator from `ctools` software package (Section 5.1). Events simulation proceeds ordered by source type (the background-type component is generated last independently of the listing order of the observation model), meaning that once all time bins photon lists have been merged in a single observation photon list the contained data are not linearly ordered in time. If one plots the time of the events as a function of the table row number (the physical temporal evolution of the events versus the order they are generated with) the result is far from a real-like photon list (Figure B.1(a)). This spike-like features along the temporal dimension are due to `ctobssim` separate generation of source and background events, as data are ordered by the ID of the MC simulation rather than time.

```
<?xml version='1.0' encoding='UTF-8' standalone='no'?>
<source_library title="source library">
  <source name="GRB" type="PointSource" tscalc="1">
    ...
  </source>
  <source name="CTABackgroundModel" type="CTAIrfBackground" instrument="CTA">
    ...
  </source>
</source_library>
```

Listing B.3: The model herein presented has two components: one point-like source and the background. The source is described by a simple power law spectral model and a point-like spatial model (Section 5.1). The background component is described by the template contained within the IRF (Section 3.6).

When analysing data with `ctools` software package utilities no issues arise, since all tools are implemented with intrinsic knowledge of the data structure. To obtain photon lists that can be universally utilised and that resemble as much as possible real observations, data tables have been further manipulated. Specifically, by sorting all events within the boundaries set by the GTI by their time. If one reproduces the plot of Figure B.1(a) after this correction, data will behave as expected of real-like observation data (Figure B.1(b)).

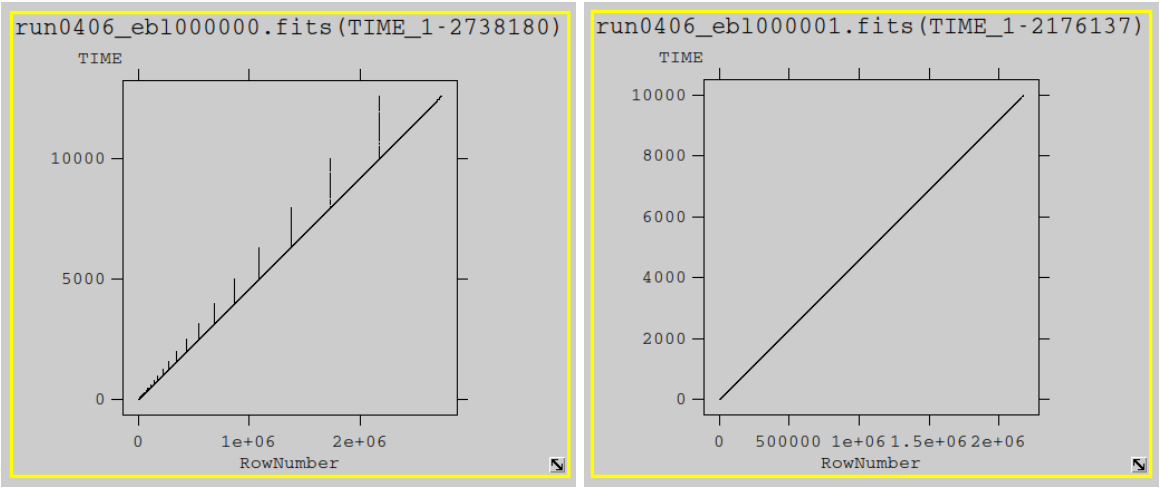

(a) (b)

Figure B.1: Here are shown the time of each simulated event in a 10^4 s long observation. Note how the simple merge of a number of observations (time bins, see Section 4.6.3) produces spiked features in time (left). The reason behind this behaviour is that data are not ordered in time, rather they are ordered by ID of the MC simulation (source first, background last). To obtain real-like data the events have been sorted by time (right).

input	follow-up	blind-srch	wilks
trials	1	10^4	10^6
dof	1	1, 3	1, 3
sGRB template	run0406_ID000126 afterglow	run0406_ID000126 afterglow	-
EBL table	Gilmore 2012 (fiducial)	Gilmore 2012 (fiducial)	-
Apply EBL	yes, no	yes, no	-
add Exp. cut-off	no	no	no
scale src intensity	no	yes	-
sort candidates by TS	yes	yes, no	-
calibration database	prod3b-v2, degr3b-v2	prod3b-v2, degr3b-v2	prod3b-v2
IRF	South_z40_0.5h	South_z40_0.5h	South_z40_0.5h
pointing RA (deg)	31.582	31.582	31.582
pointing DEC (deg)	-53.211	-53.211	-53.211
ROI (deg)	5	5	5
ΔE (TeV)	0.03-150	0.03-150	0.03-150
t_{exp} (s)	10, 100	1, 5, 10, 100	1, 5, 10, 1000
t_{delay} (s)	30, 50	30, 50	-
t_{total} (s)	$1e5$	-	-
t_{run} (s)	1200	-	-
t_{add} (s)	7200	-	-
σ_{blind} threshold	5	5	-
sky map pixel size (deg)	0.02	0.02	-
sky map axes size (pixel)	250	250	-
smoothing corr. kernel rad. (deg)	0.1	0.1	-
N_{max} candidates	5	5	-
$\sigma_{detection}$ threshold	5	5	5
src model	power law	power law	power law
bkg model	IRF type	IRF type	IRF type

Table B.1: From left to right, columns contains the parameters required by the setup (either condition control, input files or variables) and the values for the follow-up version of the pipeline, the blind-search or the Wilks' theorem verification versions respectively. Pipeline description can be found in Section 5.2 and 5.3.

Appendix C

Wilks' theorem verification

All the samples for the false positives verification described in Section 6.1 are given for dof=1 analysis (Figure C.1) and dof=3 analysis (Figure C.2). As anticipated, one can see how the TS distributions of a dof=3 analysis never abides to the Wilks' theorem. It may be due to the parameter ranges of the model, as assumed during the fitting procedure. Further tests with stricter parameter ranges on the spatial coordinates may unravel this still unresolved issue.

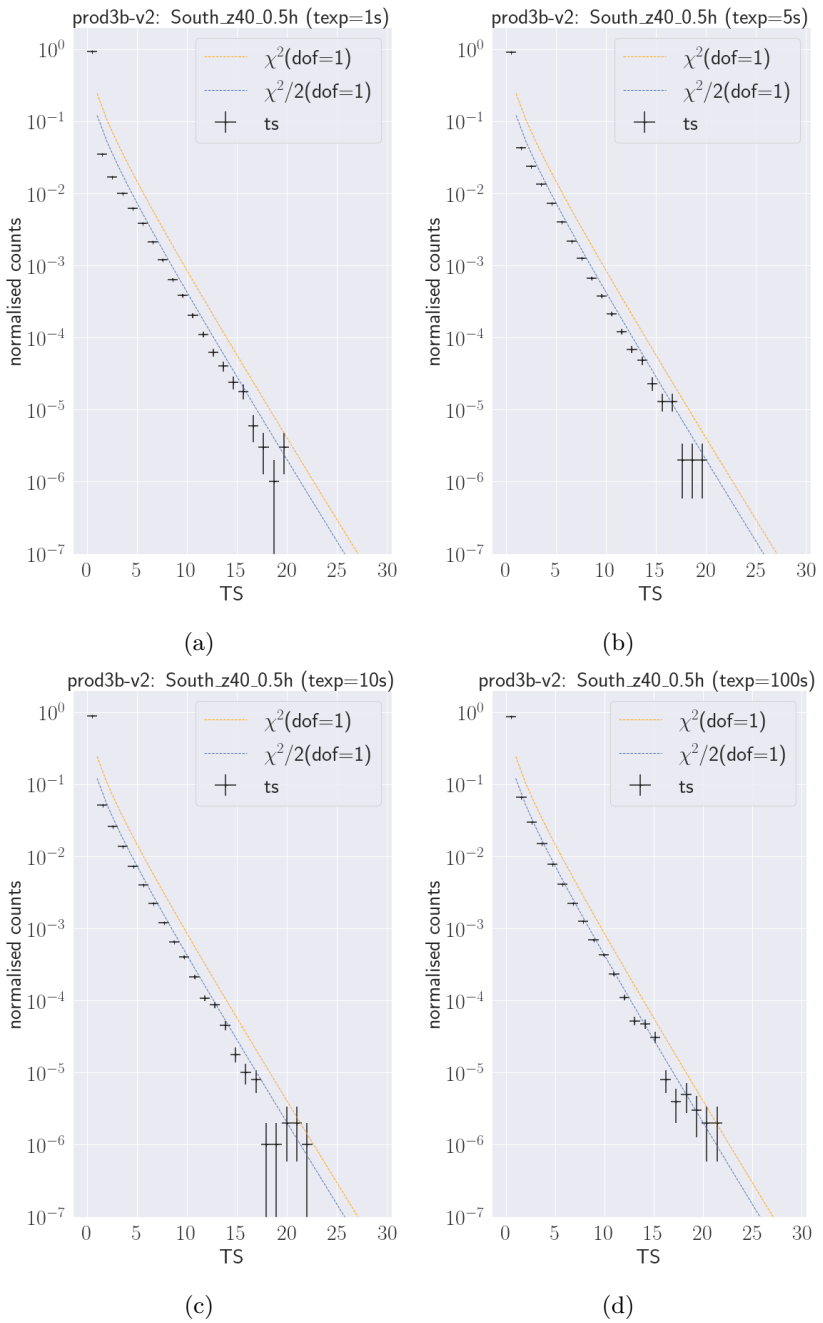

Figure C.1: The graphic shows the `ctlike` resulting TS distribution (black dots) from 1e6 empty fields best fit (dof=1) to the source's model template. Exposure times: (a) 1s , (b) 5 s, (c) 10 s and (d) 100 s. The histogram was fitted with a $\chi^2/2$ distribution (blue dashed line) which is in agreement with Wilks' theorem. Note that the first TS bin is excluded as it would require a best fitting segmented function which was not the scope of this work.

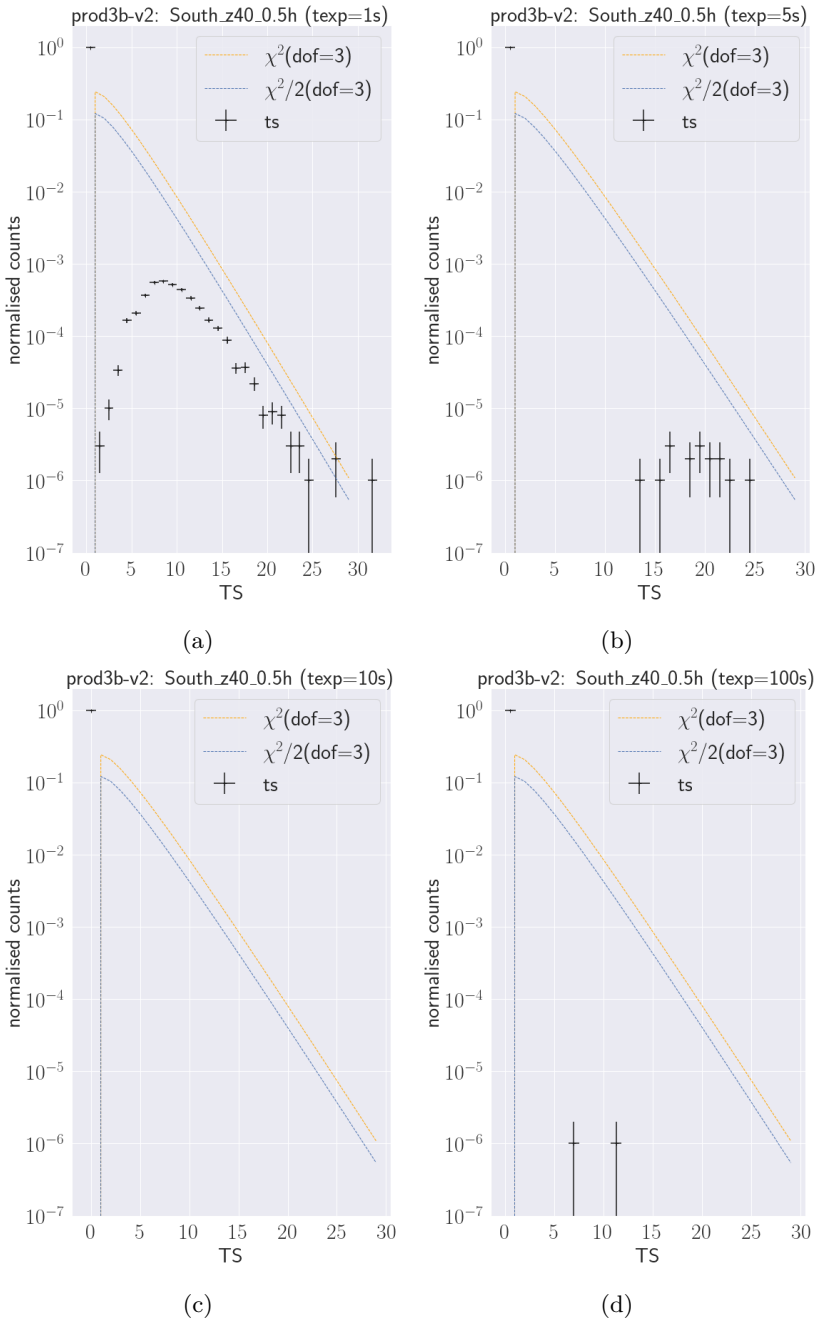

Figure C.2: The graphic shows the `ctlike` resulting TS distribution (black dots) from 1e6 empty fields best fit (dof=3) to the source's model template. Exposure times: (a) 1s , (b) 5 s, (c) 10 s and (d) 100 s. The histogram was fitted with a $\chi^2/2$ distribution (blue dashed line) and the result is clearly not in agreement with Wilks' theorem. Further investigation is required and `ctlike` convergence may be found for stricter parameter ranges in the spatial component of the source model.

Appendix D

Preliminary tests

Here the spatial parameter distributions for all exposure times (1, 5, 10, 100 s) of the preliminary test phase (Section 6.2) are shown. Figure 6.4 compare the results of EBL absorbed and unabsorbed analysis, as well as nominal and degraded sensitivity performance. From top to bottom, rows refer to 1, 5, 10 and 100 s exposure time analysis. From left to right, columns display distributions of the right ascension, declination and spherical distance from the true position.

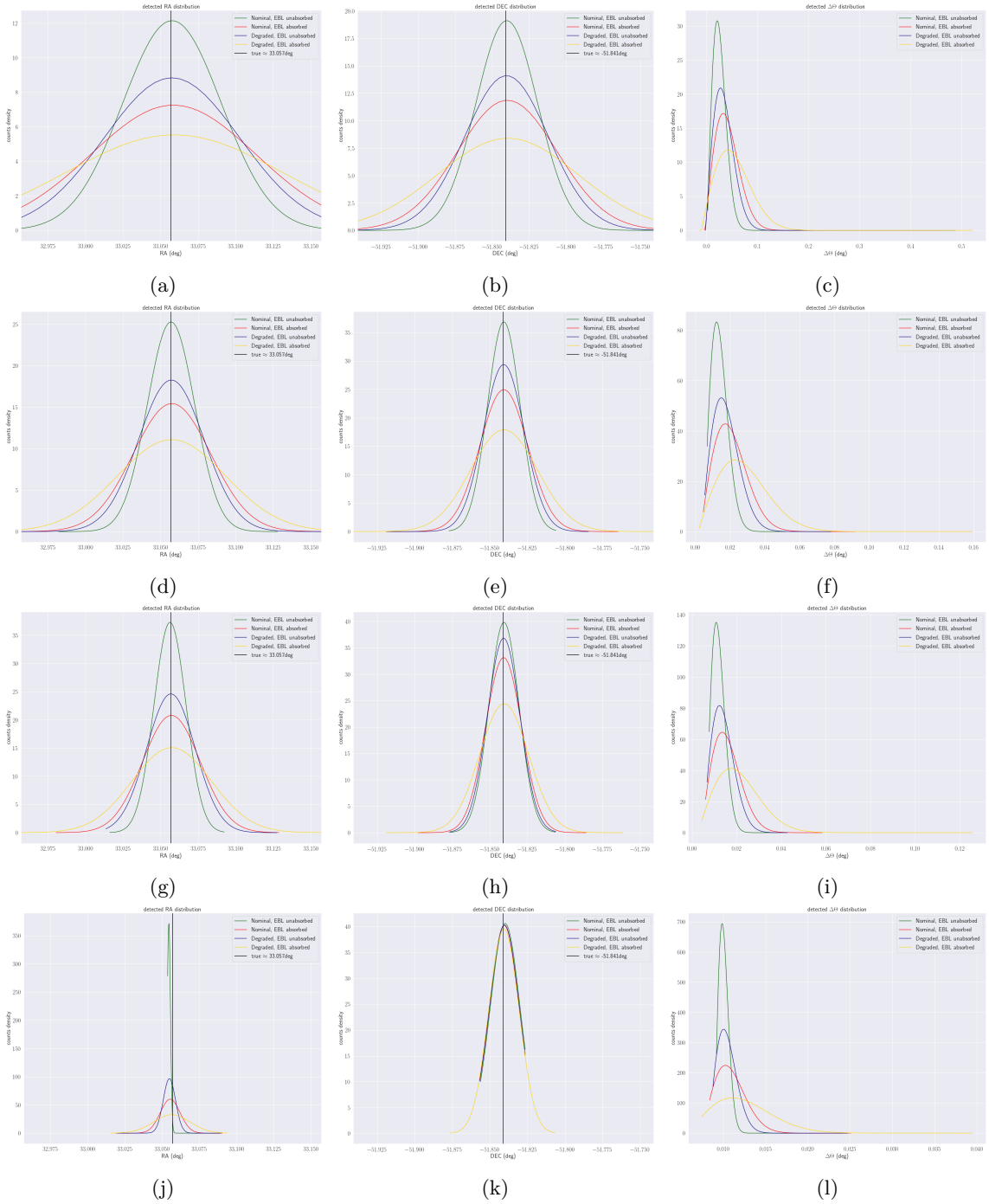

Figure D.1: **Left panels** Parameter (right ascension) distributions of 10^4 independent realisation of the same event, retrieved from $t_{exp} = 1$ s observation analysis (a), $t_{exp} = 5$ s (d), $t_{exp} = 10$ s (g) and $t_{exp} = 100$ s (j). The statistics accounts for EBL unabsorbed and absorbed sources, analysed with CTA nominal sensitivity conditions and RTA degraded sensitivity conditions. Data follow a Gaussian distribution (Table 6.2). **Central panels** Similar to the left panels, parameter (declination) distributions are from $t_{exp} = 1$ s observation analysis (b), $t_{exp} = 5$ s (e), $t_{exp} = 10$ s (h) and $t_{exp} = 100$ s (k). Data follow a Gaussian distribution (Table 6.2). **Right panels** Similar to the other panels, parameter (spherical distance) distributions are from $t_{exp} = 1$ s observation analysis (b), $t_{exp} = 5$ s (e), $t_{exp} = 10$ s (h) and $t_{exp} = 100$ s (k). Data follow a Rayleigh distribution (Table 6.2) as expected from Section 5.4.

Appendix E

Intermediate tests

From Section 6.3, the significance distribution at 5 (green), 10 (red) and 100 (blue) s of exposure time (Figure E.1) are shown. The top panel refers to CTA nominal performance while the bottom panel refers to RTA degraded performance. In Figure E.2, the confidence regions of the source localisation are given for σ =1, 2, 3 and 5 equal probability radii drawn from a Rayleigh distribution (Section 5.4.2 and 5.4.3). In Figure E.3, the same probability contours are given for the covariance of the Gaussian parameters, as explained in Section 5.4.3.

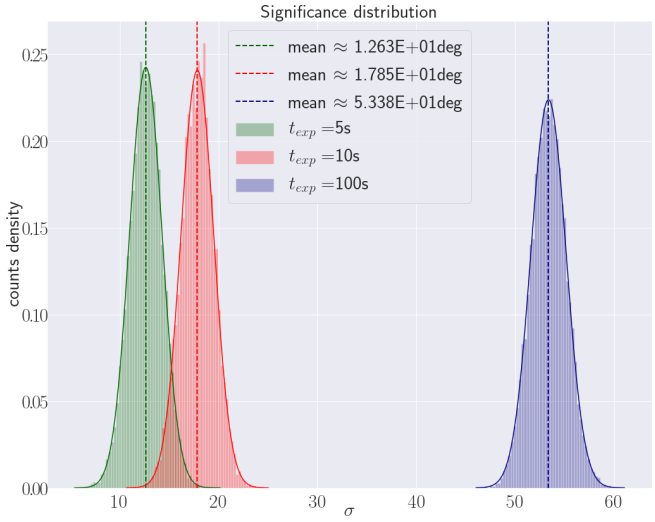

(a)

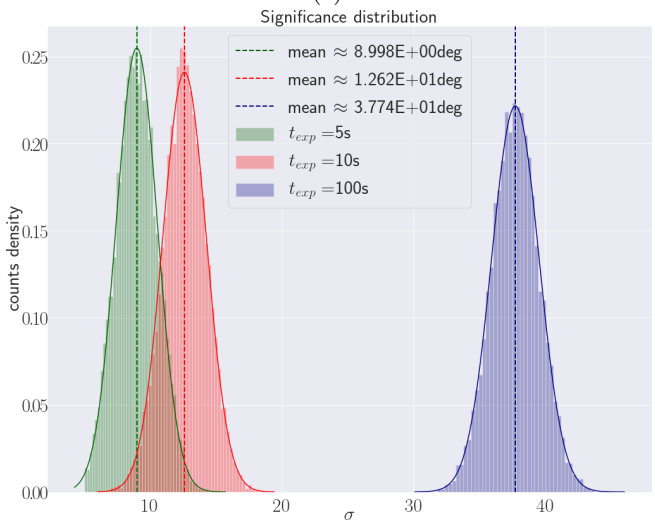

(b)

Figure E.1: Distribution of the detection significance ($\sigma = \sqrt{TS}$) for t_{exp} =5 s (green), 10 s (red) and 100 s (blue). The top panel displays the distributions obtained with nominal sensitivity analysis, while the bottom panel refers to an RTA analysis hence accounting for degraded sensitivity.

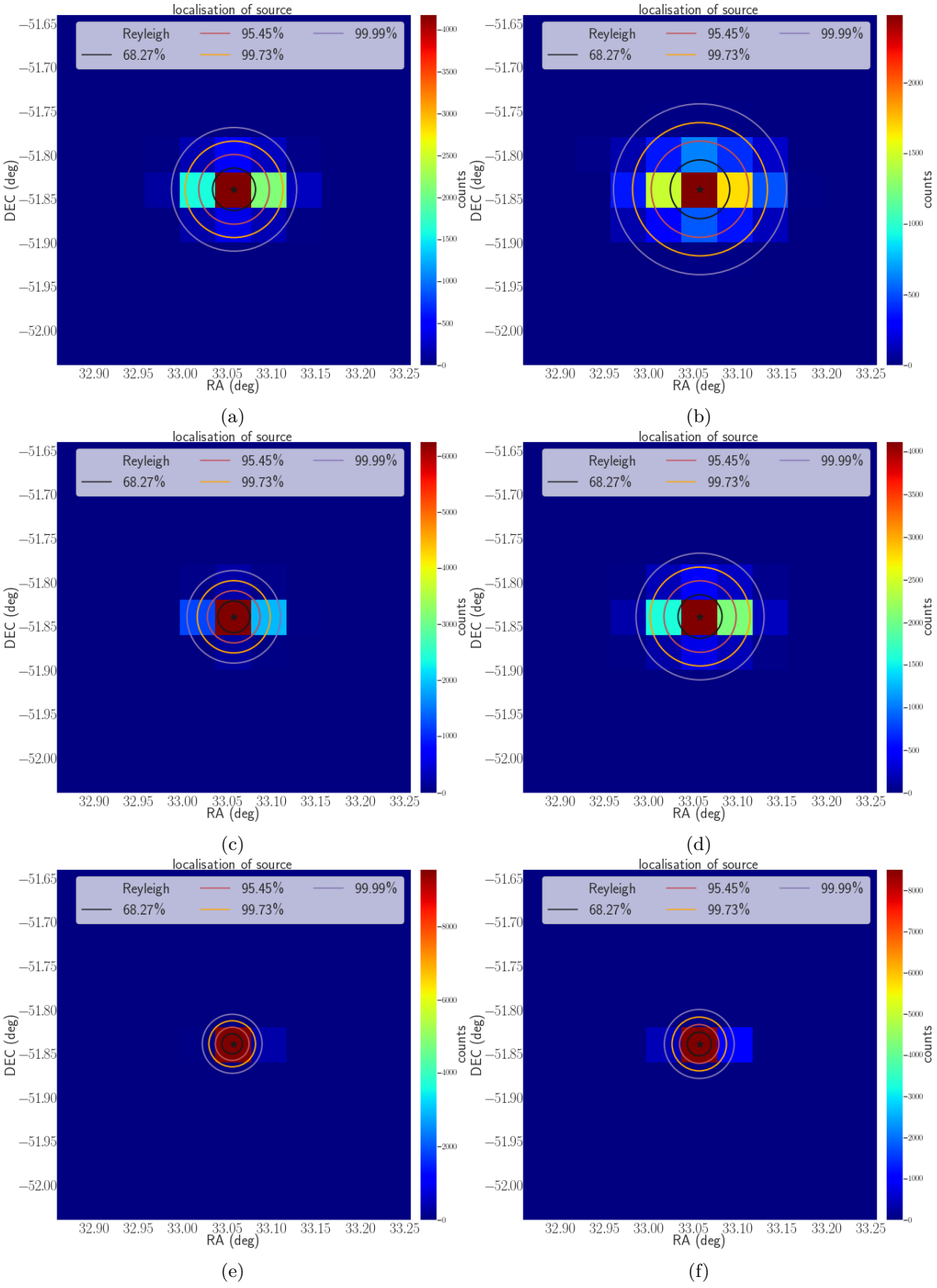

Figure E.2: Probability maps for the source localisation with CTA nominal sensitivity (left column) and RTA degraded sensitivity (right column). Confidence regions are drawn for 1, 2, 3 and 5 sigma radii of equivalent probability for Rayleigh distributed data (Section 5.4.3). Note the systematically larger dispersion of the positioning for RTA data, at lower exposure times, t_{exp} =5 s (top row) and t_{exp} =10 s (central row). At higher exposure (i.e. t_{exp} = 100 s) the spread of the distributions approache convergence (see also Figure 6.5(a)).

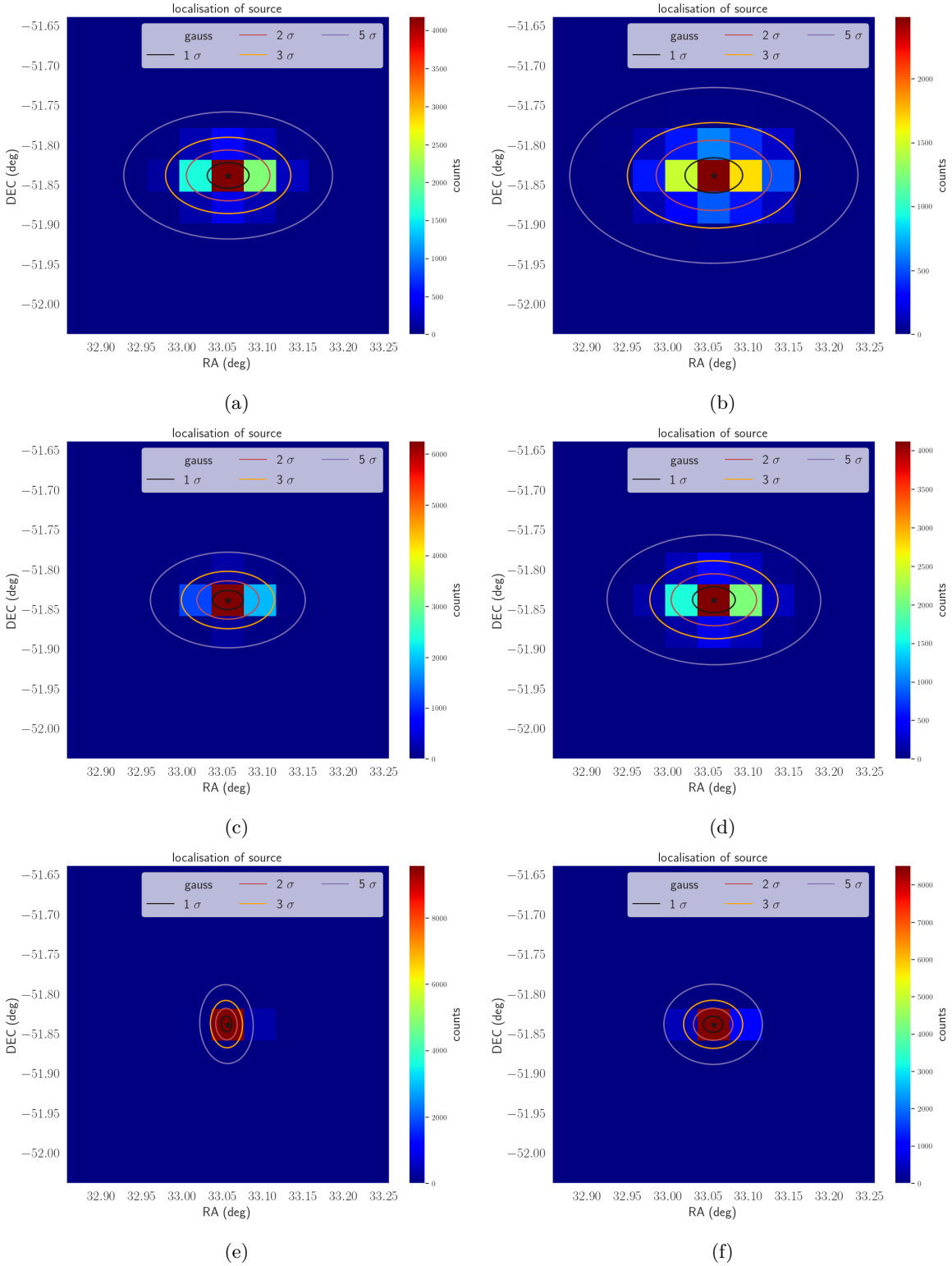

Figure E.3: Probability maps for the source localisation with CTA nominal sensitivity (left column) and RTA degraded sensitivity (right column). Confidence regions are drawn for 1, 2, 3 and 5 sigma from the covariance of the two normally distributed parameters (Section 5.4.3). Note the systematically larger dispersion of the positioning for RTA data, at lower exposure times, t_{exp} =5 s (top row) and t_{exp} =10 s (central row). At higher exposure (i.e. t_{exp} = 100 s) the gap in the spread of the distribution between nominal and degraded sensitivity approaches convergence (see also Figure 6.5(a)).

Appendix F

Follow-up tests

The full extent of the time-resolved analysis for the mocked blind-search and follow-up observation of a short GRB is shown here, for both CTA nominal (blue) and RTA degraded (red) sensitivity. In Figure F.1 a time binning of 10 s is used, while in Figure F.2 t_{exp} is fixed at 100 s. See Section 6.4.

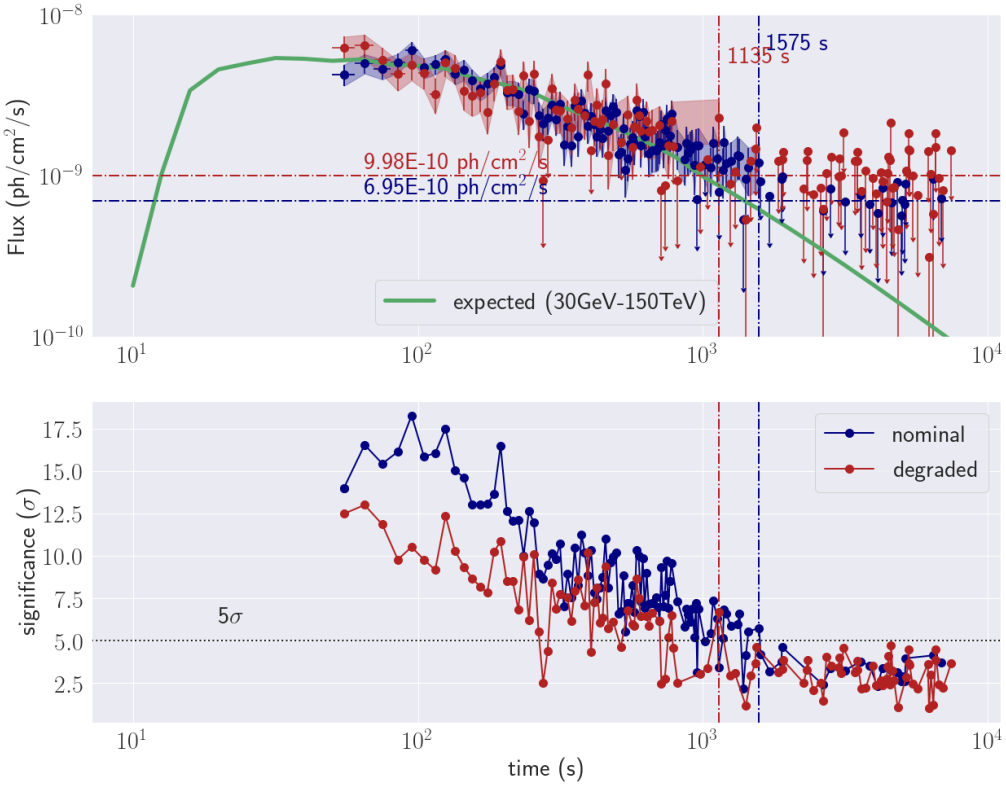

Figure F.1: GRB afterglow lightcurves for a 10 s time binned RTA analysis. Nominal (blue) and degraded (red) sensitivity analysis are compared in each case. The plot present the lightcurves (integral photon flux as a function of the observation time) in the top panel, while the bottom panel shows the detection significance as a function of the observation time. Horizontal lines have been drawn at the on-axis sensitivity for nominal (blue dot-dashed line) and degraded (red dot-dashed) sensitivity with t_{exp} =10 s as well as the 5σ significance threshold (grey dotted line). Vertical lines have been drawn at the time of the last positive detection acquired by the RTA pipeline for nominal (blue dot-dashed line) and degraded (red dot-dashed line) sensitivity.

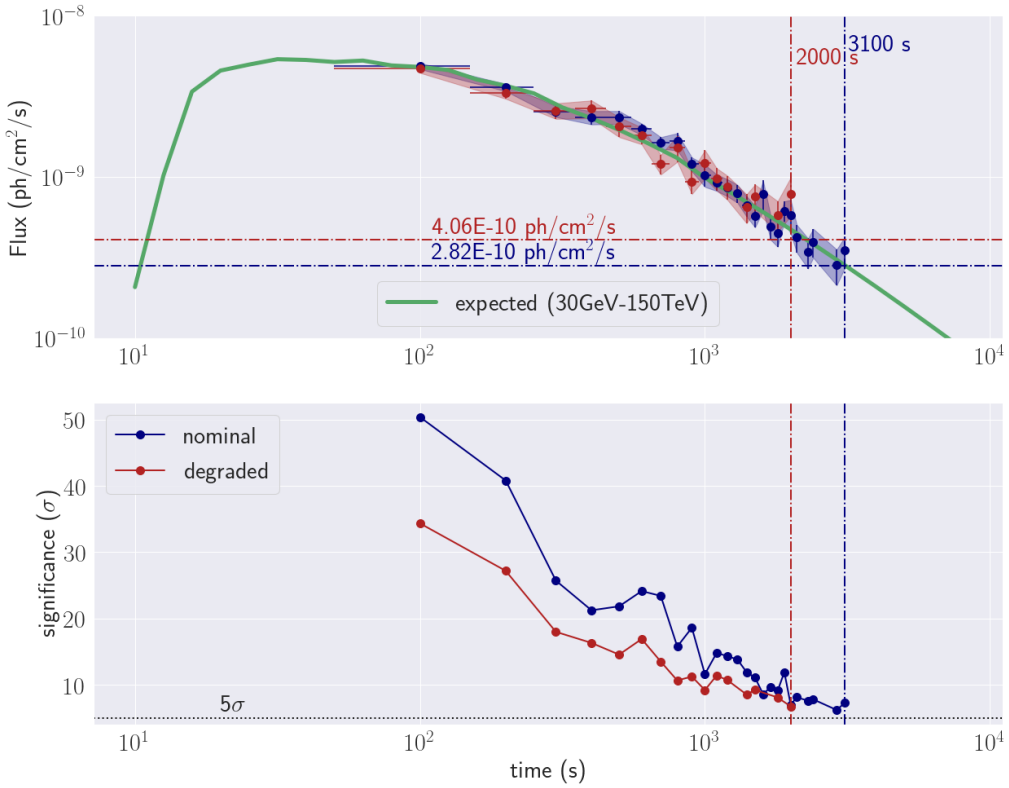

Figure F.2: GRB afterglow lightcurves for a 100 s time binned RTA analysis. Nominal (blue) and degraded (red) sensitivity analysis are compared. The plot present the lightcurves (integral photon flux as a function of the observation time) in the top panel, while the bottom panel shows the detection significance as a function of the observation time. Horizontal lines have been drawn at the on-axis sensitivity for nominal (blue dot-dashed line) and degraded (red dot-dashed) sensitivity with t_{exp} =100 s as well as the 5σ significance threshold (grey dotted line). Vertical lines have been drawn at the time of the last positive detection acquired by the RTA pipeline for nominal (blue dot-dashed line) and degraded (red dot-dashed line) sensitivity.

Appendix G

Final tests

Full sample of the analysis shown in Figure 6.7 of Section 6.5, which displayed 10 s exposure time analysis at RTA degraded sensitivity. In Figure G.1 the respective analysis at 100 s of exposure time is shown. Figure G.2 and Figure G.3 account for the CTA nominal performance, for analysis at 10 and 100 seconds of exposure time, respectively.

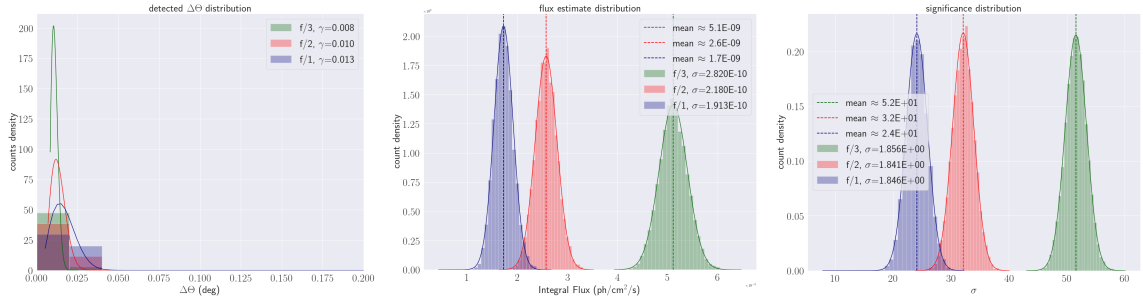

(a) (b) (c)

Figure G.1: In figure are displayed the statistical distribution of spherical distance between the true source position and the detected coordinates (left), the integral flux estimate distribution (centre) and the distribution of the detection significance (right). Data were derived by the analysis of a 10^4 sample of trials, accounting for RTA degraded sensitivity. Nominal intrinsic source flux (blue), a half (red) and a third (green) have been displayed for t_{exp} = 100 s analysis. Histograms are fitted with theoretical distributions characterised by their parameters as summarised in Table 6.7.

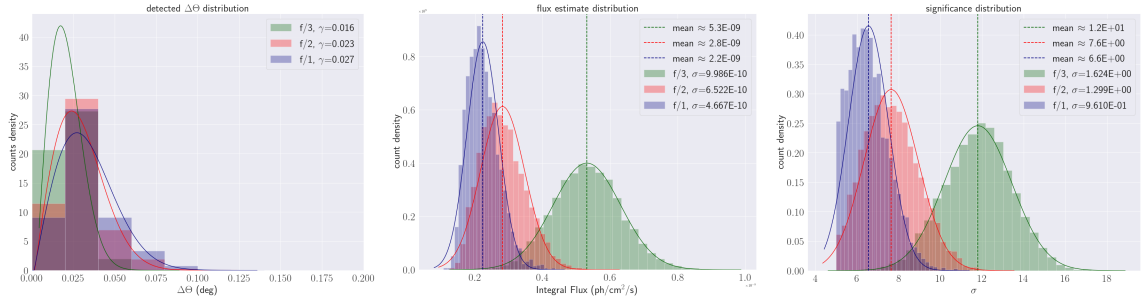

(a) (b) (c)

Figure G.2: In figure are displayed the statistical distribution of spherical distance between the true source position and the detected coordinates (left), the integral flux estimate distribution (centre) and the distribution of the detection significance (right). Data were derived by the analysis of a 10^4 sample of trials, accounting for CTA nominal sensitivity. Nominal intrinsic source flux (blue), a half (red) and a third (green) have been displayed for t_{exp} = 10 s analysis. Histograms are fitted with theoretical distributions characterised by their parameters as summarised in Table 6.7.

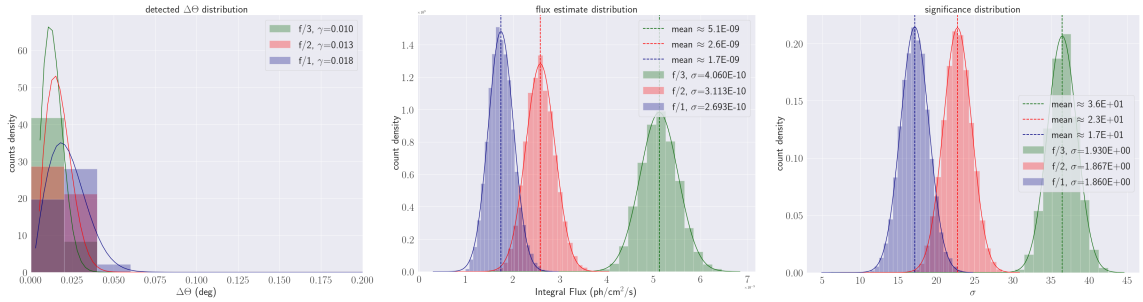

(a) (b) (c)

Figure G.3: In figure are displayed the statistical distribution of spherical distance between the true source position and the detected coordinates (left), the integral flux estimate distribution (centre) and the distribution of the detection significance (right). Data were derived by the analysis of a 10^4 sample of trials, accounting for CTA nominal sensitivity. Nominal intrinsic source flux (blue), a half (red) and a third (green) have been displayed for $t_{exp} = 100$ s analysis. Histograms are fitted with theoretical distributions characterised by their parameters as summarised in Table 6.7.

Acronyms

CTA Cherenkov Telescope Array.

EAS Extensive Air Shower.

EM Electromagnetic.

FoV Field of View.

GRB Gamma-Ray Burst.

GTI Good Time Intervals.

GW Gravitational Wave.

IACT Imaging Atmospheric Cherenkov Telescope.

IC Inverse Compton.

ISM Interstellar Medium.

LST Large-Sizes Telescope.

MM Multi-Messenger.

MST Medium-Sized Telescope.

MWL Multi-wavelength.

RTA Real-Time Analysis.

SAG Science Alert Generation.

SSC Synchrotron Self-Compton.

SST Small-Sized Telescope.

Bibliography

[1] The CTA Consortium et al. *Science with the Cherenkov Telescope Array*. World Scientific, 2019.

[2] B. Patricelli et al. Prospects for joint observations of gravitational waves and gamma rays from merging neutron star binaries. *Journal of Cosmology and Astroparticle Physics*, 2016(11):056–056, nov 2016.

[3] B. Patricelli et al. Searching for gamma-ray counterparts to gravitational waves from merging binary neutron stars with the cherenkov telescope array. *Journal of Cosmology and Astroparticle Physics*, 2018(05):056–056, may 2018.

[4] S. S. Wilks. The large-sample distribution of the likelihood ratio for testing composite hypotheses. *Ann. Math. Statist.*, 9(1):60–62, 03 1938.

[5] CTA Performance. `http://www.cta-observatory.org/science/cta-performance/`.

[6] J. Knoedlseder et al. Gammalib and ctools. a software framework for the analysis of astronomical gamma-ray data. *A&A*, pages 593, A1, ascl:1601.005, ascl:1110.007, 2016.

[7] ctools 1.6.1. Cherenkov telescope array science analysis software. `http://cta.irap.omp.eu/ctools/`.

[8] NASA/GSFC. The astronomical image and table format. `https://fits.gsfc.nasa.gov/`.

[9] gammalib 1.6.1. A versatile toolbox for scientific analysis of astronomical gamma-ray data.

[10] Astropy v3.2.1. A community python library for astronomy. `http://docs.astropy.org`.

[11] T. Vincenty. Direct and inverse solutions of geodesics on the ellipsoid with application of nested equations. *Survey Review*, XXIII(176):88–93, April 1975a.

[12] T. Vincenty. Correspondence. *Survey Review*, XXIII(180):294, April 1976.

[13] L. Rayleigh. On the resultant of a large number vibrations of the same pitch and of arbitrary phase. *Philosophical Magazine*, 10:73–78, 1880.

[14] D.B. Owen, K.J. Craswell, and D.L. Hanson. Non-parametric upper confidence bounds for p(y $<$ x) and confidence limits for p(y $<$ x) when x and y are normal. *Philosophical Magazine*, 59:906–924, 1977.

[15] A. Pak, N.B. Khoolenjani, and A.A. Jafari. Inference on p(y $<$ x) in bivariate rayleigh distribution. *arXiv:1405.4529v1*, [math.ST], 18 May 2014.

[16] Lara Nava. Preface. *International Journal of Modern Physics D*, 27(13):1802008, Jan 2018.

[17] L. Nava. High-energy emission from gamma-ray bursts. *International Journal of Modern Physics D*, 27(13):1842003, Jan 2018.

[18] L. Nava. Radiative Processes in Gamma-Ray Bursts. In *Clues on GRB Origin from Chemical Evolution Models*, page 4, Jan 2018.

[19] L. Nava et al. Clustering of LAT light curves: a clue to the origin of high-energy emission in gamma-ray bursts. *Monthly Notices of the Royal Astronomical Society*, 443(4):3578–3585, Oct 2014.

[20] L. Nava et al. Afterglow emission in gamma-ray bursts - I. Pair-enriched ambient medium and radiative blast waves. *Monthly Notices of the Royal Astronomical Society*, 433(3):2107–2121, Aug 2013.

[21] Lord Rayleigh O.M. F.R.S. Xxxi. on the problem of random vibrations, and of random flights in one, two, or three dimensions. *The London, Edinburgh, and Dublin Philosophical Magazine and Journal of Science*, 37(220):321–347, 1919.

[22] M. M. Siddiqui. Some problems connected with rayleigh distributions. *Journal or Research of National Bureau of Standards—D. Radio Propagation*, Vol. 66D(No. 2), October 1961.

[23] R. C. Gilmore et al. Semi-analytic modelling of the extragalactic background light and consequences for extragalactic gamma-ray spectra. *Monthly Notices of the Royal Astronomical Society*, 422(4):3189–3207, Jun 2012.

[24] A. Bulgarelli et al. Evaluating the maximum likelihood method for detecting short-term variability of AGILE γ-ray sources. *Astronomy & Astrophysics*, 540:A79, Apr 2012.

[25] J. R. Mattox et al. The Likelihood Analysis of EGRET Data. *The Astrophysical Journal*, 461:396, Apr 1996.

[26] A. Domínguez. Extragalactic background light and its implications for galaxy evolution and gamma-ray astronomy. IAC Talks, Astronomy and Astrophysics Seminars from the Instituto de Astrofísica de Canarias, Apr 2011.

[27] K. Bernlöhr, others, and CTA Consortium. Monte Carlo design studies for the Cherenkov Telescope Array. *Astroparticle Physics*, 43:171–188, Mar 2013.

[28] A. Donini et al. The Cherenkov Telescope Array Performance in Divergent Mode. In *36th International Cosmic Ray Conference (ICRC2019)*, volume 36 of *International Cosmic Ray Conference*, page 664, Jul 2019.

[29] T.-P. Li and Y.-Q. Ma. Analysis methods for results in gamma-ray astronomy. *The Astrophysical Journal*, 272:317–324, Sept 1983.

[30] J. Hinton et al. A New Era in Gamma-Ray Astronomy with the Cherenkov Telescope Array. *Astroparticle Physics*, 43:1–2, Mar 2013.

[31] K. Bernlöhr et al. Monte carlo design studies for the cherenkov telescope array. *Astroparticle Physics*, 43:171–188, Mar 2013.

[32] S. Funk and J.A. Hinton. Comparison of fermi-lat and cta in the region between 10–100gev. *Astroparticle Physics*, 43:348–355, Mar 2013.

[33] A. Bulgarelli et al. The On-Site Analysis of the Cherenkov Telescope Array. In *34th International Cosmic Ray Conference (ICRC2015)*, volume 34 of *International Cosmic Ray Conference*, page 763, Jul 2015.

[34] A. Bulgarelli et al. The Real-Time Analysis of Cherenkov Telescope Array Observatory. In *International Cosmic Ray Conference*, volume 33 of *International Cosmic Ray Conference*, page 3099, Jan 2013.

[35] V. Fioretti et al. Real-time analysis sensitivity evaluation of the cherenkov telescope array. In *32th International Cosmic Ray Conference (ICRC2015)*, volume 32, 2015.

[36] V. Fioretti, A. Bulgarelli, and F. Schüssler. The cherenkov telescope array on-site integral sensitivity: observing the crab. *Ground-based and Airborne Telescopes VI*, Jul 2016.

[37] V. Fioretti et al. The Cherenkov Telescope Array sensitivity to the transient sky. In *36th International Cosmic Ray Conference (ICRC2019)*, volume 36 of *International Cosmic Ray Conference*, page 673, Jul 2019.

[38] D. Fuhrmann and others for the KASCADE-Grande Collaboration. KASCADE-Grande Measurements of Energy Spectra for Elemental Groups of Cosmic Rays. In *International Cosmic Ray Conference*, volume 33 of *International Cosmic Ray Conference*, page 244, Jan 2013.

[39] R. Hanbury Brown. *The intensity interferometer. Its applications to astronomy.* Halsted Press, 1974.

[40] V.A. Acciari et al. Teraelectronvolt emission from the γ-ray burst grb 190114c. *Nature*, 575:455–458, 2019.

[41] H. Abdalla et al. A very-high-energy component deep in the γ-ray burst afterglow. *Nature*, 575:464–467, 2019.

[42] V.A. Acciari et al. Observation of inverse compton emission from a long γ-ray burst. *Nature*, 575:459–463, 2019.

[43] R. C. Gilmore et al. Iact observations of gamma-ray bursts: prospects for the cherenkov telescope array. *Experimental Astronomy*, 35(3):413–457, Oct 2012.

[44] J. Kakuwa et al. Prospects for detecting gamma-ray bursts at very high energies with the cherenkov telescope array. *Monthly Notices of the Royal Astronomical Society*, 425(1):514–526, Jul 2012.

[45] L. Gerard and CTA Consortium. Divergent pointing with the Cherenkov Telescope Array for surveys and beyond. In *34th International Cosmic Ray Conference (ICRC2015)*, volume 34 of *International Cosmic Ray Conference*, page 725, Jul 2015.

[46] M. Szanecki et al. Monte carlo simulations of alternative sky observation modes with the cherenkov telescope array. *Astroparticle Physics*, 67:33–46, Jul 2015.

[47] S. Inoue et al. Gamma-ray burst science in the era of the cherenkov telescope array. *Astroparticle Physics*, 43:252–275, Mar 2013.

[48] G. Ponti et al. The xmm–newton view of the central degrees of the milky way. *Monthly Notices of the Royal Astronomical Society*, 453(1):172–213, Aug 2015.

[49] T. N. LaRosa et al. A Wide-Field 90 Centimeter VLA Image of the Galactic Center Region. *The Astrophysical Journal*, 119(1):207–240, Jan 2000.

[50] S. Molinari et al. A 100 pc elliptical and twisted ring of cold and dense molecular clouds relvealed by herschel around the galactic centre. *The Astrophysical Journal*, 735(2):L33, Jun 2011.

[51] H. Tajima. Fermi Observations of high-energy gamma-ray emissions from GRB 080916C. *arXiv e-prints*, page arXiv:0907.0714, Jul 2009.

[52] J. D. Finke et al. Modelling the extragalactic background light from stars and dust. *The Astrophysical Journal*, 712(1):238–249, Feb 2010.

[53] M. G. Bernardini et al. Posytive – a grb population study for the cherenkov telescope array (icrc-2019). *arXiv e-prints*, page arXiv:1908.01544, Aug 2019.

[54] L. Bergström. Dark matter and imaging air cherenkov arrays. *Astroparticle Physics*, 43:44–49, 03 2013.

[55] M. Doro et al. Dark matter and fundamental physics with the cherenkov telescope array. *Astroparticle Physics*, 43:189–214, Mar 2013.

[56] C. van Eldik. Gamma rays from the galactic centre region: A review. *Astroparticle Physics*, 71:45–70, Dec 2015.

[57] Dainis Dravins et al. Optical intensity interferometry with the cherenkov telescope array. *Astroparticle Physics*, 43:331 – 347, 2013. Seeing the High-Energy Universe with the Cherenkov Telescope Array - The Science Explored with the CTA.

[58] A. A. et al. Abdo. Observations of the large magellanic cloud with fermi. *Astronomy and Astrophysics*, 512:A7, Mar 2010.

[59] H.E.S.S. Collaboration. The exceptionally powerful tev γ-ray emitters in the large magellanic cloud. *Science*, 347(6220):406–412, Jan 2015.

[60] M. Ackermann et al. Deep view of the large magellanic cloud with six years of fermi-lat observations. *Astronomy & Astrophysics*, 586:A71, Jan 2016.

[61] A. Abramowski et al. Discovery of gamma-ray emission from the extragalactic pulsar wind nebula n157b with h.e.s.s. *Astronomy & Astrophysics*, 545:L2, Aug 2012.

[62] F. Aharonian et al. The crab nebula and pulsar between 500 GeV and 80 TeV: Observations with the HEGRA stereoscopic air cerenkov telescopes. *The Astrophysical Journal*, 614(2):897–913, oct 2004.

[63] G. Dubus et al. Surveys with the cherenkov telescope array. *Astroparticle Physics*, 43:317–330, Mar 2013.

[64] F. Schüssler. The Transient program of the Cherenkov Telescope Array. In *36th International Cosmic Ray Conference (ICRC2019)*, volume 36 of *International Cosmic Ray Conference*, page 788, Jul 2019.

[65] W. Bednarek. High energy γ-ray emission from compact galactic sources in the context of observations with the next generation cherenkov telescope arrays. *Astroparticle Physics*, 43:81–102, Mar 2013.

[66] D. Mazin et al. Potential of ebl and cosmology studies with the cherenkov telescope array. *Astroparticle Physics*, 43:241–251, Mar 2013.

[67] E. de Oña-Wilhelmi et al. Prospects for observations of pulsars and pulsar wind nebulae with cta. *Astroparticle Physics*, 43:287–300, Mar 2013.

[68] J.M. Paredes et al. Binaries with the eyes of cta. *Astroparticle Physics*, 43:301–316, Mar 2013.

[69] J. I. Katz. Fast radio bursts — a brief review: Some questions, fewer answers. *Modern Physics Letters A*, 31(14):1630013, May 2016.

[70] P. T. O'Brien and S. J. Smartt. Interpreting signals from astrophysical transient experiments. *Philosophical Transactions of the Royal Society of London Series A*, 371(1992):20120498–20120498, Apr 2013.

[71] M. Ahlers and F. Halzen. High-energy cosmic neutrino puzzle: A review. *Reports on progress in physics. Physical Society (Great Britain)*, 78:126901, 10 2015.

[72] F. Halzen. Pionic photons and neutrinos from cosmic ray accelerators. *Astroparticle Physics*, 43:155–162, Mar 2013.

[73] B.P. Abbott et al. Observation of gravitational waves from a binary black hole merger. *Physical Review Letters*, 116(6), Feb 2016.

[74] V. Connaughton et al. Fermi-gbm observations ligo gravitational-wave gw150914. *The Astrophysical Journal*, 826(1):L6, Jul 2016.

[75] R. Fernàndez and B. D. Metzger. Electromagnetic signatures of neutron star mergers in the advanced ligo era. *Annual Review of Nuclear and Particle Science*, 66(1):23–45, Oct 2016.

[76] T. Antoni et al. Kascade measurements of energy spectra for elemental groups of cosmic rays: Results and open problems. *Astroparticle Physics*, 24(1-2):1–25, Sep 2005.

[77] A.M. Hillas. TOPICAL REVIEW: Can diffusive shock acceleration in supernova remnants account for high-energy galactic cosmic rays? *Journal of Physics G Nuclear Physics*, 31(5):R95–R131, May 2005.

[78] L. Oc. Drury. REVIEW ARTICLE: An introduction to the theory of diffusive shock acceleration of energetic particles in tenuous plasmas. *Reports on Progress in Physics*, 46(8):973–1027, Aug 1983.

[79] A. R. Bell. Turbulent amplification of magnetic field and diffusive shock acceleration of cosmic rays. *Monthly Notices of the Royal Astronomical Society*, 353(2):550–558, Sep 2004.

[80] P. P. Papadopoulos and W.-F. Thi. The initial conditions of star formation: Cosmic rays as the fundamental regulators. *Astrophysics and Space Science Proceedings*, page 41–59, 2013.

[81] H. Sol et al. Active galactic nuclei under the scrutiny of cta. *Astroparticle Physics*, 43:215–240, Mar 2013.

[82] M. Ackermann et al. Search for cosmic-ray induced gamma-ray emission in galaxy clusters. *The Astrophysical Journal*, 787(1):18, Apr 2014.

[83] G. Mark Voit. Tracing cosmic evolution with clusters of galaxies. *Reviews of Modern Physics*, 77(1):207–258, Apr 2005.

[84] L. Feretti et al. Clusters of galaxies: observational properties of the diffuse radio emission. *The Astronomy and Astrophysics Review*, 20(1), May 2012.

[85] G. di Sciascio and Lhaaso Collaboration. The LHAASO experiment: From Gamma-Ray Astronomy to Cosmic Rays. *Nuclear and Particle Physics Proceedings*, 279-281:166–173, Oct 2016.

[86] P Mészáros. Gamma-ray bursts. *Reports on Progress in Physics*, 69(8):2259–2321, Jul 2006.

[87] P. Kumar and B. Zhang. The physics of gamma-ray bursts & relativistic jets. *Physics Reports*, 561:1–109, Feb 2015.

[88] C. Kouveliotou et al. Identification of Two Classes of Gamma-Ray Bursts. *The Astrophysical Journal, Letters*, 413:L101, Aug 1993.

[89] R. Sari, T. Piran, and R. Narayan. Spectra and Light Curves of Gamma-Ray Burst Afterglows. *The Astrophysical Journal, Letters*, 497(1):L17–L20, Apr 1998.

[90] A. Maxham, B.-B. Zhang, and B. Zhang. Is gev emission from gamma-ray bursts of external shock origin? *Monthly Notices of the Royal Astronomical Society*, 415(1):77–82, May 2011.

[91] M. Ackermann et al. The First Fermi-LAT Gamma-Ray Burst Catalog. *The Astrophysical Journal, Supplement*, 209(1):11, Nov 2013.

[92] G. Vianello et al. The bright and the slow—grbs 100724b and 160509a with high-energy cutoffs at $\lesssim$100 mev. *The Astrophysical Journal*, 864(2):163, Sep 2018.

[93] M. Yassine et al. Time evolution of the spectral break in the high-energy extra component of grb 090926a. *Astronomy & Astrophysics*, 606:A93, Oct 2017.

[94] M. Ackermann, M. Ajello, and Asano. Detection of a Spectral Break in the Extra Hard Component of GRB 090926A. *The Astrophysical Journal*, 729(2):114, Mar 2011.

[95] K. Asano and P. Mészáros. Spectral-temporal simulations of internal dissipation models of gamma-ray bursts. *The Astrophysical Journal*, 739(2):103, Sep 2011.

[96] D.B Kieda, S.P Swordy, and S.P Wakely. A high resolution method for measuring cosmic ray composition beyond 10 tev. *Astroparticle Physics*, 15(3):287–303, Jun 2001.

[97] F. Aharonian et al. First ground-based measurement of atmospheric cherenkov light from cosmic rays. *Physical Review D*, 75(4), Feb 2007.

[98] D. Malyshev, I. Cholis, and J. Gelfand. Pulsars versus dark matter interpretation of atic/pamela. *Physical Review D*, 80(6), Sep 2009.

[99] F. A. Aharonian, A. M. Atoyan, and H. J. Voelk. High energy electrons and positrons in cosmic rays as an indicator of the existence of a nearby cosmic tevatron. *Astronomy & Astrophysics*, 294:L41–L44, Feb 1995.

[100] T. Kobayashi et al. The most likely sources of high-energy cosmic-ray electrons in supernova remnants. *The Astrophysical Journal*, 601(1):340–351, Jan 2004.

[101] A. Bulgarelli et al. The Cherenkov Telescope Array Observatory: top level use cases. In Gianluca Chiozzi and Juan C. Guzman, editors, *Software and Cyberinfrastructure for Astronomy IV*, volume 9913, pages 1114 – 1125. International Society for Optics and Photonics, SPIE, 2016.

[102] M. Seglar-Arroyo et al. The gravitational wave follow-up program of the Cherenkov Telescope Array. In *36th International Cosmic Ray Conference (ICRC2019)*, volume 36 of *International Cosmic Ray Conference*, page 790, Jul 2019.

[103] G. Ghisellini et al. GeV emission from gamma-ray bursts: a radiative fireball? *Monthly Notices of the Royal Astronomical Society*, 403(2):926–937, 03 2010.

[104] G. Ghirlanda, G. Ghisellini, and L. Nava. The onset of the GeV afterglow of GRB 090510. *The Astrophysical Journal*, 510:L7, Feb 2010.

[105] P.-H. Tam et al. An evolving gev spectrum from prompt to afterglow: the case of grb 160509a. *The Astrophysical Journal*, 844, 06 2017.

[106] P. Beniamini et al. Energies of GRB blast waves and prompt efficiencies as implied by modelling of X-ray and GeV afterglows. *Monthly Notices of the Royal Astronomical Society*, 454(1):1073–1085, 09 2015.

[107] R. Atkins et al. Milagrito, a tev air-shower array. *Nuclear Instruments and Methods in Physics Research Section A: Accelerators, Spectrometers, Detectors and Associated Equipment*, 449:478–499, 09 1999.

[108] M. de Naurois. GRB190829A: Detection of VHE gamma-ray emission with H.E.S.S. *The Astronomer's Telegram*, 13052:1, Aug 2019.

[109] B. Zhang. A possible connection between fast radio bursts and gamma-ray bursts. *The Astrophysical Journal*, 780(2):L21, Dec 2013.

[110] Zhu, B. et al. The long-lasting optical afterglow plateau of short burst grb 130912a. *A&A*, 576:A71, 2015.

[111] M. Bo er, B. Gendre, and G. Stratta. Testing for a class of ULGRBs using Swift GRBs. *PoS*, SWIFT10:032, 2015.

[112] T. Piran. Gamma-ray bursts and the fireball model. *Physics Reports*, 314(6):575–667, Jun 1999.

[113] R. W. Klebesadel, I. B. Strong, and R. A. Olson. Observations of Gamma-Ray Bursts of Cosmic Origin. *The Astrophysical Journal, Letters*, 182:L85, Jun 1973.

[114] G. Stratta, A. Di Piano, A. Bulgarelli, G. De Cesare, V. Fioretti, N. Parmiggiani, L. Nava, B. Patricelli, and for the CTA ASTRI project. CTA Real Time Analysis output from the follow-up of a short GRB. poster presented at CTA Symposium, Bologna, May 2019.

[115] S. Tampieri. *Real time aperture photometry with Cherenkov Telescope Array.* Master's thesis, AMS Università di Bologna, March 2020.

[116] E. P. Mazets et al. Investigations of diffuse cosmic gamma radiation in the range 28 keV-4.1 MeV. *ZhETF Pisma Redaktsiiu*, 20:77–80, Jul 1974.

[117] T. L. Cline et al. Energy Spectra of Cosmic Gamma-Ray Bursts. *The Astrohpysical Journal, Letters*, 185:L1, Oct 1973.

[118] C. A. Meegan et al. Spatial distribution of γ-ray bursts observed by BATSE. *Nature*, 355(6356):143–145, Jan 1992.

[119] E. Costa et al. Discovery of an X-ray afterglow associated with the γ-ray burst of 28 February 1997. *Nature*, 387(6635):783–785, Jun 1997.

[120] J. van Paradijs et al. Transient optical emission from the error box of the γ-ray burst of 28 February 1997. *Nature*, 386(6626):686–689, Apr 1997.

[121] D. A. Frail et al. The radio afterglow from the γ-ray burst of 8 May 1997. *Nature*, 389(6648):261–263, Sep 1997.

[122] J. Goodman. Are gamma-ray bursts optically thick? *The Astrophysical Journal, Letters*, 308:L47, Sep 1986.

[123] B. Paczynski. Gamma-ray bursters at cosmological distances. *The Astrophysical Journal, Letters*, 308:L43–L46, Sep 1986.

[124] A. Shemi and T. Piran. The Appearance of Cosmic Fireballs. *The Astrophysical Journal, Letters*, 365:L55, Dec 1990.

[125] B. Paczynski. Super-Eddington Winds from Neutron Stars. *The Astrophysical Journal*, 363:218, Nov 1990.

[126] T. Piran, A. Shemi, and R. Narayan. Hydrodynamics of Relativistic Fireballs. *Monthly Notices of the Royal Astronomical Society*, 263:861, Aug 1993.

[127] D. Hartmann. Afterglows from the largest explosions in the universe. *Proceedings of the National Academy of Sciences of the United States of America*, 96:4752–5, 05 1999.

[128] A. Gomboc. Unveiling the secrets of gamma ray bursts. *Contemporary Physics*, 53, 06 2012.

[129] J. P. A. Clark and D. M. Eardley. Evolution of close neutron star binaries. *The Astrophysical Journal*, 215:311–322, Jul 1977.

[130] D. Eichler et al. Nucleosynthesis, neutrino bursts and γ-rays from coalescing neutron stars. *Nature*, 340(6229):126–128, Jul 1989.

[131] J. M. Weisberg and J. H. Taylor. Observations of post-newtonian timing effects in the binary pulsar psr 1913+16. *Phys. Rev. Lett.*, 52:1348–1350, Apr 1984.

[132] A. Acharyya et al. Monte carlo studies for the optimisation of the cherenkov telescope array layout. *Astroparticle Physics*, 111:35–53, Sep 2019.

[133] B. P. Abbott et al. Multi-messenger observations of a binary neutron star merger. *The Astrophysical Journal*, 848(2):L12, Oct 2017.

[134] A.R. Bell. Cosmic ray acceleration. *Astroparticle Physics*, 43:56 – 70, 2013. Seeing the High-Energy Universe with the Cherenkov Telescope Array - The Science Explored with the CTA.

[135] L. Nava, G. Ghirlanda, and G. Ghisellini. Selection effects on GRB spectral-energy correlations. In Charles Meegan, Chryssa Kouveliotou, and Neil Gehrels, editors, *American Institute of Physics Conference Series*, volume 1133 of *American Institute of Physics Conference Series*, pages 350–355, May 2009.

[136] G. Ghisellini et al. Proton-synchrotron as the radiation mechanism of the prompt emission of GRBs? *arXiv e-prints*, page arXiv:1912.02185, Dec 2019.

[137] A. Franceschini and G. Rodighiero. The extragalactic background light revisited and the cosmic photon-photon opacity. *Astronomy & Astrophysics*, 603:A34, Jul 2017.

[138] A. Franceschini, G. Rodighiero, and M. Vaccari. Extragalactic optical-infrared background radiation, its time evolution and the cosmic photon-photon opacity. *Astronomy & Astrophysics*, 487(3):837–852, Jun 2008.

[139] Alan A. Watson. The discovery of cherenkov radiation and its use in the detection of extensive air showers. *Nuclear Physics B - Proceedings Supplements*, 212-213:13–19, Mar 2011.

[140] G. G. Fazio et al. A Search for Discrete Sources of Cosmic Gamma Rays of Energies Near 2 X $10\hat{\{}12\}$ eV. *The Astrophysical Journal, Letters*, 154:L83, Nov 1968.

[141] A. M. Hillas. Evolution of ground-based gamma-ray astronomy from the early days to the Cherenkov Telescope Arrays. *Astroparticle Physics*, 43:19–43, Mar 2013.

[142] C. Bigongiari. The MAGIC telescope. In *International Europhysics Conference on High Energy Physics, HEP2005*, page 20, Jan 2005.

[143] F. Aharonian et al. Hess observations of the galactic center region and their possible dark matter interpretation. *Physical Review Letters*, 97(22), Nov 2006.

[144] Edo Berger. Short-duration gamma-ray bursts. *Annual Review of Astronomy and Astrophysics*, 52(1):43–105, 2014.

[145] Barbara Patricelli et al. Gw cosmos: Gravitational wave compact binary system simulations, Oct 2018.